

Cover Page



Universiteit Leiden



The handle <http://hdl.handle.net/1887/36998> holds various files of this Leiden University dissertation.

Author: Dunnen, Angela den

Title: Surface-structure dependencies in catalytic reactions

Issue Date: 2015-12-09

Surface-structure dependencies in catalytic reactions

Proefschrift

ter verkrijging van
de graad van Doctor aan de Universiteit Leiden,
op gezag van Rector Magnificus prof. mr. C. J. J. M. Stolker
volgens besluit van het College voor Promoties
te verdedigen op woensdag 9 december 2015
klokke 15:00

door

Angela den Dunnen

geboren te Hardinxveld-Giessendam in 1986

Promotiecomissie:

Promotor: Prof. dr. M. T. M. Koper

Co-promotor: Dr. L. B. F. Juurlink

Overige leden: Prof. dr. G. J. Kroes
Prof. dr. J. Brouwer
Prof. dr. I. Chorkendorff (Technical University of Denmark, DK)
Prof. dr. A. Groß (Ulm University, DE)
Dr. I. M. N. Groot

The research reported in this thesis was financially supported by the Dutch National Research School Combination Catalysis (NRSC-Catalysis).

ISBN: 978-94-6299-235-1

Printing: Ridderprint BV

Table of contents

1	Introduction	1
1.1	Catalysis	1
1.2	Heterogeneous catalysis	2
1.2.1	Three-way catalytic converter	3
1.2.2	The fuel cell	3
1.3	Surface science	4
1.3.1	Ultra-high vacuum	5
1.3.2	Surfaces	5
1.4	Scope of this thesis	6
2	Experimental set-up and techniques	9
2.1	The set-up	9
2.2	Techniques	11
2.2.1	Low energy electron diffraction	11
2.2.2	Temperature programmed desorption	12
2.2.3	Time-of-flight	13
2.2.4	King and Wells	14
3	Reaction dynamics of initial O₂ sticking on Pd(100)	17
3.1	Introduction	18
3.2	Experimental	20
3.2.1	The apparatus	20
3.2.2	The Pd(100) crystal	21
3.2.3	S_0 determination	22
3.3	Results and discussion	24

3.4	Summary	29
3.5	Conclusion	30
4	Thermal desorption and time-dependent adsorption of oxygen on Pd(100)	33
4.1	Introduction	34
4.2	Experimental	36
4.3	Results	40
4.3.1	Oxygen adsorption	40
4.3.2	Oxygen desorption	41
4.4	Discussion	45
4.4.1	Oxygen adsorption	45
4.4.2	Oxygen desorption	47
4.5	Summary	51
5	Adsorption and dissociation of O₂ on Pt(553)	53
5.1	Introduction	54
5.2	Experimental	56
5.3	Results	57
5.3.1	Initial sticking probability	57
5.3.2	Coverage dependent sticking probability	61
5.3.3	Thermal desorption	63
5.4	Discussion	64
5.4.1	Initial sticking probability	64
5.4.2	Sticking at low E_i	67
5.4.3	Sticking at high E_i	71
5.5	Conclusions	73
6	Long-range influence of steps on water adsorption on clean and D-covered Pt surfaces	77
6.1	Introduction	78
6.2	Experimental	81
6.3	Results and discussion	83
6.3.1	H ₂ O desorption from Pt(111), Pt(533), Pt(755), and Pt(977)	83
6.3.2	H ₂ O desorption from D precovered Pt(111), Pt(533), Pt(755), and Pt(977)	87

6.4 Conclusion	92
7 Future prospects	95
7.1 Double beam	95
7.2 Curved single crystals	100
Bibliography	101
Summary	107
Samenvatting	111
List of Publications	115
Curriculum Vitae	117

Chapter 1

Introduction

1.1 Catalysis

The definition of a catalyst is described in the Oxford Dictionaries as 'a substance that increases the rate of a chemical reaction without itself undergoing any permanent chemical change'. Figure 1.1 illustrates the principle of a catalytic reaction. The reactants bind to the catalyst material, the molecules react and form a product, the product separates from the catalyst, and the catalyst can be used again for a new reaction. In principle, a reaction can take place without a catalyst if sufficient energy is present to overcome the high activation barrier. The catalyst provides an alternative route with lower barriers.

Catalysts play a very important role in life, industry, and the environment. There are three different main types of catalysis, namely: biological, homogeneous, and heterogeneous catalysis. Enzymes are very specific and efficient catalysts and they play a crucial role in all biological processes. An example of a biological catalyst is yeast. It has been used for centuries to make alcoholic drinks. In homogeneous catalysis, both the catalyst and the reactants are in the same phase, usually the gaseous or liquid phase. The advantage is that all catalyst particles can participate in the reaction. A disadvantage is that it is difficult to recover the catalyst materials from the reaction mixture. Heterogeneous catalysis is the most common type of catalysis used in industry for the production of fine chemicals and materials. A heterogeneous catalyst is in a different phase than the reactants. The catalyst is usually a solid material, while the reactants are gases or liquids. Only the catalyst

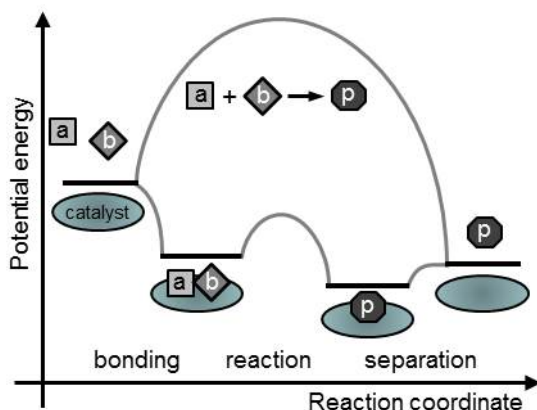


Figure 1.1: Potential energy diagram of a heterogeneously catalyzed reaction. Adapted from¹.

material near the surface participates in the reaction. It is easier to separate a solid catalyst from the reaction mixtures than in homogeneous catalysis. The research in this work involves heterogeneous catalysis.

1.2 Heterogeneous catalysis

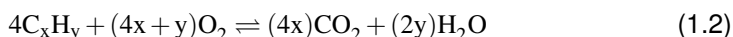
Precious metals, such as platinum and palladium, are good catalytic materials for various reactions. In heterogeneous catalysis, only the surface of the solid participates in the reactions. Therefore, it is important that small particles with a large surface area, named nanoparticles, are used. The surface atoms have a different structure than the bulk atoms. Surface atoms have fewer neighboring atoms and can interact with reactants. A typical reaction cycle in heterogeneous catalysis includes adsorption of reactants on the surface, a reaction, and finally desorption of the product(s). For this process, it is important that the reactants and products bind strong enough to the surface, so that the reaction can take place. At the same time the molecules should not bind too strongly to the surface to prevent molecules from blocking the active sites and kill the catalytic activity.

Molecules can adsorb to the surface in three ways. The first type of adsorption is physisorption. The molecules have a very weak van der Waals interaction with the surface. The chemical identity of the surface and the adsorbates are still intact.

The second type is molecular chemisorption. The molecules adsorb and form a new bond with the surface, while the molecular bonds stay intact. The last type of adsorption is the dissociative chemisorption. The bonds in the molecule are broken, different segments have now formed new bonds with the surface. The adsorbed species can form new compounds, which will then desorb from the surface.

1.2.1 Three-way catalytic converter

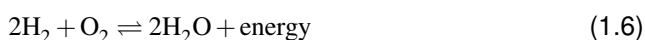
The most well known example of a catalyst is likely the one in our car exhaust: the three-way catalytic converter. It converts harmful gases into benign products.



The most efficient catalysts for the oxidation reactions (1.1 and 1.2) are platinum and palladium. For the nitric oxide reduction reaction (1.3), rhodium and palladium are the most efficient. Platinum and rhodium are used most often in the three-way catalytic converter, but palladium can replace both precious metals. For an optimal conversion of all gases, a proper air-to-fuel ratio and operating temperature are necessary¹.

1.2.2 The fuel cell

The proton exchange membrane fuel cell (PEMFC) is a promising hydrogen fuel cell for applications in transportation and mobile electronics². A schematic overview of a PEMFC is shown in figure 1.2 (adapted from³). The hydrogen oxidation reaction (HOR, reaction 1.4) takes place at the anode and the oxygen reduction reaction (ORR, reaction 1.5) at the cathode. In the overall reaction (reaction 1.6), hydrogen and oxygen are converted into water and energy.



Platinum is one of the metals that is sufficiently active to activate O_2 , and at the same time noble enough to release oxygen in the form of water from the surface. Yet, a suitable catalyst should show at least two to four times more stable catalytic activity than Pt alone⁴. A possible solution is the use of bimetallic catalyst materials, such as Pt_3Sc or Pt_3Y ⁵.

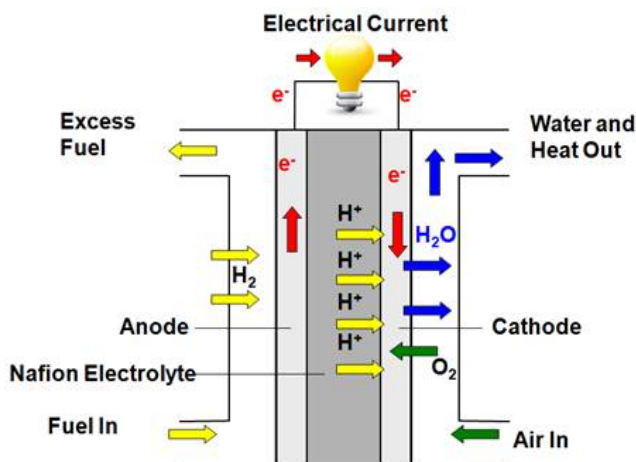


Figure 1.2: Schematic overview of a proton exchange membrane fuel cell (PEMFC), adapted from³.

1.3 Surface science

Heterogeneous catalysts are widely used and often very expensive (e.g. PtNi and PtFe). It is important to improve our understanding of the interaction of the reactants and products with the catalytic surface in order to obtain better and cheaper catalyst materials for the future. Theoretical studies can provide fundamental insights in the processes and mechanisms taking place on the surface. They can help in predicting new and promising catalysts⁶. The state-of-the-art methods and techniques now make it possible to reach chemical accuracy⁷. Nevertheless, it is still difficult and expensive to include all possible interactions, defect sites, and larger molecules. Electrochemical catalytic studies are closer to reality than many gas-phase studies. Measurements are performed in an aqueous environment and effects of, e.g. pH and potential can be studied. However, the electrolyte itself makes it difficult to

probe the solid-liquid interface. Ultra-high vacuum (UHV) studies may form a bridge between theory and electrochemistry.

1.3.1 Ultra-high vacuum

In an ultra-high vacuum chamber, the pressure is usually lower than $1 \cdot 10^{-9}$ mbar. The reaction conditions can be controlled quite accurately. Depending on the pressure and type of molecules in the chamber, the catalytic surface remains clean for a relatively long time. The amount of adsorbate and its energy can be controlled by leaking in different amounts of gas or by using a (supersonic) molecular beam. Various UHV techniques, e.g. temperature programmed desorption (TPD), low energy electron diffraction (LEED), and the King and Wells (KW) technique⁸, can be used to obtain insight on the fundamental processes that take place at surfaces during reaction, e.g. adsorption, reaction, desorption. These techniques are explained in more detail in chapter 2.

One of the major draw-backs of using UHV, is the large difference in pressure between catalysis in UHV and industry. In UHV, the pressure is more than 12 orders of magnitude lower. This is also known as the pressure gap. Nowadays, various techniques are developed to study the interaction between the reactants and catalytic surface under more realistic pressures. Nevertheless, a combination of all different types of studies is necessary to understand the reaction mechanisms and processes in the most complete way.

1.3.2 Surfaces

The surface science approach has a second draw-back: the materials gap. Real nanoparticles have a large variation in surface orientations. Small particles have a relatively large number of steps and kinks (defect sites) compared to larger particles. Interpreting results from real nanoparticles is very difficult because of the large variation in facets. Therefore, well-ordered single crystal surfaces are often used in surface science. Flat surfaces such as Pt(111) (hexagonal surface structure, figure 1.3a), Pt(100) (square structure, 1.3b), and Pt(110) (rectangular structure, 1.3c) have been studied extensively. However, defect sites are thought to be more active in bond breaking and making reactions⁹. To study the influence of steps on the reaction, stepped (see chapter 5 and 6) or curved single crystals can be used.

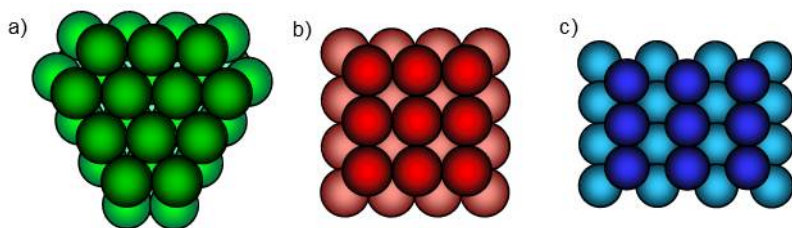


Figure 1.3: Schematic view of the a) (111) (hexagonal atomic arrangement), b) (100) (square), and c) (110) (rectangular) surface structures.

1.4 Scope of this thesis

The focus of this thesis is on the dissociation of O_2 on Pd and Pt and the hydrophobic/hydrophilic interaction of water with deuterium-precovered Pt. The breaking of the oxygen-oxygen bond is an important step for various reactions, such as the CO oxidation in the three-way catalytic converter and the catalytic oxygen reduction in the PEMFC. Most real catalytic processes involve more than one reactant that is in contact with the catalytic surface. In the PEMFC, water, hydrogen, and oxygen are present. Therefore, it is interesting to study the interaction between water, deuterium, and the surface. We use single crystal surfaces and supersonic molecular beam and UHV techniques to improve our knowledge on these systems.

In chapters 3 and 4, oxygen dissociation on the flat Pd(100) crystal as a function of incident energy (E_i), surface temperature (T_s), and incident angle is studied. The focus of chapter 3 is on the initial sticking probability of oxygen on Pd(100). The results are compared to Pd(111) and Pd(110). The results provide insight on the dissociation mechanism in the zero-coverage limit. In chapter 4, the sticking of oxygen on Pd(100) as function of coverage and oxygen desorption in the subsequent TPD experiments are studied. The dissociation process changes with increasing oxygen coverage. The obtained maximum oxygen coverage depends on both surface temperature and incident energy.

Oxygen dissociation as function of E_i , T_s , and angle is also studied on the stepped Pt(553) single crystal (chapter 5). We compare our data to the flat Pt(111) and stepped Pt(533) surfaces to study the influence of step sites. Pt(553) and Pt(533) have a comparable terrace width, but a different step type. The presence of step edges leads to a higher reactivity than on the flat surface. Depending on kinetic energy, the step type also plays a role in the oxygen sticking and dissociation

processes.

In chapter 6, co-adsorption of water and deuterium on stepped Pt surfaces with the (100) step type is studied. Earlier studies showed that the deuterated Pt(533) surface is hydrophobic, while D/Pt(111) and D/Pt(553) are hydrophilic. It was expected that a larger terrace separated by (100) steps might reduce the hydrophobicity. We compare the Pt(533) surface to Pt(755), Pt(977), and Pt(111) and find that even 8-atom wide terraces do not resemble the 'ideal' (111) surface.

Chapter 7 provides an outlook on future experiments and proof-of-principle for double molecular beam experiments. We show that reactions can take place on stepped surfaces when one gas is provided by the supersonic molecular beam and the other by the effusive beam. We can form HD from H₂ and D₂ on Pt(553) and HOD from O₂ and a mixture of H₂ and D₂ on Pt(533). The effect of step type and step density will be studied on curved single crystals in the future.

Chapter 2

Experimental set-up and techniques

2.1 The set-up

The experiments were performed using an ultra-high vacuum (UHV) apparatus named Lionfish. The main chamber has a base pressure of $< 1 \cdot 10^{-10}$ mbar during experiments and contained a LEED/Auger Electron Spectroscopy device (LK Technologies, RVL 2000/8/R), a fixed quadrupole mass spectrometer (QMS, Pfeiffer QMA 200), a sputter gun and various leak valves (experiments in chapter 6). Later, the machine was extended with a double differentially pumped supersonic molecular beam, a single differentially pumped effusive beam, and a quadrupole mass spectrometer (UTI 100C) which can be moved along the molecular beam axis for time-of-flight (TOF) measurements (for experiments in chapter 3, 4, and 5). The crystal is suspended from a liquid nitrogen cooled cryostat on an x, y, z, θ manipulator. The crystal temperature can be controlled between 84 and 1200 K with the use of liquid nitrogen for cooling and radiative heating combined with electron bombardment for heating.

A schematic side view of the supersonic molecular beam is shown in figure 2.1. The main UHV chamber (left) can be separated from the other chambers by the slide. The slide can be set to one of three orifices (diameter of 6.2 mm, 3.2 mm and 1.8 mm) or the slit (for future measurements on curved crystals).

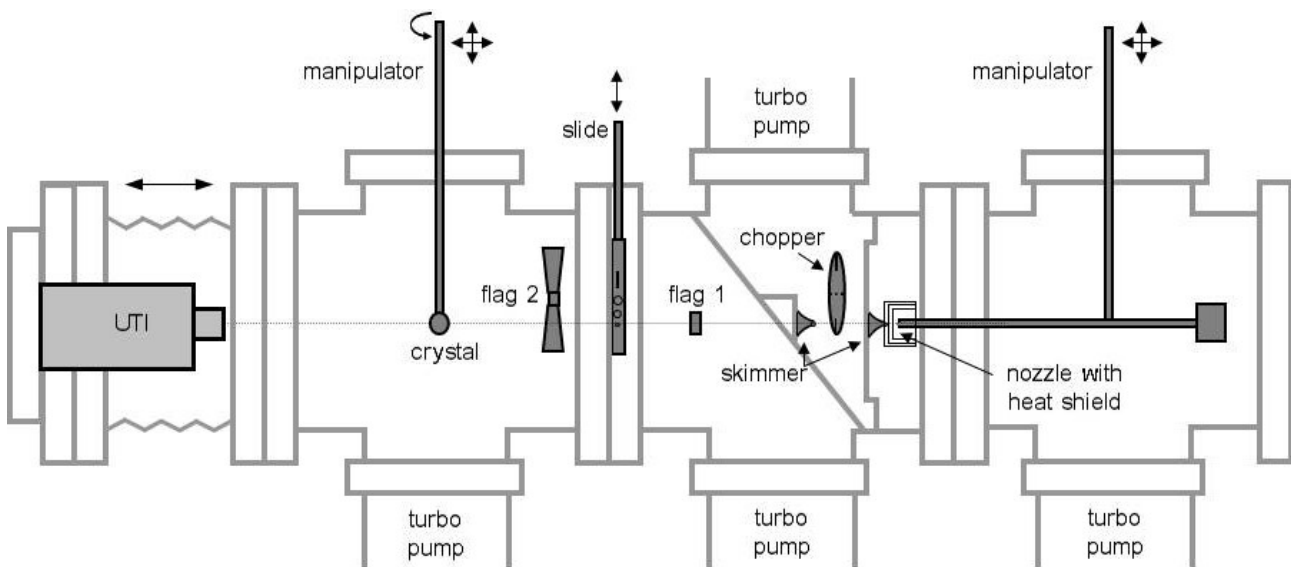


Figure 2.1: Schematic side view of the supersonic molecular beam parts.

The beam was created by continuous expansion of gas mixtures at 0.5-4.7 bar through a tungsten nozzle. The nozzle has a circular 45 μm diameter orifice and can be heated by two filaments. A heat shield protects the rest of the machine from overheating. The beam enters from the right and is shaped by a set of skimmers (diameter of 2.5 mm and 0.45 mm). Two flags (one in the second differential and one in the UHV chamber) and the chopper wheel (first differential chamber) modulate the beam. The two flags are used to determine the sticking probability with the King and Wells (KW) technique⁸ (see chapter 2.2.4). The chopper wheel is a fast rotating disk (~ 250 Hz) with two broad (17 mm) and two narrow slits (0.85 mm, 16% total duty cycle). It is used to determine the kinetic energy (E_i) of the beam with the time-of-flight (TOF) technique (see section 2.2.3). The incident kinetic energy of the molecular beam was controlled by seeding or antiseeding with helium (Linde, 6.0) or argon (Air Products, 5.7) and by heating the nozzle. Exposure of the crystal to the beam is continued until the exposed surface area has reached a maximum coverage. A temperature programmed desorption (TPD) experiment was performed after each adsorption experiment.

The procedures of the crystal cleaning and the experiments are described in the experimental part of the following chapters. Cleanliness of the crystals was checked regularly by monitoring additional masses (such as $m/e = 2$ (H_2), 18 (H_2O), 28 (CO or N_2), 32 (O_2), and 44 (CO_2) in desorption experiments and repeating experiments under identical conditions. Surface structure was confirmed by low energy electron diffraction (LEED, see chapter 2.2.1).

2.2 Techniques

2.2.1 Low energy electron diffraction

Low energy electron diffraction is a technique that can be used to determine the surface structure. The low energy electrons hit the surface, the electrons are scattered back elastically in all directions. The well-ordered structure of the surface creates an interference pattern, which can be visualized on the fluorescent screen. The pattern on the screen is a reciprocal lattice. Small interatomic distances show up as a large distance between the fluorescent spots, and the other way around.

Stepped surfaces show splitted spots on the screen. The direction of the multiplet is perpendicular to the steps¹⁰. The spot row to spot splitting ratio is a measure

of the average terrace length on the crystal. The step height can also be determined by LEED¹¹. Depending on the electron energy, the (00) spot shows either as a singlet or as a doublet. A fit for the first singlet or doublet should be compared to the theoretical energy. The best fit indicates if the steps are of single atomic height, or of double atomic height.

A good LEED device can also be used to determine the structure of ordered adsorbate layers. Unfortunately, the quality of the available LEED on our system is such that we were only able to use it to confirm the surface structure of our crystals and the azimuthal orientation relative to the plane containing the surface normal and the molecular beam.

2.2.2 Temperature programmed desorption

Temperature programmed desorption is a simple, yet very useful surface science technique. It can provide information about the binding energy of the molecule to the surface, the order of the reaction, and the surface coverage. For TPD experiments, molecules are adsorbed to the surface by background dosing (chapter 6) or by using the supersonic molecular beam (chapter 3-5). The sample is heated with a linear temperature ramp:

$$T_s = T_0 + \beta t \quad (2.1)$$

where T_s is the surface temperature, T_0 the initial surface temperature, β the heating rate, and t the time. The heating rate in this thesis varies between 1 and 4 K/s and is mentioned in the upcoming chapters when necessary. At a certain temperature, the bonds between the surface and the adsorbates are broken, the molecules desorb and are detected by the mass spectrometer.

The desorption process can be described by the Polanyi-Wigner equation¹²:

$$r(\theta) = -\frac{d\theta}{dt} = \nu(\theta)\theta^n e^{-E_d(\theta)/RT} \quad (2.2)$$

where r is the rate of desorption, θ the surface coverage, ν the pre-exponential Arrhenius factor, n the order of desorption, E_d the activation energy, and R the gas constant.

The binding energy depends on the type of adsorbed molecules, the type of metal of the crystal, the surface structure, the presence of defect sites and co-adsorbates, and the adsorbate coverage. A higher binding energy results in a higher desorption temperature. The broadness of the desorption peak is indicative of the attractive or repulsive interaction between the adsorbed molecules. The order of the reaction can be determined by dosing different amounts of molecules on the surface¹³. Zeroth-order reaction kinetics can result from an equilibrium between a condensed phase and a 2-dimensional gas phase, from which molecules can desorb. The TPD spectra are characterized by overlapping onsets with a maximum peak temperature that shifts to higher temperatures with increasing coverage. First-order reaction kinetics show no temperature shift when the coverage increases. The desorption rate is proportional to the surface concentration. Second-order kinetics (recombinative desorption) show a peak that shifts to lower temperatures with increasing coverage. The involvement of two atoms leads to a desorption rate that depends on the coverage squared. The relative number of molecules that was present on the surface (coverage) can be determined by integrating the TPD spectrum. TPD can also be used to check if the surface was clean, as the shape of the TPD spectrum often changes when other molecules are present on the surface¹⁴.

2.2.3 Time-of-flight

The time-of-flight method is used to determine the kinetic energy of the molecules in the supersonic molecular beam. TOF spectra are measured with the quadrupole mass spectrometer (UTI 100C). The QMS can be moved along the beam axis in order to vary the distance to the chopper wheel. The chopper wheel spins at a frequency of ~ 250 Hz and has two broad and two narrow slits. The optical sensor triggers a multichannel scaler card (turbo MCS, EG&G Ortec) when a slit passes the sensor. During the measurements, the chopperwheel is rotated $15/8$ turns before starting a new scan, resulting in 3 or 4 large and small peaks (depending on the timing of the trigger). Usually 10000 to 30000 scans are summed to obtain a spectrum as shown in figure 2.2.

The QMS is moved along the beam axis over a distance of 46 mm in 6 steps. When the QMS is moved further away from the chopper wheel, it takes a longer time for the molecules to reach the detector. The peaks shift to the right. The difference in flight path vs. flight time can be used to determine the average speed and kinetic

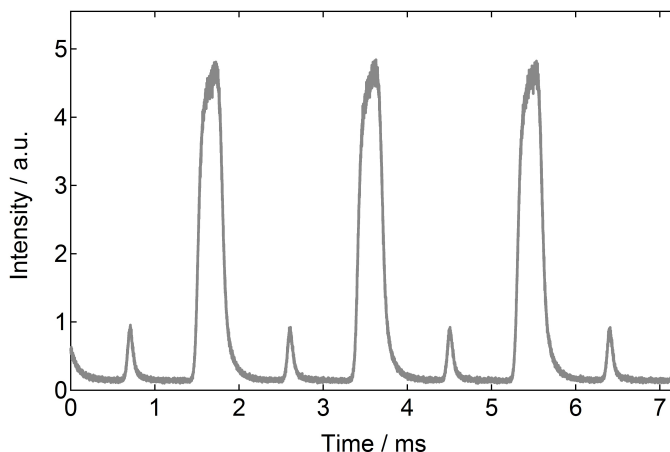


Figure 2.2: A typical time-of-flight spectrum of O_2 in the supersonic molecular beam. As the chopper wheel almost spins two times, the spectrum shows both large and small peaks of the wide and narrow slits.

energy of the molecules. Only the small peaks are used for the analysis, as the large ones are not as well defined. Oxygen is mixed with helium and/or argon to increase or decrease the speed of oxygen. The oxygen molecules and the seed gas molecules do not have the same speed in the beam. This is known as the velocity slip.

A more detailed analysis can be made to estimate the velocity distribution and delay times. For this method, the chopper gating function should be taken into account. The chopper spins fast and has narrow slits, yet there is still a transition before and after complete opening of the slit to the beam. This method is not described in this thesis.

2.2.4 King and Wells

The sticking probability (reaction probability) of O_2 on Pt or Pd single crystals can be determined with the King and Wells technique⁸. Figure 2.3 shows the different steps of a KW experiment. In the first stage, both flags along the supersonic molecular beam are closed, a background pressure of O_2 is measured by the QMS. After 5 seconds, the first flag (in the differentially pumped stage) is opened. The beam enters the main chamber, without impinging onto the sample and the oxygen partial

pressure increases, P_{rise} . The pressure is allowed to stabilize for 10 seconds, before the second flag (in the UHV main chamber) is opened. Oxygen molecules adsorb on the surface, which results in a temporary decrease of the partial pressure, P_{drop} . After a certain time, the partial pressure increases again as the surface coverage increases. The initial sticking probability (S_0) is determined by:

$$S_0 = \frac{P_{drop}}{P_{rise}} \quad (2.3)$$

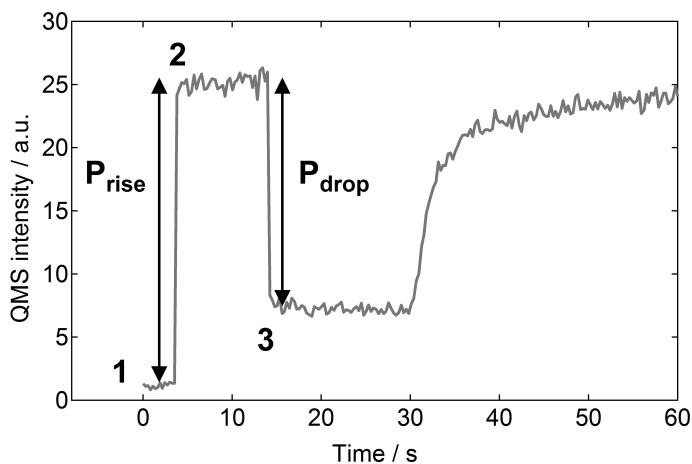


Figure 2.3: Determining the sticking probability with the King and Wells technique. The steps are explained in the text.

The reactivity of oxygen on Pd(100) was very high. In order to obtain a good estimate of the real initial sticking probability, an extrapolation method was used as described in the experimental section of chapter 3. The S_0 (first few seconds after opening the second flag) can be plotted against incident energy, surface temperature, or incident angle. The sticking probability changes over time, as the oxygen coverage increases. The complete KW experiment also provides useful information on the adsorption process as function of coverage.

Chapter 3

Reaction dynamics of initial O₂ sticking on Pd(100)

Abstract

We have determined the initial sticking probability of O₂ on Pd(100) using the King and Wells method for various kinetic energies, surface temperatures, and incident angles. The data suggest two different mechanisms to sticking and dissociation. Dissociation proceeds mostly through a direct process with indirect dissociation contributing only at low kinetic energies. We suggest a dynamical precursor state to account for the indirect dissociation channel, while steering causes the high absolute reactivity. A comparison of our results to those previously obtained for Pd(111) and Pd(110) highlights how similar results for different surfaces are interpreted to suggest widely varying dynamics.

This chapter is based on: A. den Dunnen, S. Wiegman, L. Jacobse, and L.B.F. Juurlink, *J. Chem. Phys.*, 2015, **142**, 214708.

3.1 Introduction

Dissociative adsorption of O_2 on metal surfaces is a poorly understood but crucial elementary reaction step to many heterogeneously catalyzed oxidation reactions. Various recent reviews discuss the current level of understanding for prototypical metals, e.g. Al, Pt, Cu, Ag, and Pd^{15–17}. Complications in theoretical approaches to accurately describe O_2 dissociation dynamics arise from the high reaction energy that needs to be dissipated into electron-hole (e-h) pairs and/or phonons, and a quenching of the triplet spin state upon dissociation¹⁵.

O_2 dissociation on Pt(111) is one of few systems studied experimentally and theoretically in great detail^{18–23}. The reaction has been shown to occur solely via an indirect mechanism^{19,21,24}. Stable, molecularly bound chemisorbed states labeled as superoxide (O_2^-) and peroxide (O_2^{2-}) were identified spectroscopically as the only species on the surface, even at high impact energies¹⁹. The dissociation of such systems may then be treated by a kinetic model assuming equilibrated states²⁵. Figure 3.1 displays a 1-dimensional (1-D) potential for interaction of an O_2 molecule with a surface, containing both a physisorbed and chemisorbed well, as originally proposed for O_2/Ag ²⁵, but here modified to have a lower barrier to dissociation than to desorption²⁶. In the absence of a significant influence of a physisorbed state, an experimentally determined temperature dependence to dissociation on Pt(111) was used to extract the difference between the desorption energy and the barrier to dissociation from the molecular state (ΔE_{act})^{24,26}. The adsorption energy of the molecular and atomic states ($\Delta E_{O_2,chem}$ and $\Delta E_{2O_{ads}}$) may be derived from e.g. single crystal adsorption calorimetry (SCAC) and temperature programmed desorption (TPD). Such data yield references for theoretical studies that map the potential energy surface (PES) for the same system.

The effect of molecular precursor states on the dissociation dynamics as probed by molecular beam techniques is dependent on their location and depth within the full PES^{27,28}. Obviously, both parameters change with the identity of the metal and surface structure. Moving from Pt to Pd, the reaction energy for dissociation of O_2 increases²⁹. As the atomic well depth increases, the barrier between the atomic and molecular state is lowered unless the molecular state is stabilized by the same amount. Motion of the molecular state along the reaction coordinate also affects the barrier. Hence, in moving from Pt to Pd, the relevance of the molecular precursor state may alter or remain the same. For Pd(111), spectroscopic identification of

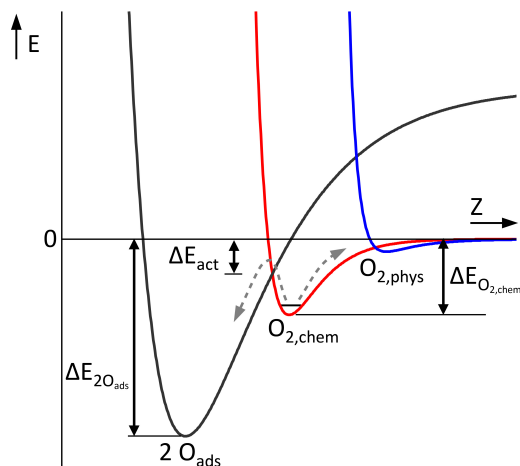


Figure 3.1: Schematic 1-D representation of a potential energy surface for O_2 dissociation on a metal surface. The blue line indicates the O_2 physisorption well ($\text{O}_{2,\text{phys}}$), the red line the O_2 chemisorption well ($\text{O}_{2,\text{chem}}$), and the black line the dissociated oxygen well (O_{ads}).

$\text{O}_{2,\text{chem}}$ and molecular beam studies indicate that dissociation occurs via an equilibrated molecular O_2 state similar to $\text{Pt}(111)$ ³⁰. A theoretical study using *ab initio* local spin density calculations agrees²⁹.

For $\text{Pd}(100)$, an electron energy loss spectroscopy (EELS) study finds that on the bare surface O_2 dissociates even at 10 K ³¹. At higher exposures, but prior to completion of the $p(2 \times 2)$ surface structure at 0.25 monolayer (ML) coverage^{31–38} molecularly adsorbed oxygen is observed^{31,33}. This may be taken to imply that there is no significant barrier between an adsorbed molecular and dissociated state for oxygen on the bare surface. The appearance of a molecular state on $\text{O}/\text{Pd}(100)$ may result from a significant change in its binding energy due to the presence of atomic oxygen in a next-nearest neighbor (NNN) site on the surface. It could also reflect a metastable molecular state on the bare surface that is not significantly changed, but cannot dissociate as a result of site blocking at the nearest neighbor (NN) site.

Various cuts through high dimensionality PESs for $\text{O}_2/\text{Pd}(100)$ were recently published independently by two research groups^{39–41}. Both PESs show a deep molecular chemisorption well located at the fourfold hollow site with the internuclear O_2 axis pointing toward bridge sites. The molecular state has a binding energy of

~ 1.5 eV per O_2 . The deep molecular well is located at a short distance from the surface and stretched along the O-O internuclear distance axis^{40,41}. Hence, the barrier to dissociation is purely located in the exit channel. Barrier heights of 120³⁹ or ~ 200 meV⁴¹ separate the molecular state from the dissociated state. The dissociation occurs by motion of both O atoms across opposite bridge sites. Meyer and Reuter find the dissociation to release 2.6 eV per O_2 in total, very little of which is coupled non-adiabatically to e-h pair excitation⁴⁰. Dynamical calculations indicate that most of the dissipated energy is quickly absorbed by a heat bath, while the O atoms retained a significant amount of kinetic energy after dissociation⁴². Coverage dependent calculations of the barrier to dissociation from the molecular state by Liu and Evans indicate that increased occupancy of NNN sites of the fourfold hollow where O_2 adsorbs both weakens the adsorption energy of the molecular state and increases the barrier to dissociation³⁹. Other cuts of both PESs with the O_2 internuclear axis (nearly) parallel to the surface suggest the presence of modestly-activated dissociative adsorption pathways at bridge and top sites^{39,41}. At other locations and for other angles between the surface and the molecular axis, the PES becomes strongly repulsive. The cuts through the potential therefor imply a high level of corrugation. Hence, this PES exhibits interesting characteristics that may be probed experimentally.

Here, we present our results from an investigation into the dissociation dynamics of O_2 on Pd(100) using supersonic molecular beam techniques. General trends in sticking probability (S_0) observed as function of incident kinetic energy (E_i), surface temperature (T_s), and incident angle (θ) dependencies are discussed in terms of possible sticking and dissociation mechanisms. Our results are also compared to those for other low-Miller-index Pd surfaces. We suggest implications for the aforementioned and future theoretical studies of O_2 /Pd(100).

3.2 Experimental

3.2.1 The apparatus

Experiments were performed using an ultra-high vacuum (UHV) apparatus (base pressure $< 1 \cdot 10^{-10}$ mbar) equipped with a double differentially pumped supersonic molecular beam and a single differentially pumped effusive beam. These beams intersect at the surface of a sample that is suspended from a liquid nitrogen cooled

cryostat on an x, y, z, θ manipulator. The UHV chamber also contains a fixed quadrupole mass spectrometer (Pfeiffer, QMA 200) for TPD, residual gas analysis (RGA), and King and Wells (KW) measurements, a quadrupole mass spectrometer (UTI 100C) which can be moved along the molecular beam axis for time-of-flight (TOF) measurements, a LEED/Auger (RVL 2000/8/R) apparatus, a sputter gun, and various leak valves.

Supersonic molecular beams were created by continuous expansion of gas mixtures at 0.5-4.7 bar through a tungsten nozzle with a circular $45\text{ }\mu\text{m}$ diameter orifice at room temperature. A beam was shaped by a set of three skimmers separating the source, two differential, and one UHV chamber. Flags in the second differential and UHV chamber and a chopper wheel in the first differential chamber modulate the beam. The incident kinetic energy of the molecular beam was controlled by seeding or antiseeding with helium (Linde, 6.0) or argon (Air Products, 5.7). The (spread in) kinetic energy of the O_2 in our beams was determined by TOF. The (initial) sticking probabilities were determined using the King and Wells technique⁸. Exposure of the crystal to the beam is continued until the exposed surface area has reached a maximum coverage. Coverage dependent sticking and our subsequent TPD experiments are discussed in chapter 4.

3.2.2 The Pd(100) crystal

Initially, we employed a Pd(100) single crystal that was previously used in high-pressure CO oxidation studies^{43,44}. The crystal was extensively cleaned by repeated cycles of Ar^+ bombardment (Messer, 5.0; $15\text{ }\mu\text{A}$, 5 min.), annealing at a surface temperature of 900 K in an oxygen atmosphere (Messer, 5.0; $3.5\cdot 10^{-8}$ mbar, 3 min.), and 3 minutes of vacuum annealing at a surface temperature of 1200 K. The surface cleanliness was confirmed by comparison of known TPD spectra for H_2 and O_2 . We did not observe any significant CO formation in temperature programmed reaction when titrating the cleaned surface with O_2 . Long-range surface order was confirmed by low energy electron diffraction (LEED). In between subsequent KW measurements, the crystal was vacuum annealed for 3 minutes at a temperature of 1200 K. Consistency of results was checked by regularly repeating an experiment under identical conditions. After obtaining an initial set of data for $S_0(E_i)$, an unexpected weak dependence on incident energy caused concerns regarding the quality of the crystal. Hence, we repeated all experiments on a newly-purchased Pd

single crystal. This second crystal was cut and polished to expose the (100) plane to $< 0.1^\circ$ accuracy (Surface Preparation Laboratory, Zaandam, The Netherlands). After an initial extensive cleaning procedure, no significant differences between the results from our two crystals were observed when using the same procedures for cleaning and determining S_0 . The measurements on the new crystal were extended to include surface temperature and angle dependencies. The kinetic energy and surface temperature dependencies were also determined a second time with an interval of almost two years. Minor variations (< 5 -10% depending on kinetic energy) in averaged absolute sticking probability for multiple measurements were found between these two data sets.

3.2.3 S_0 determination

Reactive molecules may cause difficulties in obtaining correct values for S_0 as the walls and filaments in the UHV chamber can act as pumps in parallel to the surface of interest⁴⁵. Figure 3.2 illustrates that our S_0 measurements suffer somewhat from a transient observed in the first second after the cleaned and very reactive Pd(100) is exposed to a supersonic molecular beam containing O_2 . The insets of figure 3.2 show the actual O_2 KW traces for (a) $E_i = 0.42$ eV and (b) 0.058 eV at a surface temperature of 100 K and normal incidence. They also present two extremes in the variation of KW trace shapes. The KW traces are background corrected, inverted, and scaled between 0 and 1 to yield the time-dependent sticking probability curves. The latter are shown, expanded between 0 and 5 seconds, in the main figure.

The transient behavior in the first second may result from various convolutions. The time required to fully ‘open’ the beam by removal of the main chamber flag is only ~ 3 ms. The transient is therefor most likely an artifact resulting from our system’s vacuum time constant for O_2 (~ 55 ms) and possibly a change in the effective pumping speed when allowing the beam to impinge upon the highly reactive Pd(100) surface. For high kinetic energies and/or high surface temperatures, the transient leads to an underestimation of S_0 if we were to take the highest point on the sticking over time ($S(time)$) trace. We have attempted to eliminate the transient by reducing the O_2 flux. However, reducing the beam to a maximum of 8% O_2 , retracting the nozzle from the first skimmer, and chopping the beam at ~ 250 Hz using a chopper wheel with a 16% duty cycle did not remove it. Hence, we obtain S_0 by extrapolating a linear section of $S(time)$ to the exact time where the second flag

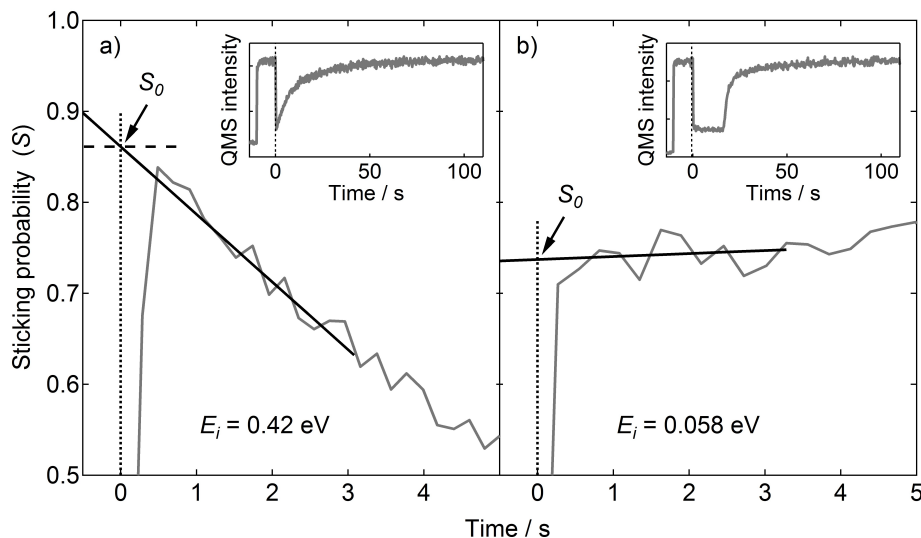


Figure 3.2: Time-dependent sticking traces for O_2 on Pd(100) at normal incidence and $T_s = 100$ K for (a) $E_i = 0.42$ eV and (b) 0.058 eV. The reported values for S_0 are determined by extrapolation to the exact time of opening of the second flag. Original KW traces are shown as insets.

opens. Figure 3.2 illustrates this procedure. For high kinetic energies and surface temperatures it increases S_0 on the order of 0.05 relative to the highest point on the S_0 trace, whereas it does not affect the value obtained for low kinetic energies and low surface temperatures. Values for S_0 reported here are averaged values of multiple measurements using the second Pd(100) crystal described above. The maximum standard deviation in S_0 of multiple measurements within a single data set was found to be 0.026. For the energy dependence, measurements were performed 2 to 6 times and repeated regularly during a single or multiple days. The spread in incident energy for a single beam is typically less than 20% of the incident energy. For one single beam of 0.32 eV, a larger energy spread of almost 50% was found.

The sticking probability is very high, but does not reach unity even at high incident energy. We have verified that this is not a consequence of contamination picked up by the crystal in between cleaning and starting the KW experiment. Predosing H_2 , i.e. the dominant residual gas, for 60 seconds at $1 \cdot 10^{-9}$ mbar causes a decrease in S_0 of 0.15 for the surface at 100 K. It does not influence the S_0 for the

400 K surface. Considering the H_2 partial pressure and typical time lag, we underestimate S_0 only for surface temperatures below 400 K and at most by a couple of percent.

3.3 Results and discussion

Figure 3.3 visualizes the trends of $S_0(E_i, T_s, \Theta)$ for O_2 on Pd(100). The blue and red lines indicate a surface temperature of 100 K and 400 K, respectively. The actual data are shown in figures 3.4, 3.5, and 3.6. To create figure 3.3, we have used a polynomial fit to reflect the energy dependence. We have used all data from two data sets gathered over a two year time span for the new crystal in the fitting procedure. For the angle dependence, we have used a cosine fit. Here only one data set was available. The additional light blue curve in the 0.42 eV plane reflects the expected angle dependence if normal energy scaling would be observed using the data for $T_s = 100$ K to fix S_0 at normal incidence.

We summarize characteristics of the general trends observed in figure 3.3. First, the $S_0(E_i)$ dependence (detailed in figure 3.4) shows a slight initial decrease with increasing incident energy. Thereafter, a gradual increase is observed that seems limited to a maximum value near 0.9. Second, S_0 is nearly independent of surface temperature over the entire energy range. The minor dependence appearing in figure 3.3 is actually caused by site-blocking from residual H_2 dissociation occurring while the crystal cools to 100 K. We have verified experimentally that H_2 pre-dosed on purpose at 100 K lowers S_0 . The second data set probing temperature dependence is shown in figure 3.5, was taken after our crystal's cooling rate had been improved significantly. It shows no significant T_s dependence over the entire energy range from 100 K to 400 K and from 0.056 to 0.38 eV. Third, we observe two opposite angle dependencies (also shown in figure 3.6) at low and high incident energies. At low incident energy and $T_s = 400$ K, there is no angle dependence, while at 100 K, S_0 even slightly increases with angle. At higher kinetic energies, the angle dependence reverses and weakly resembles normal energy scaling. Note that our crystal rotates along an axis 27° away from $[011]$ in the direction of $[0\bar{1}1]$.

These trends are explained by two parallel dissociation mechanisms, whose contribution depend on incident energy. At low E_i , an initial decline in S_0 points toward an indirect mechanism or steering. The subsequent increase in S_0 with

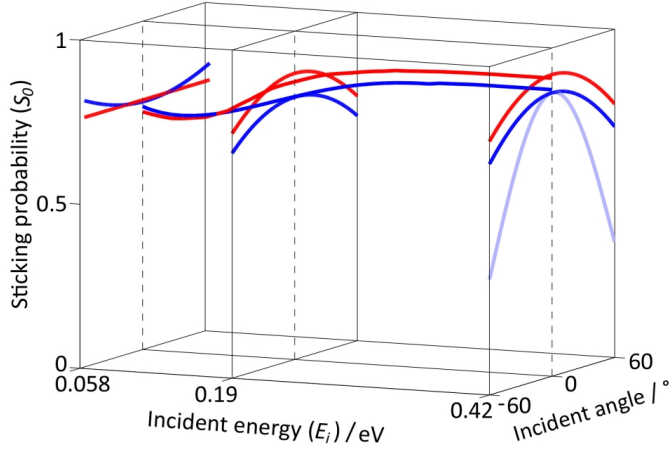


Figure 3.3: A 3-dimensional overview of O_2 S_0 on Pd(100) as a function of E_i (fitted with polynomial function) and incident angle (fitted with cosine function) at $T_s = 400$ K (red lines) and 100 K (blue lines). The light blue line in the 0.42 eV plane shows the normal energy scaling for $T_s = 100$ K.

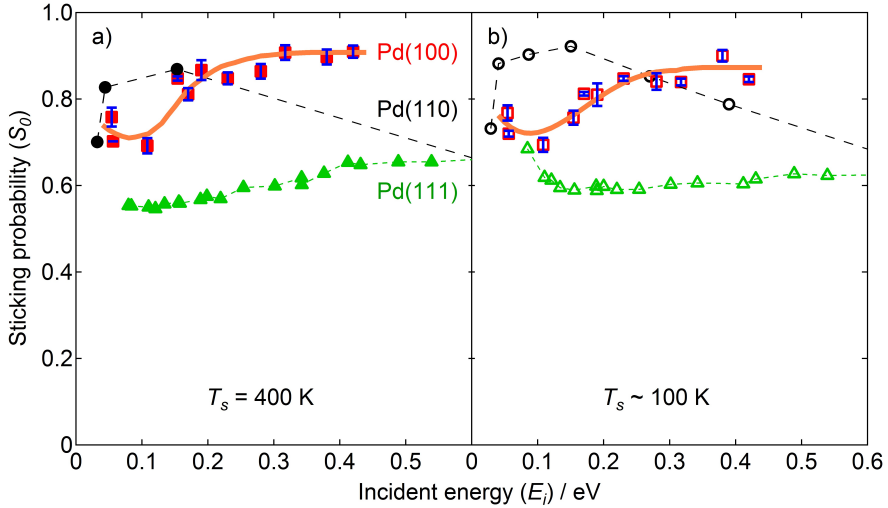


Figure 3.4: S_0 of O_2 on Pd(100) (red squares with blue error bars (standard deviation in y-direction)), Pd(111) (green triangles)³⁰, and Pd(110) (black circles, (b) at $T_s = 102$ K)⁴⁶ as a function of E_i at (a) $T_s = 400$ K and (b) 100 K. Lines are a guide to the eye. They include data for Pd(110) and Pd(111) that fall outside the energy range shown here.

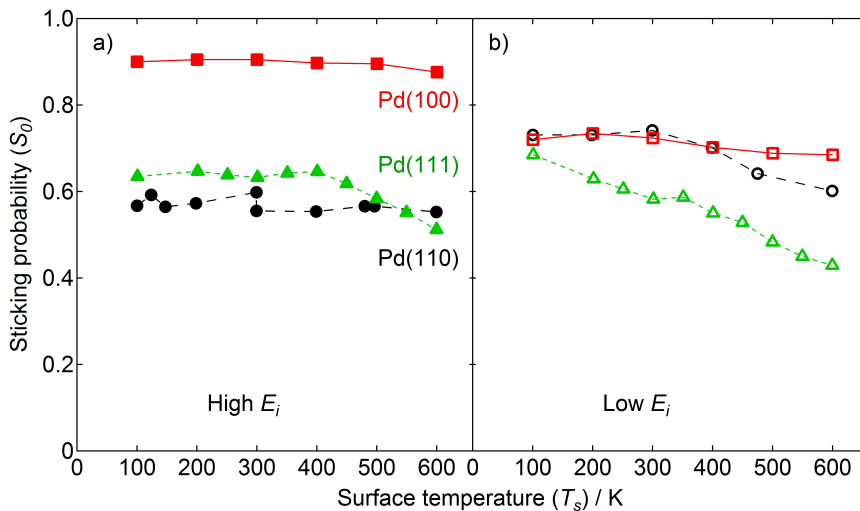


Figure 3.5: S_0 as a function of T_s at (a) high and (b) low incident energy for Pd(100) ($E_i = 0.38$ eV and 0.056 eV, red squares), Pd(111) ($E_i = 0.69$ eV and 0.083 eV, green triangles)³⁰, and Pd(110) ($E_i = 0.84$ eV and 0.032 eV, black circles)⁴⁶.

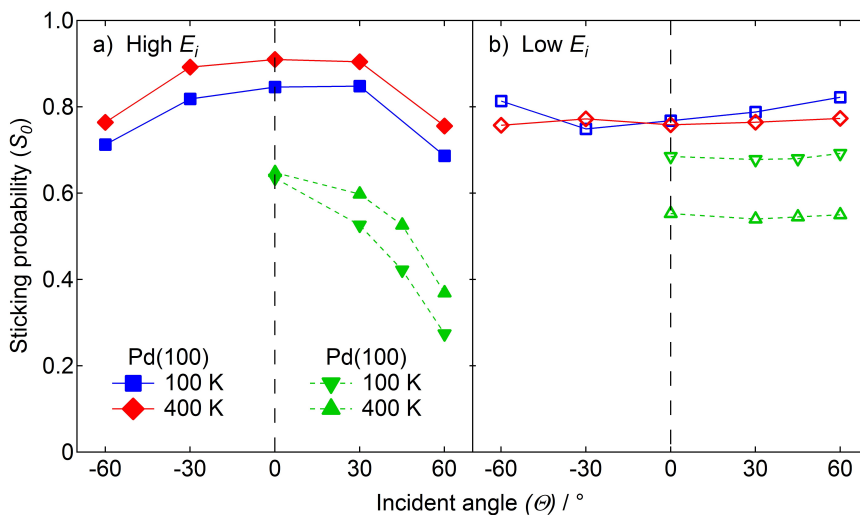


Figure 3.6: S_0 of O_2 on Pd(100) (blue squares at $T_s = 100$ K, red diamonds at 400 K at 0.058 eV and 0.42 eV) and Pd(111) (green point down triangles at $T_s = 100$ K and point up triangles at 400 K at 0.084 eV and 0.69 eV)³⁰ as a function of incident angle for (a) high and (b) low E_i .

E_i suggests an increasing dominance of a direct mechanism that benefits from momentum normal to the surface. We first focus on the indirect mechanism.

An indirect mechanism at low E_i is often ascribed to sticking and dissociation via an equilibrated or dynamic molecular precursor. However, steering may also cause a decline in reactivity^{47–49}. The absence of a temperature dependence in our data argues against an equilibrated precursor. On the other hand, a dynamical precursor mechanism, as suggested to dominate H_2 dissociation on stepped Pt surfaces at low kinetic energies^{50,51}, explains our surface temperature independence. The (near) absence of an angle dependence at low incident energies also agrees with a dynamic precursor mechanism. For H_2 on stepped Pt surfaces, a small linear angle dependence was attributed to the asymmetry of the stepped surface structure^{50,52}. Steering, as argued to strongly influence H_2 dissociation on Pd(100)^{49,53} and O_2 dissociation on Pt(111)^{22,23}, would also not show a surface temperature dependence. However, molecular dynamics simulations for O_2 on Pt(111) show an angle dependence to sticking at all energies while sticking is effectuated by steering. This seems at odds with our observations. However, O_2 sticking on Pt(111) proceeds via an equilibrated molecular state, which is likely positioned elsewhere along the reaction coordinate compared to Pd(100). Hence, we do not consider a different angle dependence a reason to exclude steering as a potential cause for the high reactivity and angle independence. The high level of corrugation actually makes steering likely, particularly at low E_i .

The observed coverage independent sticking probability at 100 K and low E_i , as shown in the inset of figure 3.2b, invites an explanation in terms of sticking via an extrinsic precursor state^{54–56}. Again, our temperature independence at low energy and the aforementioned EELS results argue against a stable molecular state in the zero-coverage limit. The depth of the $O_{2,chem}$ well, as found in the theoretical studies, also makes it unlikely that a physisorbed state is influential to the sticking and dissociation dynamics. In this regard, it is noteworthy that O_2 dissociation on (100) surfaces is generally believed to require two additional empty fourfold hollow sites (8-site model)^{57,58}. For Pd(100), these additional empty sites are on opposite sides across the bridges⁴². If either one is occupied or a NNN site is occupied, the exit channel is hampered or cannot be entered entirely. However, the molecule may equilibrate in the molecular state. In the coverage dependence study of the stability of the molecular state by Liu and Evans³⁹, O_2 is still bound by 0.9 eV when all NNN sites are occupied. The barrier to dissociation has increased from 0.12 eV to 0.4 eV,

while the desorption energy is dropped from 1.5 to 1.3 eV. Hence, we expect that the coverage independence observed in our experiments for low T_s and E_i follows from reducing the ease with which the exit channel to dissociation is reached with increasing coverage, effectively making the metastable molecular state more stable. A drop in sticking from dissociation via a (steered) dynamic precursor state is counterbalanced by scattering and sticking in the molecular state. This ultimately leads to a considerably higher total O/Pd coverage when performing the experiment at 100 K than under conditions that only lead to the $p(2 \times 2)$ structure with the 0.25 ML coverage or higher coverages reported for prolonged exposures^{32,34,36}. Our TPD results are fully in line with this interpretation. TPD spectra even provide evidence of a molecular state that is occupied at high coverage and low surface temperature (see chapter 4). Summarizing, we interpret our data at low E_i in the zero-coverage limit to suggest a gradual, near barrier-free transition of $O_{2,\text{phys}}$, $O_{2,\text{chem}}$, and O_{ads} sites for O_2 on Pd(100). With increased coverage, trapping in the molecular state becomes possible.

When increasing E_i , the weak downward trend in sticking quickly reverses. Such behavior can be explained by an increasingly dominant direct mechanism⁵⁹. Translational energy may help overcome activation barriers along reaction paths other than the minimum energy path. It may also allow for a larger range of trajectories to reach a state from which returning into the gas phase is impossible. A second option is an activated molecular chemisorption pathway. This molecularly chemisorbed state may be a precursor to dissociation. Our observations of a decrease in reactivity with increasing angle, an independence on surface temperature, the previously observed absence of a stable $O_{2,\text{chem}}$ state in EELS studies³¹, and the suggested presence of weakly activated dissociative pathways on other surface sites than the fourfold hollow in density functional theory (DFT) calculations^{39,41} all favor the direct dissociation mechanism. The angle dependence observed for higher kinetic energies may indicate that slightly activated pathways have a barrier positioned toward the entrance channel. They become accessible at increased energy.

We continue with a comparison of the dissociation dynamics for Pd(100) with Pd(111) and Pd(110). The available experimental data of $S_0(E_i, T_s, \Theta)$ for Pd(110)⁴⁶ and Pd(111)³⁰ are reproduced from the literature in figures 3.4, 3.5, and 3.6.

The energy dependence of O_2 sticking on Pd(111)³⁰ shows strong similarities with Pd(100). First, it shows a drop, then a slow rise. The angular dependence also

compares well to our results. However, in contrast to Pd(100), S_0 for Pd(111) shows a strong dependence on surface temperature. At low energy, S_0 decreases fast over the entire temperature range. At high energy, it is independent of T_s up to 400 K beyond which S_0 decreases. Here, the drop can not be ascribed to a competing onset of associative desorption⁶⁰. The observations for Pd(111) were explained by sequential physisorbed and chemisorbed precursor states for low E_i , while at high E_i O₂ directly chemisorbs as a molecule. Direct dissociation was not observed for energies up to 0.69 eV. Theoretical calculations for this system²⁹ support stable molecular intermediates for this surface. Equilibrated molecular O₂ states were also identified for Pd(111) by EELS⁶¹.

For Pd(110)⁴⁶ the temperature dependencies are similar to Pd(100), but an opposite trend in the kinetic energy dependence is observed. Here, S_0 increases up to 0.16 eV. Although the highest energy data lie outside our axis range, the dashed lines connecting the data show that at higher energies S_0 strongly decreases. These trends were ascribed to a very attractive molecularly chemisorbed precursor state leading to dissociation at low incident energy and a direct activated adsorption channel opening at higher energies. The maximum in S_0 was described as resulting from the sum of these two parallel processes with inverse dependencies on kinetic energy as used in the explanations for trends observed on Pd(100) and Pd(111).

3.4 Summary

For all low-Miller-index Pd surfaces, molecular chemisorbed states are invoked to influence the dynamics of O₂ dissociation. On Pd(111) and Pd(110), the chemisorbed state is considered a stable intermediate. It is directly or indirectly accessible from the gas phase, depending on kinetic energy. The location and depth of its potential well warrant it to be a separate state with barriers between the physisorbed and atomic states. For Pd(100), we find no reason to invoke a stable molecular state in our experiments probing reactivity in the zero coverage limit. Our findings support previous suggestions by other experiments and theory. This implies that the molecular state's location is positioned far along the reaction coordinate and/or is of significant depth when compared to the atomic state. Either argument leads to a loss of a significant barrier between the molecular and atomic states. This implication is reflected in the cuts of the PES and the limited dynamics studies published

to date for O_2 /Pd(100). A deep molecular chemisorbed state would also lead to a lesser importance of a physisorbed state. Steering may be an important ingredient to explain the high reactivity at all kinetic energies.

Although virtually invisible to experiments, the molecular chemisorbed state for O_2 /Pd(100) is of high relevance for two reasons. For the attractive part, it presents an easy path with little corrugation connecting the physisorbed to atomic states. The repulsive part of the molecular state is crucial in the required energy-loss mechanism during the encounter of O_2 with the surface. It is the first encounter of the impinging molecule with the repulsive wall of the molecular state that fully determines whether the molecule loses enough energy to trap it in a dynamic precursor state. Our explanation of the nearly independence of sticking with coverage from counterbalancing reduction of dissociative sticking by scattering into a stabilized molecular state from exit channel blocking, requires that energy transfer must be nearly independent of the local environment. The very slight increase in S_0 with coverage suggests that energy transfer is even better when a molecule happens to impinge on or near a fourfold hollow occupied by O_2 or O. The slight positive angle dependence at the lowest total energies may indicate that the chance to be steered into the metastable molecular state improves when the molecule moves more slowly along the surface normal. The parallel momentum and associated energy for off-normal incidence are very small compared to the energy gain when the molecule enters into the molecular well. It is therefore irrelevant and disappears by the efficient excitation of the in-plane surface-phonon modes when the molecule starts moving up the repulsive wall of the O_2 molecular state⁴². The large loss of energy and excitation of phonon modes upon that first encounter with the surface can be seen in the energy redistribution for a reactive encounter depicted for a reactive trajectory by Meyer and Reuter⁴². Figure 3.7 schematically illustrates our suggestion.

3.5 Conclusion

For Pd(100), we suggest that dissociative adsorption on the bare surface at the lowest incident energy occurs via a dynamic precursor. The efficiency of entering into the molecular state is likely positively affected by steering. With increasing kinetic energy more direct adsorption is favored. This may be caused by an increase in

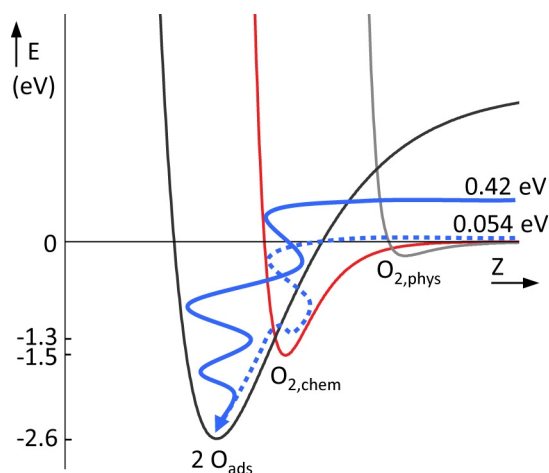


Figure 3.7: Schematic 1-D representation of the potential energy surface for O_2 dissociation on Pd(100). Values of well depth and barrier from^{40,41}. The dashed arrow shows the pathway for molecules with low E_i , the solid arrow for high E_i .

trajectories passing by the metastable molecular state at the fourfold hollow or an opening of modestly activated dissociation pathways at other locations in the unit cell. Although similar trends in reactivity are observed for various low-Miller indices of the same metal, the dynamics of dissociation appear distinctly different. The interpretation of our results is in part based on available cuts of high dimensionality PESs. However, theoretical studies have not quantitatively predicted reactivity for which we now present accurate data. It seems that theoretical dynamics studies will require proper treatment of phonon excitation in order to account for the observed trends. Furthermore, angle and coverage-dependence studies can verify our suggestions regarding the relevance of steering and sticking of O_2 into a stabilized molecular state when coverage increases.

Chapter 4

Thermal desorption and time-dependent adsorption of oxygen on Pd(100)

Abstract

We have studied the thermal desorption and time-dependent adsorption of O_2 on Pd(100) using TPD and the King and Wells technique for various kinetic energies and surface temperatures. Time-dependent adsorption measurements indicate initial O_2 dissociation for all surface temperatures between 100 and 600 K. Below 200 K, molecular oxygen also adsorbs on the atomic oxygen overlayer for incident energies between 0.056 and 0.38 eV. Subsequent heating of the combined O/ O_2 overlayer leads to unexpected high atomic oxygen coverages, comparable to those obtained at high incident energies and high surface temperatures. For adsorption above 200 K, both thermal energy from the substrate and kinetic energy in the gas phase reactant increase the obtained maximum oxygen coverage. We interpret this result to indicate that kinetic energy of O_2 is dissipated by local heating of substrate phonons during the dissociation process. The reaction energy and kinetic energy locally heat the surface and may cause nucleation of high-coverage PdO structures.

This chapter is based on: A. den Dunnen, L. Jacobse, S. Wiegman, and L.B.F. Juurlink, *in preparation*.

4.1 Introduction

Palladium is used as a catalyst material for various oxidation and reduction reactions. A well known example is the CO oxidation reaction in the three-way catalytic converter, where breaking the oxygen-oxygen bond is an important step. The dissociative adsorption and recombinative desorption of O_2 on Pd(100) has been extensively studied experimentally and theoretically^{35–40,42,62–68}.

In chapter 3, we have shown that the oxygen dissociation reaction on Pd(100) proceeds mostly via a direct mechanism. At low energy, a dynamical precursor also contributes to the reactivity and steering causes the high absolute reactivity. At low incident energy and in the zero-coverage limit, the transition of $O_{2,phys}$, $O_{2,chem}$, and O_{ads} is gradual and near barrier-free on Pd(100). With increased coverage, trapping into the molecular state also becomes possible, when the oxygen atoms are blocking the nearest neighbor (NN) sites. This is in line with an electron energy loss spectroscopy (EELS) study^{31,33} that showed that even though oxygen on the bare Pd(100) surface dissociates at a surface temperature as low as 10 K at low coverage, it is also possible for O_2 to adsorb molecularly at higher coverages. Recent DFT calculations³⁹ also indicate a stable O_2 chemisorption well on Pd(100) with pre-adsorbed O-atoms at various coverages.

Density functional theory (DFT) calculations³⁹ showed that the preferred binding site of O on Pd(100) is the fourfold hollow site. The most facile pathway for O_2 dissociation is the pathway, where the flat lying oxygen molecule is centered above the fourfold hollow site. For the minimum energy path, the oxygen dissociates over the two opposite bridge sites. The energy of the dissociated state on the clean surface is lower than that of the molecularly adsorbed state and the reaction energy has been shown to be efficiently coupled into phonons⁴². For a precoverage of 1/8 ML, the energies of the molecular and atomic states are found to be about equal³⁹. At a precoverage of 1/4 ML, the energy of the molecularly adsorbed state is lower than that of the dissociated state. Hence, surface oxidation becomes decreasingly exothermic, but DFT calculations indicate that molecular oxygen adsorbed on the $p(2 \times 2)$ structure (0.25 ML) would still rather dissociate than desorb. Kinetic Monte Carlo (KMC) simulations that take into account the coverage and surface temperature dependencies, show a quasilinear decrease of the normalized sticking coefficient for coverages up to 0.1 ML, almost independent of surface temperature. At surface temperatures above 150 K, the adlayer can equilibrate, so that

an ordered layer with a coverage of 0.25 ML is formed. At a lower surface temperature, the ordering is kinetically limited and a higher coverage of 0.3 ML can be obtained for a dose of 5 L (Langmuir).

Depending on conditions, such as oxygen dose and surface temperature, different overlayer structures can be formed. The chemisorbed $p(2 \times 2)$ (figure 4.1a) and $c(2 \times 2)$ (4.1b) structures and reconstructed $p(5 \times 5)$ (4.1c) and $(\sqrt{5} \times \sqrt{5})R27^\circ$ structures are formed for ideal coverages up to 0.25, 0.50, 0.64, and 0.8 ML, respectively^{32,34,36}. Islands of the structures with higher local coverage are formed before completion of the previous structure.

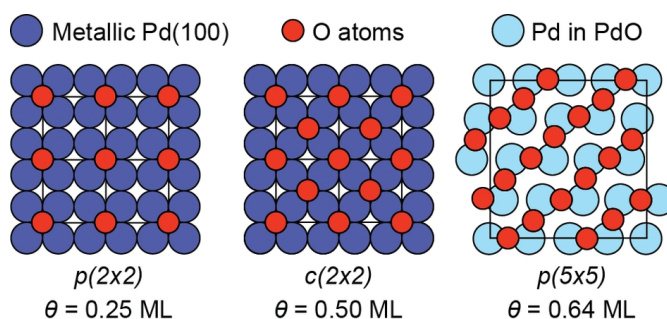


Figure 4.1: Representation of oxygen phases on Pd(100) for various coverages, adapted from³⁶.

Temperature programmed desorption (TPD) studies^{34,36,38,68} show a second order, recombinative oxygen desorption peak around 800 to 850 K (the α -peak, desorption from a disordered layer) for low coverage. At higher coverage, a shoulder develops on the low temperature side (β -peak, $c(2 \times 2)$). A narrow and sharp desorption peak around 620 to 690 K (γ -peak, decomposition of PdO in the $p(5 \times 5)$ and/or $(\sqrt{5} \times \sqrt{5})R27^\circ$ structure) is observed at very high coverages. Since this γ -peak usually develops after dosing at elevated temperatures, the formation of this structure is thought to be activated. Orent and Bader³² find a peak related to $(\sqrt{5} \times \sqrt{5})R27^\circ$ after dosing at 570 K. Chang and Thiel³⁶ do not observe this feature even after dosing at 600 K. They only observe a peak related to $p(5 \times 5)$ after dosing at a surface temperature of 400 K³⁶. Stuve and Madix³⁴ and Zheng and Altman³⁸ already observe the sharp feature of the $p(5 \times 5)$ structure after dosing at a temperature between 300 and 350 K. The last group obtained the $(\sqrt{5} \times \sqrt{5})R27^\circ$ structure after dosing 675 L at 525 K, but also after dosing thousands of Langmuir at 400 K. They also report a weak shoulder at 600 K at very high coverages, which

was ascribed to PdO bulk decomposition. The first three states ($p(2 \times 2)$, $c(2 \times 2)$, and $p(5 \times 5)$) can be removed by the presence of CO in the vacuum chamber over a time span of 15 minutes. The $(\sqrt{5} \times \sqrt{5})R27^\circ$ pattern was still visible after 10 hours at 500 K. It was suggested that variations in the minimum surface temperature needed to obtain the γ -peak may result from differences in the background pressure of CO in the chamber.

It was found before that the nucleation of the reconstructed surface structures depends on the oxygen dose and surface temperature. However, none of the above-mentioned TPD studies include adsorption at different incident energies of the O_2 molecule to unravel how the increasing dissociation barrier for increasing O-coverage is surmounted. Also, these studies did not include surface temperatures below 200 K, where a molecular adsorption state seems possible. In this study, we investigate the role of incident energy (E_i) and surface temperature (T_s) in the range of 100 K to 600 K on the oxygen adsorption and subsequent desorption processes on Pd(100). We use the King and Wells⁸ technique and TPD spectroscopy. We show that the sticking probability over time and the formation of the γ -peak depends on both E_i and T_s . A higher oxygen coverage can also be obtained for surfaces with a temperature of 100 K.

4.2 Experimental

A detailed description of the ultra-high vacuum (UHV) experimental setup is described in chapter 2. The incident kinetic energy of the supersonic molecular beam was controlled by seeding or antiseeding with helium (Linde, 6.0) or argon (Air Products, 5.7). The kinetic energy of the O_2 in our beams was determined by TOF. The sticking probabilities (over time) were determined using the King and Wells technique⁸. Exposure of the crystal to the beam is continued until the exposed surface area has reached a maximum coverage (~ 5 minutes). Each KW experiment was followed by a TPD experiment, with a heating rate of 2 K/s (for the data shown here or 4 K/s for the old data sets). Besides $m/e = 32$ (O_2), $m/e = 2$ (H_2), 16 (O), 18 (H_2O), 28 (CO or N_2), and 44 (CO_2) were recorded regularly to check for contamination.

The Pd crystal was cut and polished to expose the (100) plane to $< 0.1^\circ$ accuracy (Surface Preparation Laboratory, Zaandam, The Netherlands). It was extensively cleaned by repeated cycles of Ar^+ bombardment (Messer, 5.0; 15 μA ,

5 min.), annealing at a surface temperature of 900 K in an oxygen atmosphere (Messer, 5.0; $3.5 \cdot 10^{-8}$ mbar, 3 min.), and 3 minutes of vacuum annealing at a surface temperature of 1200 K. In between subsequent KW measurements, the crystal was vacuum annealed for 3 minutes at a temperature of 1200 K. Consistency of results was checked by regularly repeating an experiment under identical conditions.

The current produced by our channeltron in the QMS changes over the day, resulting in a decrease in sensitivity and thus a lower intensity of KW and TPD signals. We have corrected our TPD traces with the intensity of the accompanying KW traces to the first experiment of the day. With an additional background correction, this resulted in very reproducible integrated TPD areas for all experiments that were repeated during the day. Figure 4.2 shows the scaling procedure for four experiments dosed at 400 K, with $E_i = 0.23$ eV, that were repeated during the day (experiment number 3 (black), 9 (blue), 16 (green), and 26 (red)). The top panels (a and b) show the QMS intensity for KW experiments, the middle panels (c and d) show the integrated TPD areas, and the bottom panels (e and f) show the QMS intensity of the TPD experiments. The gray arrows in panel a show the difference in intensity, used to correct the data in the left panels (a, c, and e). The right panels (b, d, and f) show the corrected KW intensities, integrated TPD areas, and corrected TPD intensities. The TPD integrated areas are now the same within $\sim 4\%$. The KW traces are corrected with a double exponential function to correct for small changes in the tail that change over the day.

In order to convert the TPD integrals to a coverage in ML, we compare the oxygen uptake curves from our KW experiments for low E_i and $T_s = 200$ and 300 K (red solid line) to uptake curves from TPD experiments by Chang and Thiel³⁶ (green dotted line) and Zheng and Altman³⁸ (gray dash/dotted line, only at 335 K) (figure 4.3 and 4.4). Zheng and Altman calibrate the coverage by assuming that the saturation coverage of 0.8 ML is reached when the gamma-peak is saturated. The expected $p(2 \times 2)$ is found at 0.20 ML instead of 0.25 ML in this case. Both groups use background dosing of oxygen, which compares best to our lowest incident energy data. Scaling our low-energy data to a coverage of 0.34 ML results in very comparable uptake curves as previously reported in literature^{36,38}. Note that in case our assumption of 0.34 ML is not correct, the coverage values may change, though it will not affect the observed trends or overall conclusions. Chang also reported uptake curves that were determined by Auger spectroscopy (blue dashed lines). However, these curves never follow the same shape as the TPD and KW uptake curves.

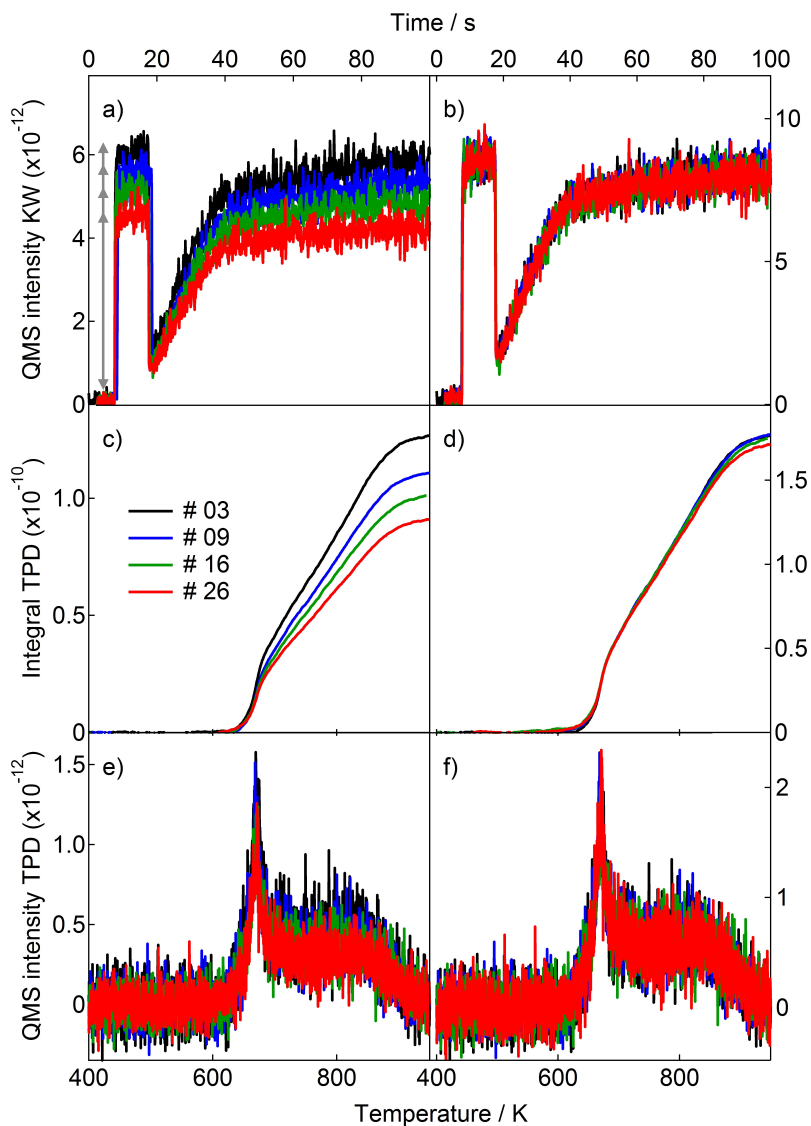


Figure 4.2: Scaling of the QMS intensities for 4 experiments dosed at 400 K and 0.23 eV. Top (a and b) panels: QMS intensity of KW experiments. Middle (c and d): TPD integrated areas. Bottom (e and f): QMS intensity TPD experiments. Right (b, d, and f): corrected data.

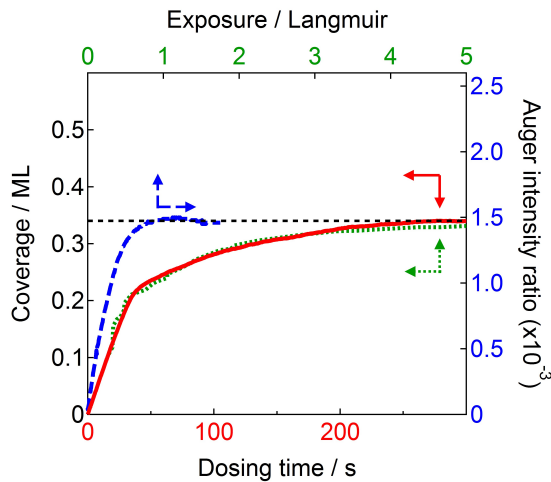


Figure 4.3: Oxygen uptake curve for $T_s = 200$ K for our data (red solid line, $E_i = 0.056$ eV, integrated KW signal) and data by Chang and Thiel³⁶ (green dotted line for TPD integrals, blue dashed line for Auger intensity ($T_s = 180$ K)). Arrows point toward the accompanying axes, the black dashed line indicates 0.34 ML.

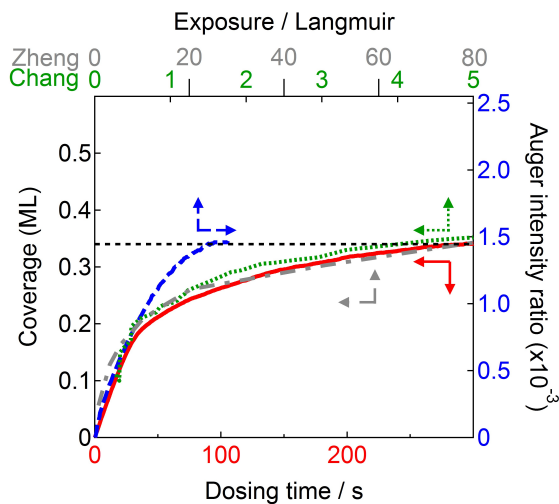


Figure 4.4: Oxygen uptake curve for $T_s = 300$ K for our data (red solid line, $E_i = 0.056$ eV, integrated KW signal), data by Chang and Thiel³⁶ (green dotted line for TPD integrals, blue dashed line for Auger intensity), and data by Zheng³⁸ (gray dash/dotted line for TPD integrals ($T_s = 335$ K)).

Part of the molecules may already desorb from the surface between closing the beam flag and starting the TPD. However, our integrated KW area shows a trend which is comparable to the integrated area for TPD experiments for various T_s and E_i . All beams with different energies have very different intensities and can not directly be compared to each other in KW uptake curves. We have used the least square method to determine the coverage of the KW experiments by comparison to the TPD experiments. We have also compared the TPD shapes of different groups^{36,38,68} to our TPD experiments. A coverage of 0.34 ML (only α and β -peaks and no γ -peak) for the experiment at 0.056 eV and 200 K seems a reasonable coverage. Other techniques could have confirmed if this assumption is valid. Unfortunately, we were not able to determine the coverage via other techniques. Our low quality LEED device was only able to confirm the (100) orientation of our Pd crystal.

4.3 Results

4.3.1 Oxygen adsorption

Figure 4.5 shows the sticking traces over time for a) 0.056 eV, b) 0.17 eV, and c) 0.38 eV at $T_s = 100$ K (blue) and 400 K (gray). At low energy and low temperature, the sticking probability slightly increases over time, stabilizes and eventually decreases exponentially. The trace with a surface temperature of 400 K, also initially increases for almost 10 seconds, as can be seen from the linear fit in this region (black line). After that, it decreases linearly over time. At the highest energy (figure 4.5c), both surface temperatures show nearly identical exponential decreases over time. After 10 seconds, the 100 K trace remains slightly higher than the 400 K trace. At $T_s = 100$ K and intermediate incident energies (figure 4.5b, only 0.17 eV is shown), the KW trace shows two consecutive inflections. S for $T_s = 100$ and 400 K initially drops nearly linearly. For 100 K, a plateau is reached after approximately 20 s whereas for 400 K a lower plateau is reached after 30 s. For 100 K, the second inflection point occurs at approximately 45 s with an exponential-like drop in S . A poorly discernable, but similar inflection and exponential-like drop occurs at 60 s for the 400 K trace.

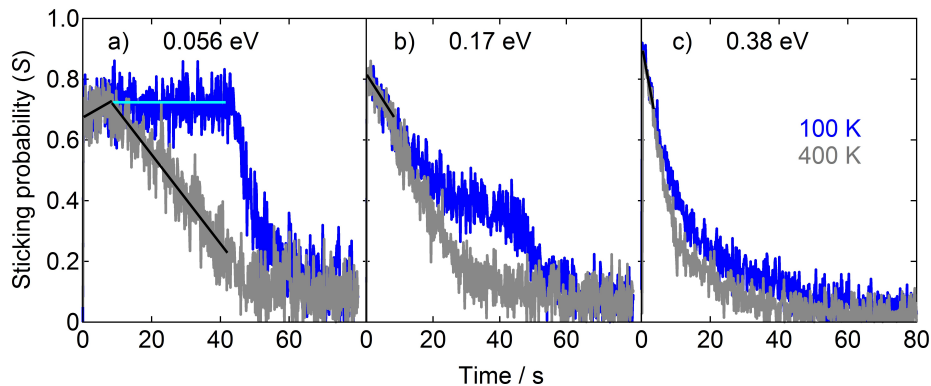


Figure 4.5: Sticking traces over time for a) $E_i = 0.056$ eV, b) 0.17 eV, and c) 0.38 eV at $T_s = 100$ K (blue) and 400 K (gray). The KW traces are reversed in the y direction, scaled between $S = 0$ and 1 , and shifted in the x direction, so that the moment the second flag opens is set to $t = 0$.

4.3.2 Oxygen desorption

Figure 4.6 shows TPD spectra that were collected after the KW experiments with incident energies of a) 0.056 eV, b) 0.23 eV, and c) 0.38 eV for various dosing surface temperatures. All TPD spectra of experiments at $T_s = 100$ K (blue), show a desorption peak between 100 and 200 K (δ -peak). This peak is due to molecular oxygen desorption and increases with increasing incident energy. The peak is absent when a surface temperature higher than 150 K was used. All TPD spectra show a broad desorption feature between ~ 640 and 930 K, due to recombinative oxygen desorption (α and β -peaks). An additional, sharp feature (γ -peak) with a maximum between 670 and 684 K is visible for all energies at a dosing temperature of 100 K. This feature also develops with increasing E_i and T_s . It is absent for all of the low energy TPD spectra between 200 (green) and 600 K (red). At high E_i , the γ -peak is observed for all dosing temperatures. The intensity is largest for 600 K and 100 K and lowest for 200 K.

We have compared the oxygen uptake curves from our KW experiments for $E_i = 0.056$ eV and $T_s = 200$ and 300 K to uptake curves from TPD experiments by Chang and Thiel³⁶ and Zheng and Altman³⁸ (only 335 K) (see Experimental). We have verified that adsorption via the KW experiments and desorption in the TPD experiments follow the same trend for the total obtained coverage. When we scale

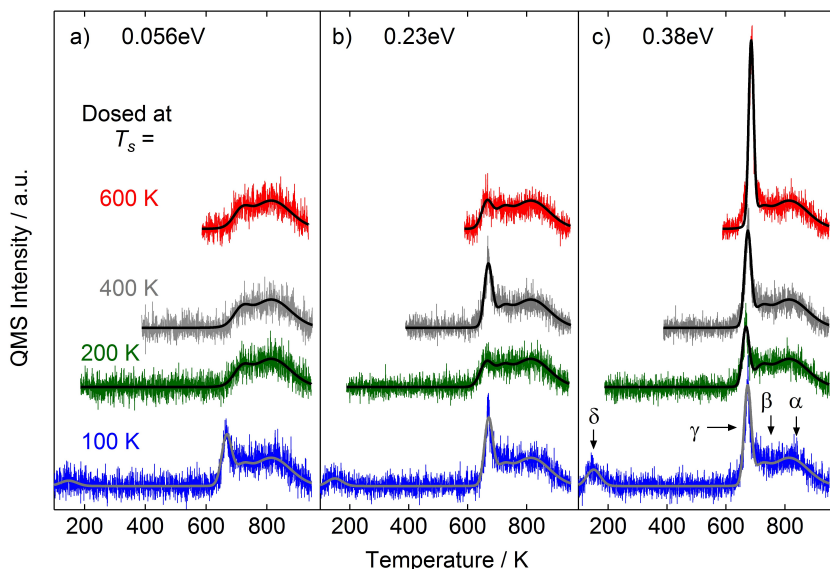


Figure 4.6: TPD spectra of mass 32 (including fits through the data), recorded after KW experiments with a) $E_i = 0.056$ eV, b) 0.23 eV, and c) 0.38 eV for various T_s . The heating rate of the crystal is 2 K/s.

our KW uptake data to have a coverage of 0.34 ML, the uptake curves closely resemble those previously measured by TPD. Therefore, we assume that the total TPD desorption (combined α and β -peak) of $E_i = 0.056$ eV and $T_s = 200$ K adds up to 0.34 ML. We have applied this scaling factor to all of our TPD spectra.

The total oxygen coverage (total integrated TPD signal for the α , β , γ , and δ -peaks) as function of E_i for various T_s is shown in figure 4.7a. Note that in case our assumption of 0.34 ML for the combined α and β -peak is not correct, the data in the figure will shift along the y-axis. It does not affect the observed trends. The traces of 200 and 300 K and of 400 and 500 K are nearly identical. At the lowest two energies, the coverage does not change. At intermediate energies, the coverage increases with increasing energy. At high energy, the maximum obtained coverage saturates. At 600 K, the maximum coverage increases initially more slowly than for the other surface temperatures. Above 0.23 eV, it accelerates resulting in a maximum coverage of almost 0.6 ML at $T_s = 600$ K and 0.38 eV. The maximum obtained coverage of the 100 K experiments is generally higher than the other surface temperatures. This additional oxygen is distributed over the γ and δ peaks.

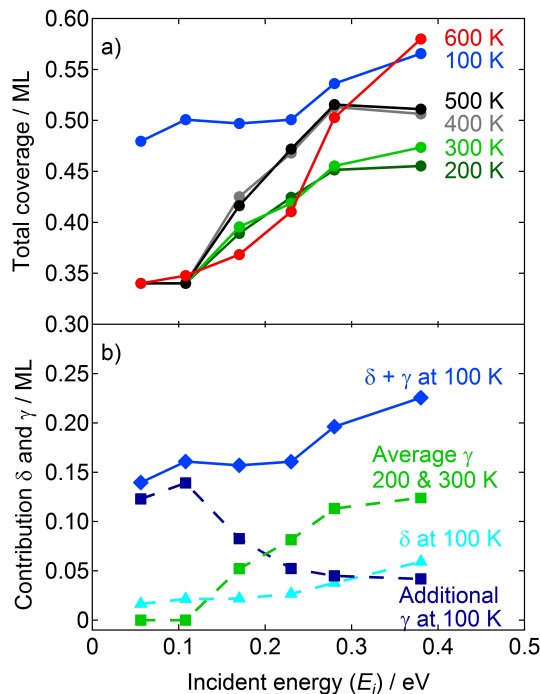


Figure 4.7: a) Integrated TPD peak areas of the total coverage (α , β , γ (and δ)) in ML for oxygen desorption from Pd(100) as function of E_i for various T_s (circles). b) The average integral of the γ -peak for $T_s = 200$ and 300 K (green squares), the δ -peak at 100 K (triangles), and the additional γ -peak at 100 K (blue squares) compared to 200 and 300 K add up to the total contribution of the γ and δ -peak for $T_s = 100$ K (diamonds).

Figure 4.7b shows a deconvolution of the amounts of desorbing O_2 in the different desorption features for the experiment performed at 100 K. The triangles show the amount of oxygen that desorbs in the δ -peak. This may safely be assumed to result from desorption of molecularly adsorbed O_2 . However, part of the molecular species present at 100 K may have dissociated during the temperature ramp instead of desorbing between 100 and 150 K. The dissociated fraction would reappear in the γ peak. We estimate this contribution in the following way. The green squares indicate the average γ -peak of the experiments performed at 200 and 300 K. We assume that it is the same for the 100 K experiment for identical incident energy. The blue squares then reflect the amount of additional oxygen in the γ -peak as compared to the green squares. Hence the blue squares reflect our esti-

mate of molecular O_2 that dissociated instead of desorbed during the temperature ramp. The three dashed traces add up to the total amount of oxygen in the δ and γ -peak (diamonds) for experiment at 100 K. The ratio 'additional γ ' to δ changes from 7.5 at low E_i to 0.7 at high E_i . This ratio reflects a vastly changing tendency for molecular O_2 adsorbed on O-covered Pd(100) surface to dissociate vs. desorb.

The total obtained oxygen coverage on Pd(100) as determined from TPD traces as function of E_i (horizontal axis) and T_s (vertical axis) is shown in figure 4.8. This coverage plot was constructed from 36 averaged measurements (for 6 different temperatures and 6 different energies). The data is interpolated to show a more smooth transition between the data points. It clearly shows the higher coverage for the 100 K surface temperature for the entire energy range (orange/red). At high E_i and high T_s , we also obtain a high surface coverage.

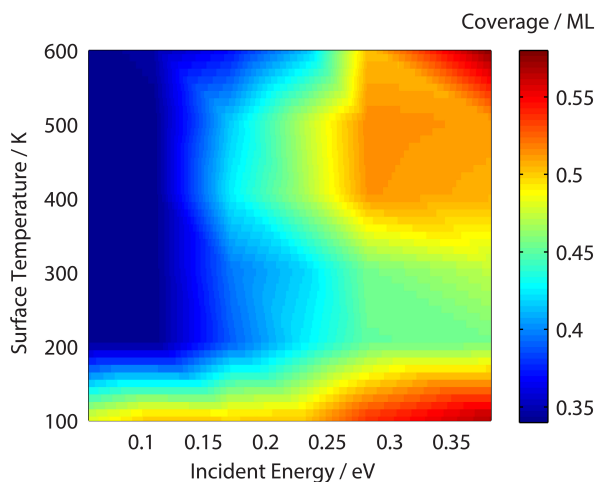


Figure 4.8: A surface plot of the total coverage in ML for oxygen desorption from Pd(100) as function of both incident energy (horizontal axis) and surface temperature (vertical axis).

Note that the total exposure used to obtain the data in figure 4.8 varies for different incident energies, but not for surface temperatures. The figure does not represent the obtained coverage per exposure, but the amount of O_2 detected during the subsequent desorption. Fluxes of the various O_2 beams vary non-linearly between the different kinetic energies by at most a factor of 1.8. As the TPD traces were taken after exposing the surface to a point where the sticking probability had dropped to (nearly) zero, exposures varying by this factor would not lead to signifi-

cant changes in the absolute coverage. Hence, the color-coding is neither skewed in either direction by experimental variations.

4.4 Discussion

4.4.1 Oxygen adsorption

The coverage-dependent sticking probability traces in figure 4.5 inform us on the adsorption dynamics of O_2 on the Pd(100) surface. The data for the lowest impact energy and lowest surface temperature show a nearly invariant sticking probability up to a point where it rapidly drops. Initially, the sticking probability actually even increases slightly, as it does for the 400 K trace. Such an independence on coverage or increase has been observed before for various systems^{46,69,70}. It is often attributed to sticking via a precursor^{54–56} state that has a long life time, suggesting that the molecule will find an adsorption site through diffusion, independent of where it originally impinged onto the surface. The precursor state may be located in the plane of the surface above an occupied site (extrinsic precursor) or above the bare surface (intrinsic precursor). However, sticking via such an equilibrated, mobile precursor seems not to be the case here.

First, a previous EELS study showed that the molecular oxygen state is not stable in the zero-coverage limit on Pd(100) at any of the temperatures in our experiments³³. Hence, at least initially, molecular O_2 impinging onto the bare surface must dissociate. Sticking into a stable molecular state may only occur after sites are blocked by O_2 molecules that dissociated earlier. Second, we have shown previously that the weak kinetic energy dependence of initial sticking suggests that a direct dissociation process is dominant. Only at low incident energy it seems supplemented by a process that is sensitive to the molecular chemisorption well⁷¹. We referred to the latter as a dynamic precursor mechanism to dissociation to distinguish it from accommodated extrinsic or intrinsic precursor states. Such a dynamic precursor state is well-known for sticking of molecular hydrogen on stepped platinum surfaces^{50,52,72,73}.

Our coverage-dependent adsorption data support this view. From our TPD results, we can conclude that a molecular O_2 state must exist on the oxygen-covered surface and that it is occupied at high coverages in adsorption experiments performed with a surface temperature initially well below 200 K. At 150 K, we still

observe a small δ -peak in TPD spectra, but at 200 K we do not. Although this molecular state must exist and can be occupied at higher coverages, the initial sticking coefficient and its rate of change in the first seconds of the adsorption experiments are identical for each set of incident energies. Exemplary data for 100 and 400 K are shown in figure 4.5. All other data for different conditions show the same behavior. The extent of the overlap of the traces varies per energy, but it lasts in each case long enough to account for a significant fraction of the total adsorbed oxygen. The absence of a surface temperature dependence in the dissociation probability in the first seconds strongly argues against sticking via any type of accommodated precursor state up to the coverage where the traces for 100 and 400 K deviate. Until the point of deviation is reached, a molecular state can therefore only be passed through transiently on the path to dissociation and can not be considered equilibrated. Beyond the point of deviation, molecular sticking into stable precursor states presents an additional mechanism at 100 K that is likely also related to the higher obtained final coverages apparent from the subsequent desorption experiments.

The insensitivity of the sticking probability on coverage for 100 K and 0.056 eV is thus not a result of dissociative sticking via equilibrated precursor states. It must result from consecutive adsorption mechanisms leading initially to dissociation and subsequently to additional molecular sticking. The necessary Langmuirian-like drop in time for sticking from the direct dissociative mechanism must be fully compensated by sticking into the molecular state. Hence, molecular sticking on partially O-covered Pd(100) is equally efficient as the initial dissociative sticking on the bare surface. This suggests that curvature of the potential leading into the molecular state is not strongly affected by occupancy of four-fold-hollow sites at or near the site of impact. The sudden drop in sticking in the trace indicates that this behavior is restricted to a certain limit and that molecular sticking reaches only a certain coverage on top of or in between the atomic states.

The difference between the 100 and 400 K traces may be interpreted as additional molecular sticking on partially O-covered Pd(100). The point at which traces for the different temperatures start deviating varies with kinetic energy. As fluxes for beams with different kinetic energies vary, the point at which deviation occurs in terms of flux or dissociated O_2 may not be directly obtained from figure 4.5. We will show elsewhere that the coverage-dependence observed for the intermediate energies can be quantitatively explained as a summation of the behaviors observed

for the lowest and highest incident energies.

As fluxes are not equal for experiments using various kinetic energies, the total integrated areas under the curves can also not be compared for the three panels in figure 4.5. Correcting for the different fluxes shows that the accumulated O-coverage in the adsorption experiments increases substantially with increasing kinetic energy. This is also reflected in figures 4.7 and 4.8, but then through the subsequent O₂ desorption. This effect is observed for any surface temperature.

Increasing maximum obtained coverages with increasing incident energies were also found for, e.g., CH₄ dissociation on Pt(111)⁷⁴. It may imply that a new dissociation barrier in the entrance channel appears with increasing coverage or that an existing barrier shifts upward and/or toward the entrance channel of the potential energy surface. Considering that the invariant sticking at 100 K and 0.056 eV suggested no significant change in the entrance channel with increasing coverage, our data suggest that a modest barrier between the molecular and atomic state, i.e. in the exit channel, increases with coverage. It may still be overcome by additional kinetic energy of the impinging molecule. Recent DFT calculations report potential energy curves for O₂ binding to various O-covered Pd(100) surfaces³⁹. Liu and Evans find that with increasing O-precoverage, the molecular state weakens while the barrier to dissociation increases. The binding energy of atomic states also decreases with coverage. This barrier is located in the exit channel. Hence, calculations and the interpretation of our experimental results are at least qualitatively in agreement.

Finally, it is noteworthy that in this picture of adsorption and dissociation for increasing coverage, the energy dependence on sticking indicates that the potential efficiently couples normal momentum of the impinging O₂ to lateral momentum of the individual nuclei, helping to surpass the rising dissociation barrier in the exit channel. This again argues against accommodation in a molecular precursor state for trajectories that end up in a dissociated state.

4.4.2 Oxygen desorption

To aid our understanding of Pd(100)'s oxygen uptake, we have divided the obtained coverage plot into various areas in figure 4.9. The arrows indicate the direction in which a higher surface coverage is obtained by independently varying incident kinetic energy or surface temperature.

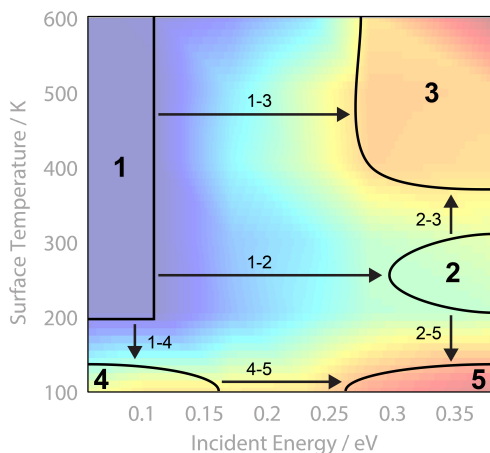


Figure 4.9: The maximum coverage of oxygen on Pd(100) is divided into five different areas that depend of incidence energy (horizontal axis) and surface temperature (vertical axis). The arrows indicate the pathways for obtaining a higher coverage.

Our starting point is area 1, where the coverage is relatively low. Above the surface temperature of 200 K, molecularly adsorbed O_2 is not stable and for the lower incident energies TPD spectra show the α and β -peaks only. The associated TPD area was scaled to a coverage of 0.34 ML as described previously. Although we can not distinguish surface structures by LEED, previous studies provide reference. The local coverages of the $p(2 \times 2)$ and $c(2 \times 2)$ structure, and the absence of the γ -peak for TPDs from area 1, require that the surface is composed of $p(2 \times 2)$ and $c(2 \times 2)$ patches with a ratio of roughly 2 : 1.

With increasing energy (areas 2 and 3), the γ -peak in TPD spectra appears whereas the subsequent α and β -peaks do not change. The sharp and narrow γ -peak has been observed before for adsorption at high surface temperatures^{36,38,68}. The formation of this γ -peak is considered an activated process and indicates the presence of the $p(5 \times 5)$ and/or $(\sqrt{5} \times \sqrt{5})R27^\circ$ structures. The appearance of the peak in TPD spectra along line 1-2 shows that formation of these high coverage structures is indeed activated. The energetic barrier may be overcome by providing gaseous O_2 with more kinetic energy. This is interesting as formation of these structures not only involves dissociation of O_2 , but also significant changes in the position of Pd atoms. This observation suggests that kinetic energy of O_2 is coupled rather efficiently to motion of other Pd and O atoms at the site of impact creating a

local high O-coverage PdO structure.

In region 2, the coverage approaches, but does not reach, 0.5 ML. As the γ -peak is present, adsorption can not solely have formed a nearly completed $c(2 \times 2)$ overlayer. Therefore, it must be a mix of three phases. The question then arises whether the high coverage phase was formed from highly energetic O_2 dissociation within the $p(2 \times 2)$ or $c(2 \times 2)$ patches, or at the boundaries between these. If only the former structure allows for additional dissociation, half of the $p(2 \times 2)$ area as obtained in area 1 needs to be converted to the $p(5 \times 5)$ structure in area 2. If only the latter structure would allow for additional dissociation, the approximately 1/3 of the surface covered by $c(2 \times 2)$ in region 1 would have to be converted entirely into $(\sqrt{5} \times \sqrt{5})R27^\circ$, i.e. the structure with a highest local coverage near 0.8 ML to account for the TPD integral. This option seems less likely. Dissociation at boundaries between phases may also occur and initiate the formation of nuclei of the higher coverage PdO structures. Obviously, the total TPD integral may also be accounted for by a mix of these processes, i.e. additional dissociation on both (2×2) phases and their boundaries.

Surface temperature may also enhance the total oxygen uptake, similar to kinetic energy. Within region 1, no increase is observed in the obtained coverage over a 400 K span, whereas from region 2 the ultimate coverage rises from 0.45 ML to nearly 0.6 ML in region 3. The rise in coverage is associated with an increase in the γ -peak of desorption only. The thermal energy and kinetic energy variations in figure 4.9 are not quantitatively comparable though. Whereas thermal energy spans several tens of meV, the change in kinetic energy equals hundreds. Hence, we can not conclude that thermal energy is less effective in creating high coverage structures. On the other hand, the limited amount of additional thermal energy has a clear effect when kinetic energy is high. The increase along line 2-3 suggests that thermal energy aids in additional formation of the high coverage structures when they are initiated by high kinetic energy impact. Note that near 600 K, the high coverage structures also start to disintegrate. Hence, a possible interpretation of the topography of obtained surface coverage above 200 K is that kinetic energy facilitates nucleation of higher coverage PdO structures and that surface diffusion contributes to their growth. The size of various patches would then be governed by the kinetics of nucleation, growth, and disintegration of the PdO high coverage structures. If this interpretation is correct, an STM study in combination with oxidation by a supersonic molecular beam would show that two different sets

of conditions leading to the same overall coverage is associated with different distributions of patch sizes. The interpretation in terms of competing kinetics may also explain the delayed increase in the obtained coverage with kinetic energy for the 600 K trace as shown in figure 4.7a.

At adsorption temperatures between 100 and 150 K (areas 4 and 5), the molecular oxygen desorption peak (δ -peak) and a γ -peak are observed in the subsequent TPD experiments. They account for the considerably higher coverages over the entire incident energy range as compared to surface temperatures ranging from 200 to 500 K. Following line 1-4 nearly 0.15 ML O adsorbs more at 100 K than at 200 K. At low kinetic energy, none of the high temperature experiments (area 1) show the γ -peak in figure 4.6. Therefore, the high coverage structure required to explain the γ peak for area 4 is not formed while the surface is at 100 K. More likely, it is formed from dissociation of O_2 chemisorbed to the low coverage $p(2 \times 2)$ and/or $c(2 \times 2)$ structures. At low impact energy, these molecules adsorb to the abundant low atomic oxygen coverage areas and show preference for dissociation over desorption during the temperature ramp. When the kinetic energy is increased (line 4-5), higher coverage structures are already formed from direct dissociation. Consequently, fewer O_2 molecules adsorb on top of this surface, and a preference for desorption over dissociation develops. These trends appear in figure 4.7b.

The appearance of the γ peak for area 4 is quite surprising though. Nucleation of high coverage structures was ascribed to dissociation of molecules impinging with high kinetic energy. Thermal energy during the temperature ramp is low and would not be expected to assist much in overcoming the activation barrier to forming the high coverage PdO structures. However, if kinetic energy and the reaction energy are both easily absorbed locally by phonon excitations, and phonons drive the formation of the high coverage structures, the apparent contradiction is resolved. In other words, heating the surface does not generate the PdO nuclei, but deposition of energy from an impinging molecule creating a local hot spot does. A higher surface temperature then still contributes to growth of the PdO structures by increasing O diffusion. Recent dynamical calculations for O_2 dissociation on the Pd(100) surface support his idea. Phonon excitation to absorb the reaction energy is fast, efficient and local⁴². In the previous section we concluded that kinetic energy also seems to couple well to the surface.

4.5 Summary

The results of our adsorption and desorption experiments for O_2 on Pd(100) support the idea that dissociation is mostly direct. At low incident energy it may be supplemented by a dynamic precursor mechanism passing through a molecular state. At low surface temperatures and significant O-coverage this molecular state may be occupied. A chemisorbed O_2 molecule on (2x2)-type overlayers may also dissociate thermally and cause an unexpectedly high local coverage of a PdO-type structure. The formation of such high coverage structures is activated and can also be caused by kinetic energy of the impinging O_2 for surface temperatures where the molecular state is unstable. We suggest that the nucleation of PdO structures from the (2x2) structures with a local coverage exceeding 0.5 ML is induced by local phonon heating. These are excited efficiently by coupling of the reaction energy and kinetic energy of the impinging molecule to motion of Pd atoms at the site of impact. While locally-induced phonons drive the transition to PdO structures, thermal phonons aid in growing the PdO nuclei through increased diffusion of O atoms. The existence of the molecular state and the kinetics of nucleation, growth and decomposition of the high coverage structures cause an unexpected topography in oxygen adsorption as a function on incident energy and surface temperature.

Chapter 5

Adsorption and dissociation of O₂ on Pt(553)

Abstract

Molecular adsorption and dissociation of O₂ on Pt(553) have been investigated using supersonic molecular beam techniques and TPD. The sticking probability was determined for various combinations of incident kinetic energy, surface temperature, incident angle, and surface coverage. A comparison with data for Pt(533) and Pt{110}(1×2) shows quantitatively the same high step-induced sticking at low energies compared to Pt(111). The enhancement is therefore insensitive to the exact arrangement of atoms forming surface corrugation. We consider energy transfer and electronic effects to explain the enhanced sticking. On the other hand, dissociation dynamics at higher incident energies are strongly dependent on step type. The Pt(553) and Pt(533) surfaces are more reactive than Pt(111), but the (100) step shows higher sticking than the (110) step. We relate this difference to a variation in the effective lowering of the barrier to dissociation from molecularly adsorbed states into atomic states. Our findings are in line with results from experimental desorption studies and theoretical studies of atomic binding energies. We discuss the influence of the step type on sticking and dissociation dynamics with a 1-D PES.

This chapter is based on: L. Jacobse, A. den Dunnen, and L.B.F. Juurlink, *J. Chem. Phys.*, 2015, **143**, 014703.

5.1 Introduction

Platinum is widely used as a catalyst for a variety of chemical processes, including oxidation reactions and the conversion of car exhaust gases. One of the most important steps in oxidation reactions is breaking the oxygen-oxygen bond in O_2 by dissociative adsorption. Therefore, a thorough understanding of the O_2 /Pt system is of crucial importance to describe the overall process of oxidation. By combining single crystal surfaces in an ultra-high vacuum (UHV) environment with supersonic molecular beam techniques, detailed information about the role of surface structure and other variables, e.g. incident kinetic energy (E_i), surface temperature (T_s), incident angle (Φ), and coverage (θ) can be obtained. Especially the flat Pt(111) surface has drawn a lot of attention in the past years^{19–21,23,24,75–81}. However, other low-Miller-index surfaces, e.g. Pt{100}(1x1)⁸² and Pt{110}(1x1)⁸³, corrugated surfaces, e.g. Pt(533)^{84–86} and other stepped surfaces^{87–92}, and reconstructed surfaces, e.g. Pt{110}(1x2)⁶⁹ and Pt(100)hex-R0.7°⁹³, have also been studied both experimentally and theoretically.

As reviewed by Vattuone *et al.*, four different adsorption states of oxygen on Pt(111) have been identified experimentally⁹⁴. A molecular physisorbed state, two molecular chemisorbed states (peroxo- and superoxo-like), and one atomically chemisorbed state have been observed using various spectroscopic techniques. Theoretical studies show three different molecular adsorption states for O_2 on Pt(111). A top-bridge-top (superoxo-like), a top-fcc-bridge (peroxo-like), and a top-hcp-bridge orientation are suggested⁷⁷. Adsorption on a top-hcp-bridge site was not observed experimentally. This is explained by the low barrier for rotation to the superoxo species. Dissociation of the molecularly chemisorbed species was only observed with the peroxo or top-hcp-bridge species as intermediate state. Depending on the surface coverage, the most stable adsorption sites for the O atoms were the fcc and hcp sites (low coverage) or just the fcc sites (all coverages). A series of molecular beam studies have investigated the dissociation dynamics of O_2 on Pt(111)^{19,21,24,92}.

Surfaces containing (111) terraces with regular steps are often used to model the influence of edges occurring on real catalytic particles. Figure 5.1 shows several of such surfaces in comparison to the (111) plane. Step ‘defects’ are expected to play an active role in O_2 dissociation dynamics on platinum. Gee and Hayden investigated O_2 adsorption on the Pt(533) surface⁸⁴. This surface consists of four-

atom wide (111) terraces separated by square (100) step edges (Pt[4(111)x(100)]). Walker *et al.* studied the reconstructed Pt{110}(1x2) surface (figure 5.1d), which contains of three-atom wide (111) terraces separated by sharp (111) type step edges⁶⁹.

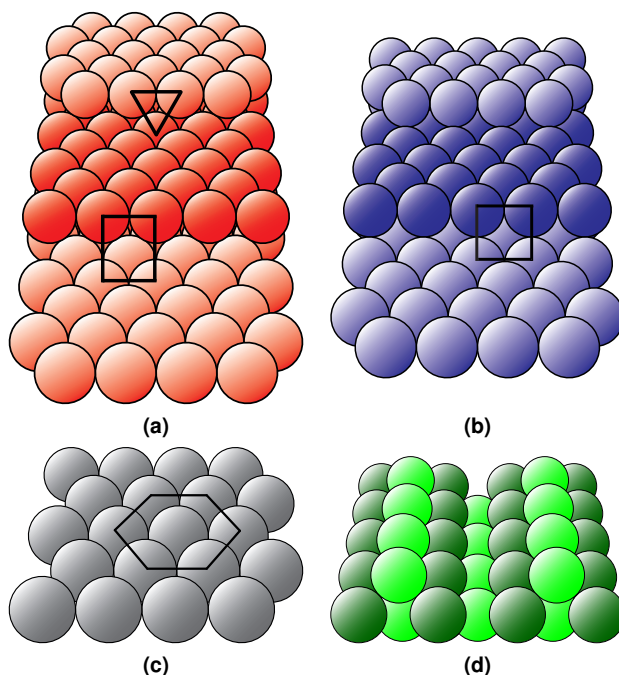


Figure 5.1: a) The Pt(553) surface structure with hexagonal terraces and rectangular (or triangular) step sites; b) The Pt(533) surface structure with hexagonal terraces and square step sites; c) The Pt(111) surface with a hexagonal structure; d) The Pt{110}(1x2) surface structure with a missing row reconstruction.

For surfaces consisting of (111) terraces, we have demonstrated that the step type is a relevant parameter in the desorption process⁹⁵. This temperature programmed desorption (TPD) study of the O₂ associative desorption from Pt(553) (figure 5.1a) and Pt(533) (figure 5.1b) showed significantly different desorption temperatures for the steps while desorption from the (111) terraces occurred at the same temperature. Desorption of the molecularly chemisorbed species occurs around the same temperature for the different step types as was shown by experiments for Pt(331)⁹⁰ and Pt(311)⁹¹. Density functional theory (DFT) calculations find similar characteristics⁸⁷.

To study the influence of step type on adsorption experimentally, one may compare results for the previously mentioned molecular beam studies for Pt(533) and Pt{110}(1 \times 2). However, as these surfaces have different terrace lengths and different step types, a better comparison is made with Pt(553) (Pt[4(111) \times (110)]). This surface has the same terrace width as Pt(533), only now with rectangular (110) step edges. Alternatively, Pt(553) can be described as a surface with five-atom wide (111) terraces and (111) type step edges (Pt[5(111) \times (111)]). Both the rectangular and triangular atomic arrangements at the step are indicated in figure 5.1a. In this regard, Pt(553) may also be compared better to Pt{110}(1 \times 2) as both contain the same arrangement of Pt atoms forming the step edge.

Here, we report on studies of the molecular dynamics of adsorption and dissociation of O_2 on Pt(553). The overlap in surface structure allows for a fair comparison of our data to those published for Pt(111)²⁰ and Pt(533)⁸⁴. As far as data are available, a comparison is also made to the data for Pt{110}(1 \times 2)⁶⁹.

5.2 Experimental

Experiments were performed using an UHV apparatus (base pressure $< 1 \cdot 10^{-10}$ mbar) equipped with, among others, a double differentially pumped supersonic molecular beam, a fixed quadrupole mass spectrometer (Pfeiffer, QMA 200), a quadrupole mass spectrometer (UTI, 100C) which can be moved along the molecular beam axis, and a LEED/Auger (RVL 2000/8/R) apparatus. The Pt(553) single crystal (cut and polished $< 0.1^\circ$, Surface Preparation Laboratory, Zaandam, The Netherlands) is suspended from a liquid nitrogen cooled cryostat on an x, y, z, θ manipulator. It was cleaned by repeated cycles of Ar^+ bombardment (Messer, 5.0; 15 μA , 5 min.), annealing at a surface temperature of 900 K in an oxygen atmosphere (Messer, 5.0; $3.5 \cdot 10^{-8}$ mbar, 3 min.), and three minutes of vacuum annealing at a surface temperature of 1200 K. The surface cleanliness was confirmed by comparison of TPD spectra with ones that have been measured previously in our group and are known to be sensitive to structure and contamination⁹⁵. Surface structure was confirmed by LEED. The spot row spacing to spot splitting ratio was found to be ~ 3.9 , which corresponds well to the literature value of 3.8406⁹⁶. In between measurements, the crystal was vacuum annealed for 3 min. at a surface temperature of 1200 K. Consistency of the quality of the Pt(553) surface during the

day was monitored by regularly repeating an experiment under identical conditions. For angle-dependence studies, the rotational axis of our crystal would ideally be along the $[\bar{1}10]$ direction. We determined it to be off by 15° . Upon rotation of the crystal, molecules do not impinge exactly orthogonally into the step edge.

The molecular beam was created by expansion of a gas at 0.5-4.3 bar through a tungsten nozzle with a circular $45\ \mu\text{m}$ diameter orifice. A beam is shaped by a set of skimmers. Flags and a chopper wheel allow us to modulate the beam. The kinetic energy of the molecular beam was controlled by seeding or antiseeding with helium (Linde, 6.0) or argon (Air Products, 5.7). The nozzle is concentrically placed in a larger diameter tube. The tube is heated by electron bombardment from two filaments, radiatively heating the nozzle and leading to higher kinetic energies of the molecular beam. By combining antiseeding and nozzle heating, resulting in a beam with intermediate E_i , we have verified that heating the nozzle has no influence on the sticking probability. To determine the (spread in) kinetic energy of the O_2 in our beam, time-of-flight (TOF) experiments were performed with the movable mass spectrometer. To obtain a sufficiently low flux of oxygen (Air Products, 5.8 or Hoekloos 3.96 vol% O_2 in He, 4.6), we mixed gases feeding the expansion with an O_2 concentration less than 8%. In addition, the beam was chopped at high frequency ($\sim 250\ \text{Hz}$) by a chopper wheel with a 16% duty cycle. The (initial) sticking probabilities were determined with the fixed mass spectrometer using the King and Wells technique (KW)⁸. Our UHV system has a vacuum time constant for O_2 on the order of 0.05 s which causes a nearly stepwise initial increase of the partial O_2 pressure within the first second in all sticking probability measurements. It is followed by various typical coverage dependencies that last for 10^1 to 10^2 of seconds. A linear fit through the first few seconds of the data was used to accurately determine the sticking probability at $t = 0$ (as in chapter 3). No significant variations in S_0 were found in a period of two years and after several modifications to the setup had been made.

5.3 Results

5.3.1 Initial sticking probability

Figure 5.2 shows the initial sticking probability of O_2 on the Pt(553) surface (circles) for $T_s = 200\ \text{K}$ as a function of the incident kinetic energy. Maxwell distributions

for O_2 are added as lines for room temperature and temperatures common in car exhausts¹ to indicate the most relevant energy range. For comparison, the data for Pt(533) (squares⁸⁴), Pt{110}(1x2) (diamonds⁶⁹), and Pt(111) (triangles²⁰) are also shown in this figure. For $E_i < 0.2$ eV, S_0 decreases with increasing incident energy. Although this trend is seen for all surfaces, the absolute values of S_0 for the Pt(553), Pt(533), and Pt{110}(1x2) surfaces are significantly higher as compared to the Pt(111) surface. Noticeably, the absolute values for these stepped surfaces coincide up to ~ 0.15 eV. Here we note that in previous experiments for H_2 dissociation on Pt(533) researchers in our group also have shown quantitative agreement between our group and the Hayden group^{50,52}. Hence, the overlap is not accidental. For $E_i > 0.2$ eV, S_0 slowly increases, until a plateau is reached. The sticking probability for Pt(553) levels off to approximately 0.33, i.e. slightly higher than the value which was found for Pt(111)^{19,20}, whereas for Pt(533) S_0 converges to a significantly higher value of 0.425⁸⁴.

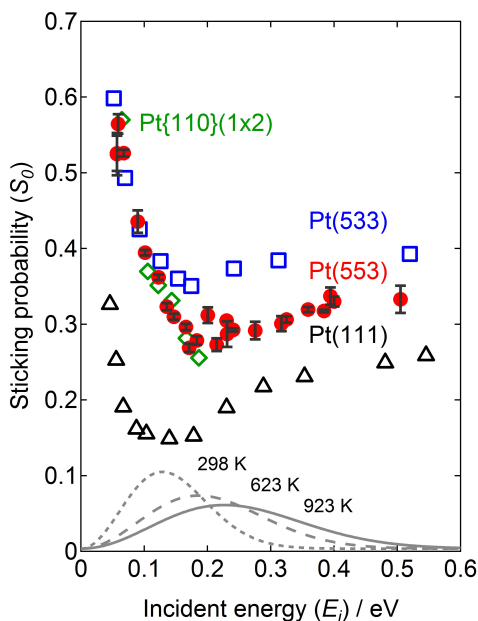


Figure 5.2: S_0 of O_2 on Pt(553) (circles, with error bars in y-direction), Pt(533) (squares⁸⁴), Pt{110}(1x2) (diamonds⁶⁹) and Pt(111) (triangles²⁰) as function of incident kinetic energy. In all experiments the incident angle is normal to the surface and $T_s = 200$ K. Maxwell distributions for 298 (dotted), 623 (dashed), and 923 K (solid) are shown with arbitrary intensity.

Figure 5.3 shows the initial sticking probability as a function of surface temperature for the Pt(553) (circles), Pt(533) (squares⁸⁴), Pt{110}(1x2) (diamonds⁶⁹), and Pt(111) (triangles²⁰) surfaces. For low incident kinetic energy (open symbols), S_0 generally decreases with increasing surface temperature. The values for $S_0(T_s)$ are again the same for Pt(553), Pt(533), and Pt{110}(1x2). They are significantly higher than for Pt(111), although the slopes (dS_0/dT_s) are rather similar. We note here that scrutinizing our data for Pt(553) shows that S_0 is actually temperature independent between 150 and 250 K within experimental uncertainty (0.56 ± 0.01). A drop with increasing temperature is only observed for $T_s > 250$ K.

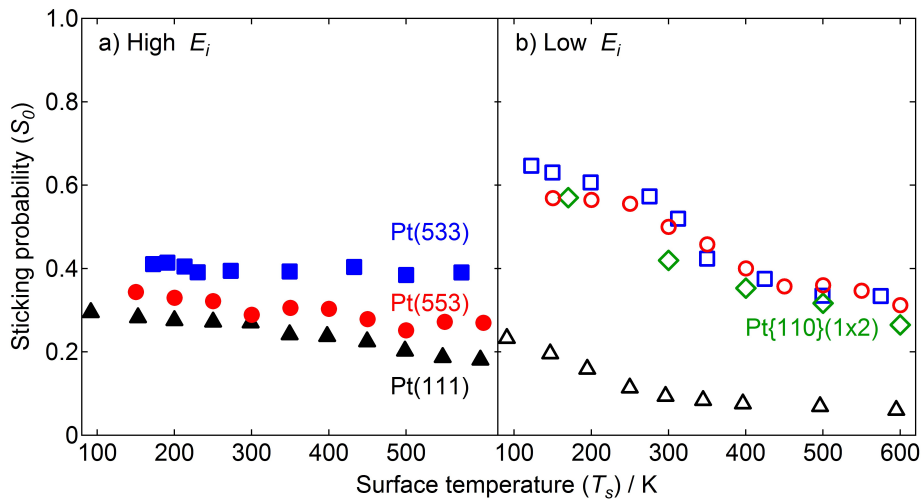


Figure 5.3: S_0 of O_2 on Pt(553) ($E_i = 0.059$ eV and 0.40 eV, circles), Pt(533) ($E_i = 0.052$ eV and 1.15 eV, squares⁸⁴), Pt{110}(1x2) ($E_i = 0.064$ eV, diamonds⁶⁹), and Pt(111) ($E_i = 0.085$ eV and 0.9 eV, triangles²⁰) as a function of T_s .

At higher incident energy (filled symbols) S_0 is less dependent on the surface temperature. It still varies clearly for Pt(553) and Pt(111) and shows nearly the same values for dS_0/dT_s . However, S_0 for Pt(533) is significantly higher and seems nearly independent of T_s in comparison to the other surfaces. We note that the E_i at which this data was collected varies significantly for the individual surfaces. However, the near energy independence for $E_i > 0.40$ eV justifies the comparison.

Figure 5.4 shows S_0 as a function of the incident angle for the Pt(553) (circles) and Pt(533) (squares⁸⁴) surfaces. The incident angle (Φ) is defined as the an-

gle between the supersonic molecular beam and the surface normal, where O_2 molecules impinge on the open side of the step for positive angles. As expected from the anisotropy of the Pt(553) and Pt(533) surface structures, S_0 shows an asymmetric behavior with a higher sticking probability for positive angles at all incident energies. For low E_i (open symbols), the Pt(553) surface shows a stronger angular dependence for S_0 than the Pt(533) surface. This effect is not due to the lower surface temperature used in our experiments as the same trend was observed for $T_s = 225$ K (not shown here). For higher values of E_i (filled) there are more striking differences between the Pt(553) and Pt(533) surfaces. Gee and Hayden deconvoluted the total signal for Pt(533) to separate the contributions from the terraces ($\Phi_{\perp} \approx -14^\circ$) and steps ($\Phi_{\perp} \approx 40^\circ$)⁸⁴. For positive angles, the data for Pt(553) yield no suggestion how to separate contributions from the step edges and terraces. It shows a smooth, nearly angle independent trend, with a dip at $\Phi = 40^\circ$. This dip is a real feature of the data set and was observed consistently for multiple values of E_i .

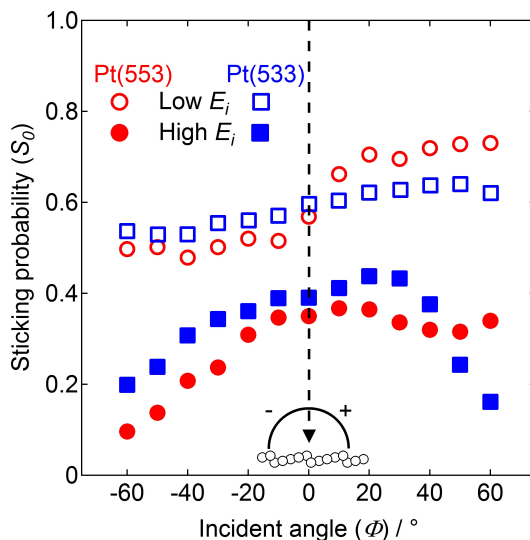


Figure 5.4: S_0 of O_2 on Pt(553) ($E_i = 0.059$ eV, open and 0.40 eV, closed circles at $T_s = 150$ K) and Pt(533) ($E_i = 0.052$ eV, open at $T_s = 225$ K and $E_i = 1.15$ eV, closed squares at $T_s = 350$ K⁸⁴) as a function of the incident angle Φ .

5.3.2 Coverage dependent sticking probability

The data in figure 5.5 show the change of the sticking probability during the experiment for $E_i = 0.059, 0.23, 0.32$, and 0.40 eV (5.5a-d respectively) and for $T_s = 150, 200$, and 250 K. As the absolute maximum oxygen coverage for Pt(553) is not known and may depend on the incident kinetic energy and surface temperature, we have not converted the horizontal axis to a coverage in monolayers here. However, the data still reveal crucial information on the dynamics of oxygen sticking on Pt(553).

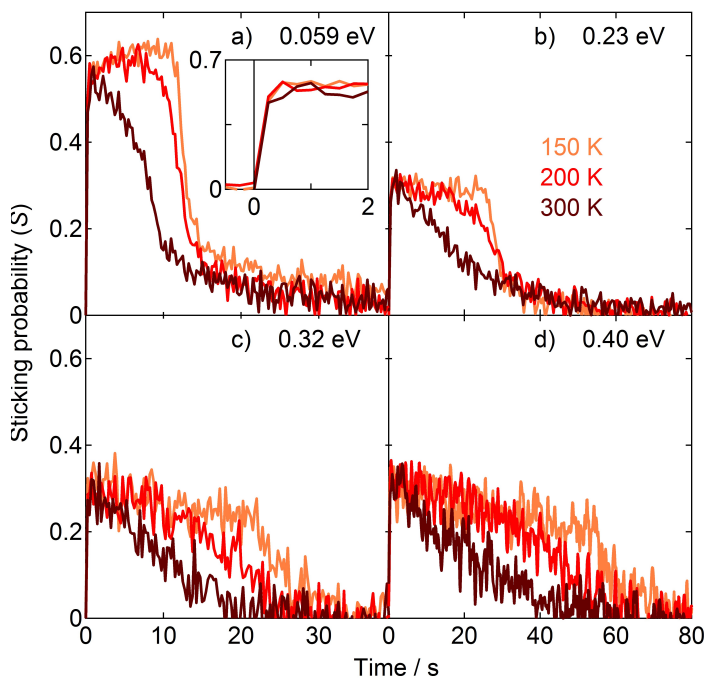


Figure 5.5: Change of the sticking probability of oxygen on Pt(553) during the experiment for $T_s = 150$ K (light), $T_s = 200$ K (red), and $T_s = 250$ K (dark) at $\Phi = 0$ and a) $E_i = 0.059$ eV; b) $E_i = 0.23$ eV; c) $E_i = 0.32$ eV; d) $E_i = 0.40$ eV. The O_2 flux was not the same for the different beams. For a-c) the time axis is 0-40 seconds, for d) it is 0-80 seconds.

First we observe that at $t = 0$ the sticking probability steps up within a fraction of a second. This is a consequence of the convolution of the measurement with the vacuum time constant for O_2 . Second, we note that S_0 (the intercept with the y-axis)

is quantitatively the same for $T_s = 150, 200$, and 250 K for all incident energies. Only beyond 250 K, S_0 drops with increasing T_s (see figure 5.3). Third, as plotted in the four panels, $dS/d\theta$ in the limit of $\theta = 0$ seems the same for $T_s = 150$ and 200 K for all incident energies. It varies from being clearly positive to slightly negative. For $T_s = 250$ K, $dS/d\theta$ seems lower than the values at lower surface temperature and always negative. However, the inset shows that this difference between $T_s = 250$ K and the other traces is not present in the first two seconds of the experiment. We only show one inset, but the same overlapping traces occur in the first seconds of all panels, and the slope $dS/d\theta$ in the zero-coverage limit is exactly the same within each panel. The differences in coverage dependence only develop after the coverage has increased well beyond 0. Furthermore, we note that for the lowest surface temperatures, the sticking probability shows an abrupt change in slope after a certain number of O_2 molecules has impinged onto the surface. The abruptness decreases with increasing surface temperature. Finally, after the abrupt decrease, at low E_i it takes significantly longer to reach $S = 0$. This is most clearly seen in the slow decrease of the traces in figure 5.5a for longer times.

Figure 5.6 shows as a 3-D plot of $S(\theta, \Phi)$ for $E_i = 0.059$ eV and $T_s = 150$ K. This sticking surface was constructed from 13 individual coverage-dependent sticking measurements. We slightly smoothed the surface to reduce noise. The coverage is an arbitrary value calculated by integrating the multiplication of time and flux (as determined in a relative sense by the QMS current for $m/e = 32$ while the molecular beam enters the chamber and impinges onto an inert flag) with the sticking probability. It is also corrected by a factor $\cos(\Phi)$ for the larger surface area onto which the beam deposits oxygen for increasing angles. This yields a total obtained (maximum) coverage in these experiments that is independent of incident angle. The initial step-like increase in sticking at all angles is again a result of the convolution of our measurement with the vacuum time constant of O_2 . This step-like increase is immediately followed by two different behaviors. For positive incident angles, where O_2 impinges into the step, the sticking probability is independent of coverage until some saturation level is reached and sticking plummets. For negative angles, where the downward step becomes increasingly invisible to the impinging molecule, the initial sticking probability is lower. However, sticking clearly increases with coverage. This behavior is maintained for a while after which the sticking probability also drops similar to the behavior at positive incident angles.

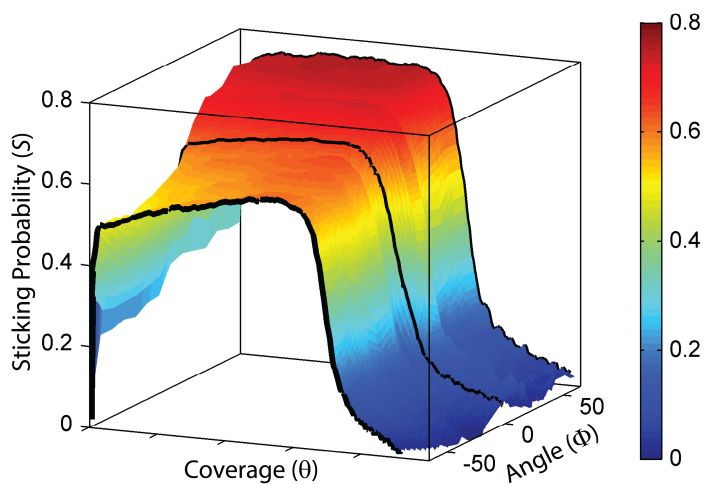


Figure 5.6: Sticking probability of O_2 on Pt(553) as function of θ and Φ for $E_i = 0.059$ eV and $T_s = 150$ K.

5.3.3 Thermal desorption

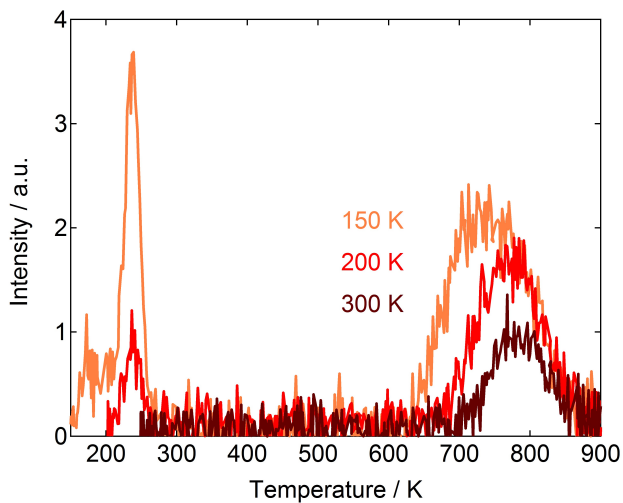


Figure 5.7: TPD spectra of O_2 desorption from Pt(553) recorded after KW experiments for $T_s = 150$ K (light), $T_s = 200$ K (red), and $T_s = 250$ K (dark) with a heating rate of 4.0 K/s.

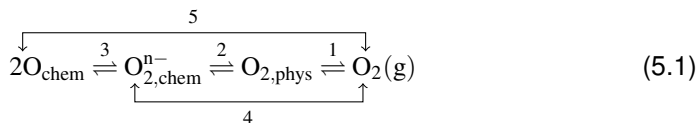
Figure 5.7 shows temperature programmed desorption spectra obtained after a molecular beam impinged onto the Pt(553) surface until we observed no more sticking. The three traces were obtained for $E_i = 0.059$ eV at normal incidence and for $T_s = 150, 200$, and 250 K. The spectra show two desorption peaks between $T_s = 150$ K and $T_s = 250$ K as well as the previously studied associative desorption features for this surface at much higher temperatures⁹⁵. Previous studies for O_2 desorption from Pt(111) that used an effusive source only show a single desorption feature near 150 K from a molecular state⁹⁷. On that surface desorption occurs in parallel with dissociation. For Pt(111), vacuum oxidation by O_2 leads to a maximum coverage of 0.25 ML O/Pt, unless it is performed at considerably higher temperatures⁹⁸. Stepped Pt surfaces yield additional desorption peaks ascribed to molecular adsorption at or near steps^{85,86,90,91}. The peak between 220 and 250 K is therefore likely due to step-bound O_2 . In our experiments, the peaks from molecular states disappear with increasing surface temperature. Wang *et al.*⁸⁵ and Rar and Matsushima⁸⁶ found similar large molecular desorption peaks for Pt(533), while Gee and Hayden only reported a considerably smaller peak⁸⁴.

TPD studies following upon adsorption from a supersonic molecular beam may not relate quantitatively to the adsorption from the beam. The total adsorption as calculated by integrating the multiplication of time and flux with the sticking probability may contain a contribution of adsorption into meta-stable sites that desorb in between stopping the beam and starting the temperature ramp. The isothermal desorption from weakly-bound states 'while not measuring' causes a quantitative discrepancy that renders us unable to relate our KW and TPD data quantitatively. On the other hand, part of molecularly-bound O_2 created at low T_s , may also dissociate during the consecutive temperature ramp. It reappears in the associative desorption regime of the TPD spectrum. The increase in the O_2 associative desorption between 600 and 900 K for experiments performed at 200 and 150 K relative to 250 K is most likely a result from this process.

5.4 Discussion

5.4.1 Initial sticking probability

Based on the previous studies using Pt(111), O_2 adsorption is generally described by:



where $\text{O}_{2,\text{chem}}^{\text{n-}}$ describes molecular states, such as the peroxo- and superoxo-like states¹⁹. These may act as precursors to dissociation while desorption from these states is also possible. The maximum coverage of molecular O_2 exceeds the atomic coverage of O on Pt(111)^{97,99}. Part of the $\text{O}_{2,\text{chem}}^{\text{n-}}$ adsorbed at low temperatures desorbs around 150 K while another part dissociates creating a (2x2) O_{chem} overlayer. The additional low temperature desorption feature between 220-250 K observed in our TPD spectra for Pt(553) (figure 5.7) and Pt(533)⁸⁴⁻⁸⁶ suggests that additional molecular states exist at step edges, likely of similar nature but more strongly bound than to (111) terraces. These molecular states may be similar but are not likely identical to molecular states appearing in potential energy surfaces (PES) for O_2/Pt or in sticking probability measurements in the zero-coverage limit. They are likely affected by interaction with co-adsorbed $\text{O}_{2,\text{chem}}^{\text{n-}}$ or O_{chem} .

Sticking probability measurements, as performed in this study, do not distinguish between final states. The initial sticking probability is simply a summation of all possible parallel and consecutive adsorption pathways occurring on a time scale faster than the measurement:

$$\begin{aligned}
 S_0 = & S_0^{\text{direct}}(\text{O}_{2,\text{phys}}) + S_0^{\text{indirect}}(\text{O}_{2,\text{chem}}^{\text{n-}}) \\
 & + S_0^{\text{indirect}}(\text{O}_{\text{chem}}) + S_0^{\text{direct}}(\text{O}_{2,\text{chem}}^{\text{n-}}) + S_0^{\text{direct}}(\text{O}_{\text{chem}})
 \end{aligned} \quad (5.2)$$

Here, individual contributions are ordered as numbered in reaction 5.1. Equation 5.2 also holds for non-initial conditions, although adsorption energies of atomic and molecular states may alter with coverage.

The physisorbed state is not stable at any experimental surface temperature in this study and its sole contribution to S_0 from reversible reaction 1.1 is zero⁹⁴. However, the physisorbed state may be passed through for indirect molecular chemisorption, i.e. reaction 1.2. As adsorption on Pt(111) at low energies shows a negative dependence on incident energy, an indirect sticking mechanism into a chemisorbed state occurring via the physisorbed state is generally invoked^{19,20,24}. The subsequent increase of S_0 with E_i is often argued to represent an additional activated

pathway to adsorption. For Pt(111), this is reaction 1.4, i.e. direct sticking into a molecular state. For surface temperatures exceeding ~ 200 K, this chemisorbed and equilibrated O_2 either dissociates along an activated path, i.e. reaction 1.3, or desorbs back into the gas phase. This competition explains the T_s dependence at high E_i for Pt(111).

While this picture of O_2 adsorption was constructed in the previous century and mostly based on experimental studies, theoretical studies are still debating whether the physisorbed state on Pt(111) is a crucial ingredient to explain the kinetic energy dependencies. A recent molecular dynamics simulation, based on a classical reactive force field approach, includes a physisorption well of ~ 0.04 eV, a molecular chemisorption well of 0.35 eV and a very high barrier to dissociation from the latter well in a top-bridge-top geometry⁸¹. The study finds that sticking in the low energy regime proceeds via steering and trapping in the physisorption well. It reproduces the energy-dependence on sticking, including the dip in reactivity near 0.2 eV, and results from an older O_2 scattering study¹⁰⁰ reasonably accurately. On the other hand, a previous tight-binding molecular dynamics study reproduced kinetic energy and surface temperature trends without such a physisorption well²³. E_i -dependent steering and energy transfer from the surface to the molecule at finite surface temperatures were indicated as the origins for the experimentally observed trends.

The similar energy and surface temperature dependencies for sticking on Pt(533) were, by comparison to the previous experimental studies for Pt(111), interpreted to suggest, at least in part, the same two sticking mechanisms; indirect adsorption via the physisorbed state and activated direct adsorption into molecular states. The significantly higher values for S_0 at low incident energy for Pt(533) were ascribed to additional direct chemisorption at the step and increased conversion of a physisorbed state to the chemisorbed state by the step. An increased reactivity at high incident energy was ascribed to an additional channel, i.e. direct, activated dissociative adsorption at the (100) step (reaction 1.5). The clear peak at the [100] normal in the angular dependence for high incident energy (see figure 5.4), was considered a fingerprint of this channel.

With this in mind, we turn to our results for O_2 sticking on Pt(553) and the comparison of data to those obtained for other Pt surfaces. We focus on the low E_i regime first.

5.4.2 Sticking at low E_i

From figure 5.2, we note that the same characteristic features appear in the initial adsorption of O_2 on Pt(553), Pt(533), Pt{110}(1x2), and Pt(111). For $E_i < 0.2$ eV the initial sticking probability strongly decreases with increasing incident energy. Also, a general decreasing trend with surface temperature is observed in this energy range (figure 5.3), although S_0 for Pt(553) is actually independent of surface temperature between 150 and 250 K. Thereafter it drops steadily as it does for all other Pt surfaces. Furthermore, the absolute values of $S_0(E_i < 0.15$ eV, $T_s)$ are equal for Pt(553), Pt(533), and Pt{110}(1x2), and significantly higher than for Pt(111). For the stepped surfaces, $S_0(\Phi)$ shows a smooth dependence, favoring an approach into the step (figure 5.4).

The similarities, especially for Pt(553) and Pt(533), may easily persuade us to adopt an explanation based on previously suggested direct and indirect mechanisms for sticking. Gee and Hayden introduced the idea of parallel sticking mechanisms to explain high sticking at low incident energy data for Pt(533) as compared to Pt(111)⁸⁴. They reasoned that a physisorbed precursor state would be more efficiently turned into a chemisorbed state on Pt(533) because of the high step density. Using a hard cube model for data at $E_i \simeq 0.05$ eV, they found this mechanism to be responsible for 0.3 of the total initial sticking of ~ 0.6 . Direct adsorption into a molecular chemisorbed state at the (100) step edge of Pt(533) was considered to contribute the other half. This direct molecular adsorption was indicated to be the same mechanism as one of the two parallel mechanisms accounting for sticking at high incident energy, i.e. direct molecular sticking (reaction 1.4). Oddly, this mechanism was considered to be activated in order to account for the increase in reactivity with increasing energy. This seems in contradiction to a mechanism contributing half of $S_0 \simeq 0.6$ at an incident energy of only 0.05 eV.

We believe that the behavior of the stepped surfaces at low energy is indeed a result of parallel sticking mechanisms. However, we expect that direct molecular sticking at the step edge in a non-activated process. At the upper edge of the step, the molecular chemisorbed state is calculated to be bound on the order of 0.5-1.0 eV more strongly than at terrace sites⁸⁷. By the principle from Bell¹⁰¹, Brønsted¹⁰², Evans, and Polanyi¹⁰³ (BEP principle), this doubling of the well depth should drag any barrier to molecular chemisorption down. We expect this to be at least several tenths of an eV. As the impinging molecule at low kinetic energies will mostly follow

the minimum energy path and steering seems efficient^{23,81}, we see no reason why direct molecular adsorption should be activated at the step. In parallel, sticking will also occur on (111) terrace sites, very similar to sticking on the ‘infinite’ (111) plane, irrespective whether it proceeds via a physisorbed state or via direct steering into a chemisorbed molecular state. Finally, the cusp of the step may very well be some intermediate zone where adsorption is not non-activated, but still different from adsorption on terrace sites.

For H_2 , experiment and theory suggest that the unit cell of a stepped surface may simply be divided into various regions, where the local potential dictates which adsorption mechanism is dominant^{50,52,72,73}. This leads to a weighted average sticking probability that quantitatively represents the various ways available for an impinging molecule to stick to a non-uniform surface. Using a series of (100) stepped Pt surfaces, researchers in our group have shown that a simple model based on the results from a three-atom wide terrace, quantitatively predicted the measured sticking probability for all other stepped surfaces and Pt(111)⁵². The model was not very sensitive to the exact assumed partitioning between step and terrace areas. Based on that approach, we may expect that the Pt(553) surface is reasonably well described as consisting for $\sim 50\%$ of an area dominated by the step (upper area and lower area) and for $\sim 50\%$ as acting like the Pt(111) surface for O_2 sticking. Hence, the total S_0 can be rewritten as

$$S_0^{553} \simeq 0.5 \cdot S_0^{step} + 0.5 \cdot S_0^{terrace} \quad (5.3)$$

The step and terrace contributions may result from various mechanisms that (for reasons of simplicity) we here refer to as direct and ‘indirect’.

$$S_0^{step} = S_{0,direct}^{step} + S_{0,indirect}^{step} \quad (5.4a)$$

$$S_0^{terrace} = S_{0,direct}^{terrace} + S_{0,indirect}^{terrace} \quad (5.4b)$$

Figure 5.8 shows the results of our model that ascribes the measured sticking probability for Pt(553) to represent a weighted average of two contributing areas of roughly equal size as schematically indicated in the inset. We have applied a polynomial fit to published Pt(111) data (solid black line). From this fit and a

polynomial fit through our measured data for Pt(553) (red data with a solid red line), we calculate the local energy-dependent sticking at the (110) step (solid blue line). We then take these two local energy-dependent sticking probabilities for step and terrace, multiply them by 0.5, and separate their contributions to the measured data further into different sticking mechanisms.

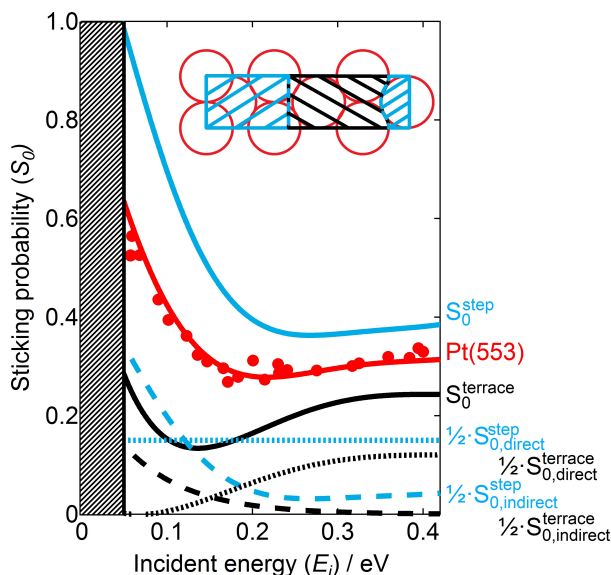


Figure 5.8: Deconvolution of the initial sticking probability into contributions from the (110) step edges and the (111) terraces.

For the contribution of the step, we argued that non-activated direct adsorption takes place. We estimate this partition directly from the difference between the reactivity observed for Pt(111) and Pt(553) (see discussion below) and expect it to be roughly energy-independent. This contribution (dotted blue line) leaves an energy-dependent remainder (dashed blue line) that must be ascribed to another sticking mechanism for O_2 molecules impinging at the bottom of the step edge. In equation 5.4 and in figure 5.8 we refer to this contribution as ‘indirect’. The contribution from the (111) terrace is also separated into two components as suggested previously^{19,21,24}. We have used an exponential decay to fit the low E_i data. It represents the indirect component that others quantify using a hard cube model^{24,84}.

In comparing the individual contributions, we find that direct processes have

roughly the same maximum value for step and terrace. Whereas direct adsorption into a molecular state is non-activated at the step, it is activated for molecules impinging on the terrace. For molecules sticking with a negative energy dependence, the ones impinging at the bottom of the step have roughly twice the chance of sticking compared to those impinging onto the terrace. Overall, this rough model is not very different from those proposed previously^{19,24,84}. However, we now consider three contributions to sticking at low incident energy on the stepped surface. The two 'indirect' mechanisms are replaced by a fourth mechanism with increasing energy.

We consider the qualitative consequences of this model for other observed dependencies at low incident energy. The negative surface temperature dependence beyond 250 K may be explained by the large contribution of two 'indirect' mechanisms. Whether these are truly indirect and proceed via a physisorbed state can not be concluded from our sticking probability measurements in the zero-coverage regime. The coverage dependencies at low incident energy and low surface temperatures show the expected features of a long-lived precursor state. Sticking even increases with coverage for the lowest surface temperatures. However, the difference in perception that is exemplified by the inset in figure 5.5, remind us that mechanisms contributing at larger coverages may not be the same as those operating on the clean surface. The inset shows that the mechanisms contribution to sticking at zero coverage are surface temperature independent up to 250 K. It is only at higher coverage that a surface temperature dependence appears. This may be interpreted to show that sticking occurs directly into chemisorbed states as S_0 only drops at surface temperatures when all these states have become unstable.

The angle dependence in figure 5.4 argues for the separation of sticking through 'indirect' mechanisms at terrace and step sites in our model. As the top of the step, where chemisorption may occur into a deep molecular well, protrudes from the (553) plane, one would not expect a significant or strongly asymmetric dependence on incident angle for this direct mechanism. Indirect sticking at the (111) terrace should show a symmetric dependence around the [111] normal at -12.3° . Hence, the asymmetry and increase at positive angles imply that molecules impinging into the lower part of the step have a different interaction with the surface than those impinging on (111) sites.

The combined angle and coverage-dependencies in figure 5.6 are in this regard also intriguing. We interpret the difference in behavior for negative and positive

incident angles as a signature that step-bound molecular O_2 provides additional corrugation with the ideal mass match for subsequently impacting O_2 molecules. In other words, step-bound O_2 molecules may aid indirect sticking by acting as efficient collision partners. This effect would increase with increasing negative impact angles. For positive impact angles, they will have less influence as the step itself already provides corrugation and efficient means for slow impacting molecules to lose their kinetic energy and momentum.

Finally, we consider whether our model explains both the similarities and minor differences between the stepped surfaces. We believe the origin for the overlap in S_0 for Pt(533), Pt(553), and Pt{110}(2x1) points to a dominant contribution of the step to the total sticking in the low energy regime. The length of the unit cell, hence the step density, is the same to within 10% for these surfaces. This implies that the number of impact sites leading to enhanced ‘indirect’ sticking through impact at the bottom of the step edges, e.g. by enhanced kinetic-to-rotational energy transfer^{72,104}, is approximately the same for all stepped surfaces considered here. Also the number of top edge sites where O_2 molecules experience a higher binding energy and where direct non-activated adsorption may occur, is nearly the same for these surfaces. Here, it is noteworthy that not only the step density but also the macroscopic work function is (nearly) the same for these three stepped surfaces^{105,106}. The only difference in dependencies that we find at lower energy is the slightly higher sticking for Pt(553) for positive impact angles. We expect that details of the PES, governing the extent of momentum and energy transfer, manifest themselves here.

5.4.3 Sticking at high E_i

Our proposed model for the observed kinetic energy dependence suggests that with increasing incident energy the ‘indirect’ mechanisms are replaced by activated, direct sticking at the (111) terrace. At the highest incident energies, roughly half of the molecules stick if their trajectory directs them into a chemisorbed state at the top edge of the step. The other half sticks as a consequence of having enough kinetic energy to overcome an (apparent) activation barrier when impinging onto a (111) terrace site. The contribution of the direct, non-activated mechanism was estimated from the maximum difference occurring between Pt(111) and Pt(553) in the regime where the ‘indirect’ mechanisms start to fail. This is ~ 0.15 at 0.2 eV.

Considering the physical size of the top of the edge in proportion to the unit cell of Pt(553), this value also represents a reasonable fraction of trajectories impinging onto this site. Furthermore, the estimate does not lead to an unphysical value, i.e. $S_0^{step} > 1$. Here, we note that the behavior below ~ 0.05 eV is simply unknown and, with standard supersonic molecular beam methods, impossible to determine. Finally, we do not consider the estimate of 0.15 very accurate, although it can also not be very different within our model. A very similar value was found for direct non-activated H_2 dissociation onto the top of Pt step edges^{52,73}.

In comparison to Pt(111) and Pt(533), sticking on Pt(553) is intermediate at the highest kinetic energies. Also, in contradiction to the behavior at low kinetic energy, the angle dependence for the two stepped surfaces is not very similar. For Pt(533), a clear ‘bump’ is observed near the [100] normal on top of a smooth trend. The angle dependence and weak T_s dependence were interpreted to indicate that the (100) steps on Pt(533) facilitate direct activated dissociation at high E_i ⁸⁴. The data for Pt(553) seems rather insensitive to the impinging angle for positive angles. We only observe a small but reproducible dip appearing at $\sim 40^\circ$. Also the temperature dependence in figure 5.3 at high incident energies varies between the stepped surfaces. Pt(533) is significantly less dependent than Pt(553). The latter actually resembles the behavior of Pt(111) more closely. Both observations justify that our model does not include direct dissociative adsorption at high kinetic energies.

The difference between the two step types is also echoed by our previously published TPD data for these surfaces. Associative desorption from Pt(533) occurs at higher temperatures than for Pt(553). This indicates a more strongly bound atomic state on the (100) step⁹⁵. This represents itself also in a weaker tendency for atomic oxygen bound at the (100) step edge to become hydrogenated to hydroxyl as compared to O_{chem} bound to (110) steps and the (111) terrace^{95,107,108}. A more strongly bound atomic state would, by the BEP principle, reduce the barrier between molecularly chemisorbed O_2 and O_{chem} . Apparently, the barrier reduction for the (100) step is large enough to allow for direct dissociation. The only minor indication that it may also occur on Pt(553) at higher E_i is the slight upturn in $S_{0,indirect}^{step}$. This may be wrongly ascribed and actually reflect a very small contribution of direct dissociation at high E_i . Obviously, spectroscopic identification of the products would be conclusive. Unfortunately, we are not currently capable of producing such data.

Previous groups have used a simple kinetic model to extract the trapping probability (α_{mc}), relative reaction barriers ($E_d - E_a$, with subscripts d and a indicating

desorption and dissociation respectively) and frequency factors (v_a/v_d) from the experimental data at high incident energies, by assuming three different adsorption states (O_{chem} , $O_{2,\text{chem}}^{n-}$, and $O_{2,\text{phys}}$) and two distinct reaction pathways (reaction 5.1.2 and 5.1.4). This has been done for Pt(111), Pt(533), and Pt{110}(1x2)^{19,20,24,69,84}. For reason of completeness, we have applied this model to our data. Assuming a trapping probability of 0.32, we find similar values ($E_d - E_a = 0.054$ eV, and $v_a/v_d = 1.18$) as for the other surfaces. However, we question how reliable this model is. Increased well depths of atomic and molecular states at the stepped surfaces combined with lower barriers to dissociation reduce the lifetime of precursor states. This competes with equilibration, which is at the heart of the kinetic model. Recent high dimensionality dynamical calculations for Pd(100) that explicitly include phonon excitation⁴², and where the molecular chemisorption energy is very similar to the value calculated for Pt steps⁸⁷, show no signs of equilibration. Furthermore, as input for this model α_{mc} is assumed from high E_i and low T_s data. Keeping this in mind, we believe that the numbers resulting from this model should not be used as anything more than rough estimates if appropriate at all.

5.5 Conclusions

Combining the observations from the experiments for Pt(553), Pt(111), and Pt(533), we suggest the three qualitative 1-D PESs shown in figure 5.9a. For clarity, we do not extend atomic and molecular chemisorption potential curves along the x-axis to high values. The inset shows the expected relative dissociation barriers. Figure 5.9b shows the locations and orientations of $O_{2,\text{chem}}^{n-}$ and O_{chem} . For molecular O_2 , both TPD experiments (for Pt(331)⁹⁰ and Pt(311)⁹¹) and DFT calculations⁸⁷ (Pt(221) and Pt(211)) find that $O_{2,\text{chem}}^{n-}$ is orientated parallel to the step edge.

We highlight the crucial similarities and differences between the three potentials. First, the weakly bound physisorption state (0.08 eV per O_2 ⁸¹) is probably not notably different for the three surfaces. However, the two different step types bind $O_{2,\text{chem}}^{n-}$ significantly stronger than the (111) terrace (top-fcc-bridge, 0.6 eV). The binding energy for the two step edges is similar (~ 1.5 eV). The atomic states differ between all surfaces. Both step types bind O_{chem} more strongly than Pt(111). The associative desorption temperature of $O_{\text{chem,step}}$ for Pt(533) is 36 K higher than for Pt(553)⁹⁵. This suggests that the $O_{\text{chem,step}}$ potential well is deepest for the (100)

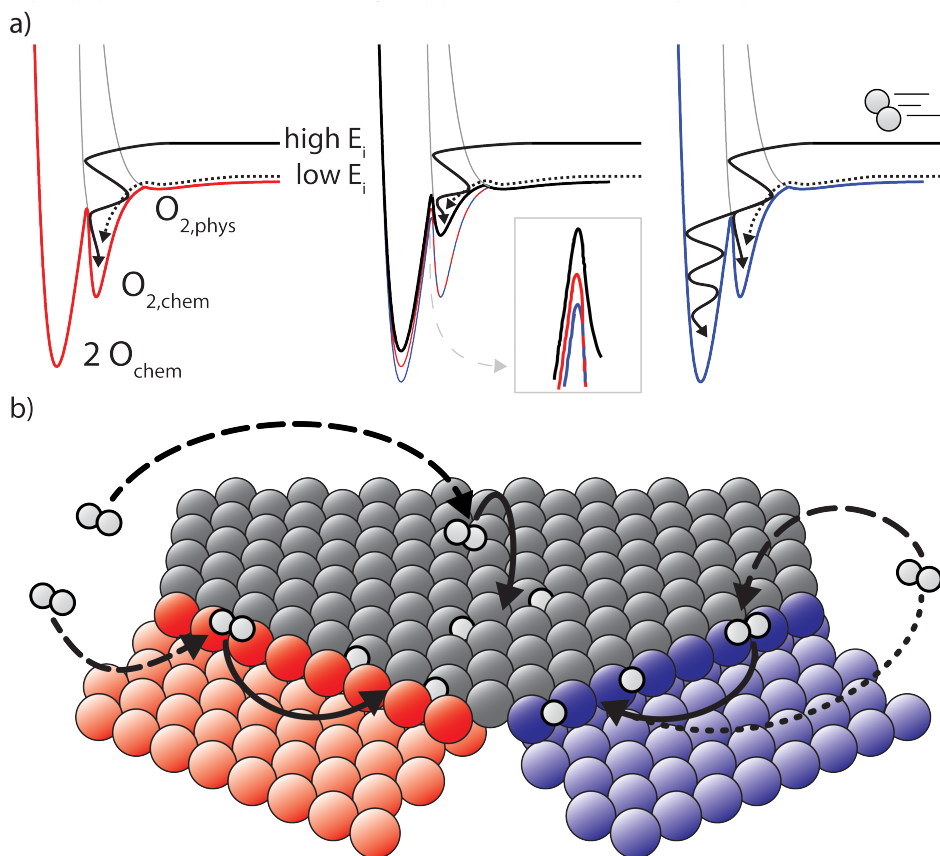


Figure 5.9: a) Qualitative 1-D PES for O_2 adsorption on the Pt(553) (red), Pt(111) (black), and Pt(533) (blue) surfaces; b) Model surface indicating the experimentally observed adsorption pathways and geometries for the different surface structures.

step. These observations are supported by DFT calculations which report binding energies of 2.2, 2.4, and 2.6 eV for $2 O_{chem}$ on Pt(111) (fcc hollow), Pt(221) (step fcc hollow), and Pt(211) (step bridge) respectively⁸⁷. The BEP principle requires that the barrier for dissociation from the molecular state is reduced more on the (100) step type than on the (110) step type. This qualitatively explains why direct dissociative adsorption (reaction 5.1.5) is only observed for Pt(533). The reaction paths drawn in figure 5.9a visualize that for the Pt(111) and Pt(553) surfaces at low and high E_i O_2 dissociates only via $O_{2,chem}^{n-}$, whereas on Pt(533) a channel to direct dissociative adsorption has opened.

Summarizing, we have shown that using a simple model it is possible to qualitatively explain the features of our data for adsorption of O_2 on Pt(553). The total sticking probability has been described in terms of contributions from four different reaction pathways. Two of these pathways are decreasing with increasing E_i , the third is activated, and the fourth is independent of E_i . This description is consistent with adsorption and desorption data from experiments and theory and may likely be applicable to similar systems.

Chapter 6

Long-range influence of steps on water adsorption on clean and D-covered Pt surfaces

Abstract

We have examined H₂O desorption from Pt(111) terraces of varying width and its dependence on precoverage by D with TPD studies. We observe distinct water desorption from (100) steps and (111) terraces. The steps provide adsorption sites with a higher binding energy than terraces. Pre-adsorption of D at steps causes annihilation of water stabilization at the steps and an initial stabilization of water on the (111) terraces. When the (111) terraces also become precovered with D, this water stabilization trend reverses on all surfaces. Destabilization continues for stepped surfaces containing up to 8-atom wide (111) terraces with a (100) step type and these become hydrophobic, in contrast to surfaces with a (110) step type and with the infinite (111) terrace. Our results illustrate how surface defects and a delicate balance between intermolecular forces and the adsorption energy govern hydrophobic vs. hydrophilic behavior. The influence of steps on the adsorption of water on nano-structured platinum surfaces has a very long-ranged character.

This chapter is based on: A. den Dunnen, M.J.T.C. van der Niet, C. Badan, M.T.M. Koper, and L.B.F. Juurlink, *Phys. Chem. Chem. Phys.*, 2015, **17**, 8530.

6.1 Introduction

The structure of H_2O at interfaces and the associated hydrophilicity and hydrophobicity are important in fields such as biology, astrophysics, chemistry, and physics^{109–121}. In biology, one could think of the folding of proteins, or micelles^{110–113}, where hydrophilic and hydrophobic interactions play an important role. Water structures are also found in space, e.g. on interstellar dust grains and comets. These water structures play an important role in the formation of planets and stars^{114–116}. In the field of materials and surface science, self-assembled monolayers are studied to design functional surfaces. The characteristics of such surfaces can be fine tuned from very hydrophilic to very hydrophobic by using different functional groups^{117,118}. Single-walled carbon nanotubes are used as model systems to study interfacial properties of nanoconfined water. Water can form a hydrogen-bonded network through the hydrophobic tubes^{119,120}. A change in temperature can result in a hydrophobic-hydrophilic transition¹²¹. The interaction between water and metal catalysts is also important in electrochemical systems such as low temperature fuel cells and other aqueous electrochemical systems. In these systems, water and other molecules interact with a metallic electrode material.

Three extensive reviews have summarized the interaction and reaction of water and co-adsorbates with metal and metal oxide surfaces^{122–124}. These studies show that the interfacial water structure depends, amongst other variables, on the metal identity and atomic structure, the surface temperature, and pressure. On surfaces such as $Cu(111)$, $Ag(111)$, and $Au(111)$, water forms 3-D ice clusters, implying that these surfaces are non-wetting. On other surfaces, such as $Pt(111)$, $Pd(111)$, and $Ru(0001)$, water initially forms a wetting layer. The structure of this first layer determines whether or not a second wetting layer is formed¹²⁴. Even the unit cell structure of the first layer varies with metal identity and atomic structure. On $Pt(111)$, a hexagonal water structure is formed¹²⁵, whereas on $Cu(110)$ interlinked pentamers have been observed¹²⁶. It is also well documented that depending on the growth temperature, various multilayered structures can be formed. A water monolayer dosed on a $Pt(111)$ surface at temperatures below 135 K, yields so-called amorphous solid water (ASW)¹²⁷. When water is dosed at a higher temperature, or during a temperature ramp, crystalline ice (CI) structures are formed¹²⁵.

Single atomic steps at surfaces may also influence the structure of adsorbed water. Thürmer and Nie showed that cubic ice (I_c) is grown in spirals created by

screw dislocations above substrate steps¹²⁸. They also showed that in thin water films, hexagonal ice (I_h) is favored, while in thicker films, mostly I_c is formed. In the submonolayer regime, Morgenstern *et al.* showed, using scanning tunneling microscopy (STM), that water adsorbs preferentially at the upper side of steps at low coordination sites on Pt(111). For rectangular (110) steps, short chains or clusters seemed to appear, whereas for the square (100) steps, molecular chains are formed¹²⁹. On Ag(111), a 1-D amorphous structure is formed when water is adsorbed at 70 K. A 2-D bilayer grows at the lower step edge, on which a second layer nucleates heterogeneously¹³⁰.

The steps and defects in the (111) facet are believed to be catalytically active sites for many reactions⁹. Water prefers to bind at step edges and corners on catalyst nanoparticles (gray atoms in figure 6.1a). This figure shows a schematic representation of an fcc metal catalyst particle with square (100) and hexagonal (111) facets¹³¹. The terrace length and amount of defects depend on the diameter of the nanoparticle. The presence of the various surface structures makes it difficult to study fundamental reaction steps on nanoparticles. To gain more insight in the catalytic activity at platinum surfaces, Pt single crystals have been studied. The (111) facet is modeled by a Pt(111) surface (figure 6.1b). The effect of defect sites can be modeled by the use of stepped single crystal surfaces, e.g. using variable terrace lengths (figure 6.1c-e).

Platinum is a good catalyst for many electrochemical reactions, where the interaction of water with the Pt surface as well as with other species is relevant. The interaction of water with Pt(111) is well studied and shows considerable complexity^{125,127,129,132–143}. Fewer experimental studies have investigated the interaction of water with platinum surfaces with defects that are naturally present on the surface¹²⁹, or regularly stepped surfaces^{95,144,145}. In systems such as the hydrogen-oxygen fuel cell other species, e.g. adsorbed hydrogen or oxygen atoms and hydroxyl groups, are also present. Therefore, co-adsorption studies including water at different platinum surfaces are highly relevant and may serve as model systems. D_2O on a Pt(111) surface is slightly stabilized in the presence of a small amount of deuterium¹⁴⁶. For higher D-precoverage, it is approximately as stable as on the bare Pt(111) surface. Both bare Pt(111) and D/Pt(111) are hydrophilic, i.e. water wets the surface prior to forming multilayered structures. We have shown previously that pre-deuteration of surfaces with (100) and (110) steps separating short 4-atom wide (111) terraces has very different effects, depending on the step ge-

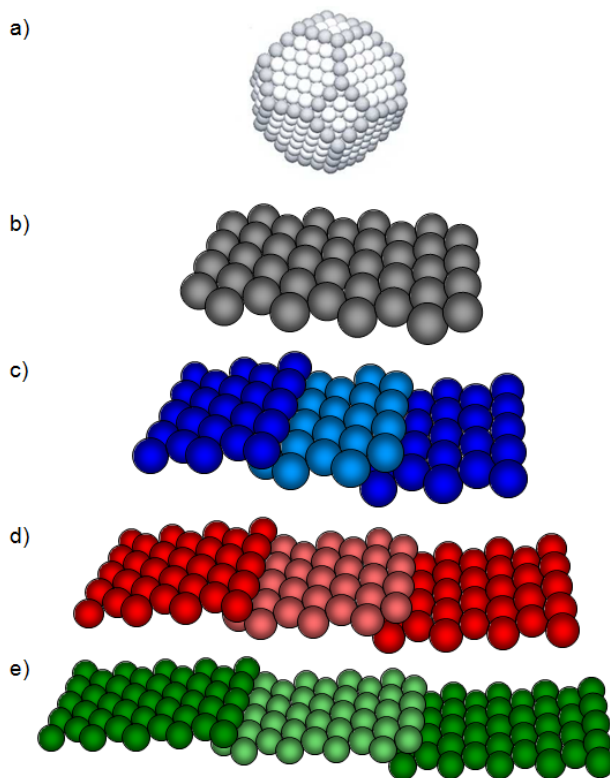


Figure 6.1: Schematic representation of a) 2.74 nm diameter Pt nanoparticle, from ¹³¹, b) Pt(111), c) Pt(533), d) Pt(755), and e) Pt(977).

ometry. On both surfaces, the step-related stabilization of water disappears when a small amount of D is precovering the surfaces. The pre-deuterated surface with (110) steps is still hydrophilic. Conversely, the pre-deuterated surface with (100) steps is hydrophobic. Water forms ASW clusters near step sites on D/Pt(533) ¹⁴⁷.

Here, we expand upon our elucidation of the water structures in contact with bare and pre-deuterated stepped Pt surfaces with (100) steps and (111) terraces (Pt[$n(111) \times (100)$]). The terrace width (n) varies from 4 (Pt(533), figure 6.1c), to 6 (Pt(755), figure 6.1d), to 8 atoms (Pt(977), figure 6.1e). This reflects relevant nanoparticle systems with a diameter up to ~ 7 nm. We compare the results of the stepped surfaces to the flat Pt(111) surface. We use temperature programmed

desorption (TPD) in combination with isotopic labeling, to investigate the role of terrace width in the hydrophobicity/hydrophilicity and the exchange between D_{ad} and H_2O . Significantly, our results show a strong long-range influence of step sites on the adsorption of water layers on clean and D-covered platinum surfaces, showing that the perturbative effect that defects may have on water-covered Pt surfaces extends well beyond the immediate vicinity of the defect.

6.2 Experimental

Experiments were performed in an ultra-high vacuum (UHV) apparatus containing LEED/Auger Electron Spectroscopy (LK Technologies, RVL 2000/8/R), a quadrupole mass spectrometer (QMS, Pfeiffer QME 200), and various leak valves. The base pressure of the system was $< 2 \cdot 10^{-10}$ mbar during experiments. The Pt crystals (cut and polished $< 0.1^\circ$, Surface Preparation Laboratory, Zaandam, The Netherlands) were cleaned by repeated cycles of Ar^+ bombardment (Messer, 5.0; 20 μA , 10 min), annealing between 850 and 1000 K in an oxygen atmosphere (Messer, 5.0; $2 \cdot 10^{-8}$ mbar, and annealing at 1200 K. The crystal temperature can be controlled between 84 and 1200 K with the use of liquid nitrogen for cooling and radiative heating combined with electron bombardment for heating.

Water from a Millipore Milli-Q gradient A10 system (18.2 M Ω resistance) was deaerated in a glass container by multiple freeze-pump-thaw cycles and kept at a total pressure of 2.0 bar helium (Air Products, BIP Plus). A water bath ($\sim 30^\circ C$) was used to keep the vapor pressure of the water in the glass container constant. The container was connected to a home-built glass capillary-array doser located ~ 1.5 cm from the sample. Water was dosed directly on the surface at $T_s \leq 110$ K at a rate of ~ 0.009 ML/s by measuring the pressure rise due to the co-dosed helium.

To minimize hydrogen contamination from background adsorption, all filaments were switched off during D_2 dosing (Lindegas, 2.8; background dosing, $2 \cdot 10^{-7}$ mbar while cooling down the sample from 500 to 100 K (~ 5 min)). This produced a full monolayer of D_{ad} . To vary the amount of deuterium on the surface, we first create a full monolayer of D_{ad} , then we remove a part from the surface by ramping the crystal to a set temperature with 1 K/s and subsequently cooling the crystal to 100 K before measuring TPD spectrum. All reported pressures are uncorrected for ion gauge sensitivity.

For the co-adsorption experiments, deuterium was adsorbed first. After the pressure in the system had reached the base pressure, water was dosed on top of the (partly) deuterated surface.

For TPD spectroscopy the heating rate was 1 K/s. During heating $m/e = 2$ (H_2), 3 (HD), 4 (D_2), 18 (H_2O), 19 (HOD), and 20 (D_2O) were monitored with the QMS. We have verified that cracking in the QMS ionizer of HOD and D_2O yields no significant contribution to the signal at $m/e = 18$ at the low signal intensities in experiments for $m/e = 19$ and 20. Therefore, the signal at $m/e = 18$ results only from H_2O within experimental error. Similarly, the signal at $m/e = 19$ results only from HOD and the signal at $m/e = 20$ only from D_2O . Experiments where only water is dosed onto the crystal show that there is no significant amount of $m/e = 20$ desorbing from the surface (either from $H_2^{18}O$ or D_2O). Therefore, we do believe that in our experiments with co-adsorption of D_2 and H_2O , $m/e = 20$ results from D_2O desorption and not from $H_2^{18}O$. For data analysis $m/e = 2$ was not taken into account, since the signal is negligibly small and mainly due to D^+ and not H_2^+ . Initially, $m/e = 28$ (CO or N_2) and 32 (O_2) were monitored as well, but no desorption was detected. All H_2O and D_2 coverages are calculated from the integrated TPD peak areas. Following Grecea *et al.*¹⁴⁵, we define 1 monolayer (ML) of water as the largest combined integral for the two high temperature peaks on each of the stepped Pt surfaces, or the integral of the single high temperature peak for Pt(111). We are not aware of an unambiguous means to determine the integral for 1 ML HOD desorbing from the surface. Therefore, we have used the integral for 1 ML H_2O (desorbing from bare Pt) as a reference in quantifying the amounts of H_2O and HOD. We assume that the cracking ratio in the QMS and channeltron amplification are similar for both isotopes, because of the relatively small difference in mass/charge ratio. We define 1 ML of deuterium as the maximum integrated area of the spectrum, without implying a $D_{ad} : Pt$ ratio of 1:1, as was shown for the Pt(533) surface⁹⁵. We have corrected the temperature of the Pt(755), Pt(977), and Pt(111) surfaces by shifting the complete temperature range by at most 3.3 K. We have done this in order to align the onset of the second water layer desorption to that of Pt(533). This may be expected to be the same for every crystal independent of its structure or type of metal¹²⁴, although we acknowledge that kinetic factors may play a role leading to differences between the various step widths. Here, we expect that small changes in the temperature readout of the different crystals are caused by differences in the attachment of the thermocouple wires to the various crystals. We therefore believe

that the temperature shift is reasonable and necessary.

The H₂O TPD spectra show an almost stepwise increase in their baseline. This is due to the high vacuum time constant of water in our UHV system. A reasonable approximation for the baseline is given by:

$$y = y_0 + \frac{1}{2}\Delta y * \left(\tanh\left(\frac{T - T_0}{\Delta T}\right) + 1 \right) \quad (6.1)$$

where Δy is the total increase in the height of the baseline, T_0 is the center of the S-curve, typically slightly before the peak maximum, and ΔT is an arbitrary parameter to smooth out the \tanh . Note that the value of ΔT does not matter for the total obtained integral, though it may affect the relative intensities of smaller peaks at lower temperatures. We have verified that this baseline correction procedure does not influence the leading edges of our TPD data if ΔT and T_0 are kept constant. An example of the raw data and the background correction of water desorption from Pt(553) were shown in a previous article¹⁴⁸.

6.3 Results and discussion

6.3.1 H₂O desorption from Pt(111), Pt(533), Pt(755), and Pt(977)

Figure 6.2 shows the H₂O desorption spectra from the four surfaces as well as the deconvolution into two or three Gaussian line shapes. Although the fits are not perfect, they give a good approximation for the integrated peak areas. On Pt(111) (figure 6.2a), the water desorption spectrum shows two peaks located at 168 K and 152 K. For low water dosage, only the high temperature peak is observed and it shifts from around 163 K to 168 K with increasing water coverage. These results are very similar to the results that Daschbach *et al.* reported for sub-monolayer water desorption from Pt(111)¹²⁷. They used a heating rate of 0.6 K/s and dosed water at 100 K. Their water desorption peak shifts from ~ 158 K for very low water coverage to ~ 168 K for 1 ML of water. When more than 1 ML of water is dosed, a second lower-temperature peak appears that shifts from approximately 148 K to 158 K with increasing water coverage (not shown). Since Daschbach *et al.* did not report a second peak, we compare these results to results from Haq *et al.*¹²⁵. They dosed water at a slightly higher temperature of 137 K, in order to obtain a Cl film on the Pt(111) surface, and used a heating rate of 0.65 K/s. They also

observed a peak shifting from ~ 160 K to 168 K with increasing water dosage corresponding to submonolayer water desorption from Pt(111). In their work, with more than 1 ML dosed onto the surface, a low temperature peak appears that shifts from ~ 148 K to 152 K for 1.7 ML of water. This low temperature peak was assigned to water desorption from the second layer. Since our results are very similar to these literature results, we also assign the high temperature peak (around 168 K) to water desorption from the bare Pt(111) and the low temperature peak (around 152 K) to water desorption from water in the second layer.

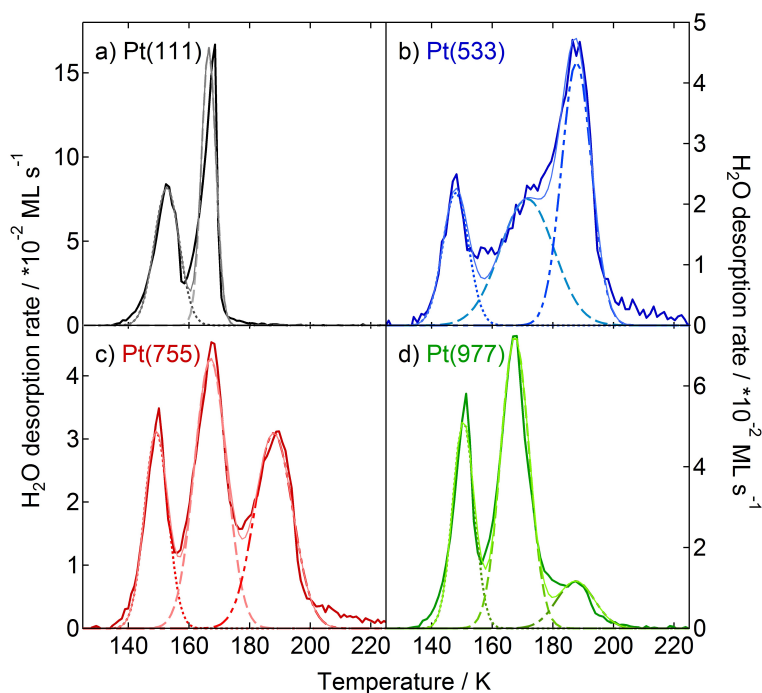


Figure 6.2: Deconvolution of the H_2O desorption spectra from bare surfaces into a) two Gaussians for Pt(111) (1.83 ML), and into three Gaussians for b) Pt(533) (1.24 ML), c) Pt(755) (1.36 ML), and d) Pt(977) (1.48 ML).

For Pt(533) (figure 6.2b), the water desorption spectrum is deconvoluted into three Gaussian line shapes. The results of water desorption from bare Pt(533) were reported in an earlier publication¹⁴⁹ and for completeness' sake we summarize the main findings here briefly. For water coverages below 0.25 ML, there is a peak around 184 K that shifts to 188 K with increasing coverage. For coverages higher

than 0.25 ML, this peak does not shift anymore until saturation of this peak. A second intermediate temperature peak (around 167 K) appears prior to saturation of the high temperature peak. When both the high and intermediate temperature peaks are saturated, a third low temperature peak appears around 150 K shifting to higher temperatures with increasing water dosage. We assigned the peak at 188 K to water desorption from the (100) steps on the Pt(533) surface, the peak at 167 K to water desorption from (111) terrace sites on this surface, and the peak around 150 K to desorption from the second water layer. The water desorption spectra from both Pt(755) (figure 6.2c) and Pt(977) (figure 6.2d) also show three peaks, located at 188 K, 167 K, and around 150 K. Figure 6.3b collects the TPD spectra in one figure and clearly shows that the desorption peak of water in the second layer, the desorption peak of water from (111) terraces, and the desorption peak of water from the (100) steps show perfect correspondence for all three stepped surfaces. The two low temperature peaks of the stepped surfaces also align with the peaks from Pt(111) corresponding to water desorption from the monolayer and second layer. The amount of water desorption from steps decreases with decreasing step density from Pt(533) to Pt(755) to Pt(977) and eventually disappears for Pt(111), whereas the amount of water desorption from (111) sites increases. Since the peak temperatures of the spectra of Pt(755) and Pt(977) are very similar to those of Pt(533) (and Pt(111)), we assign the low temperature peaks (around 150 K) in figure 6.2c (Pt(755)) and figure 6.2d (Pt(977)) to desorption of water in the second layer, the peaks at 167 K to water desorption from the (111) terraces, and the peaks at 188 K to water desorption from the (100) steps on Pt(755) and Pt(977).

It is informative to analyze the Gaussian line shapes for the water desorption peaks from (111) terraces and from (100) steps (figure 6.2). Table 6.1 compares the ratio between the integral of the (100) step site peaks to the (111) terrace site peaks to the step density for the three stepped Pt surfaces. Pt(533) has a step density of 0.109 \AA^{-1} . For instance, the ratio between the step peak and the terrace peak is 1.16 for this surface. Even though we describe Pt(533) as a surface of 4 atom wide (111) terraces, separated by (100) steps, the presence of steps seems to have a larger influence on the stabilization of water as would be expected from pure geometrical considerations. DFT (density functional theory)¹⁴⁵ and STM¹²⁹ studies have suggested that water molecules desorbing in the high temperature peak, may originate from both the upper and lower sides of the (100) steps and maybe also at least in part from the (111) terraces close to the steps.

Table 6.1: Terrace width, step density, water desorption from steps to terrace ratio, and peak width FWHM for Pt(111), Pt(977), Pt(755), and Pt(533)

Surface	Ter width	Step density	INT(step)/INT(ter)	Ter FWHM	Step FWHM
Pt(111)	infinite	-	-	5.6 K	-
Pt(977)	8 atoms	0.054 \AA^{-1}	0.21	11.2 K	14.6 K
Pt(755)	6 atoms	0.072 \AA^{-1}	0.86	12.6 K	14.9 K
Pt(533)	4 atoms	0.109 \AA^{-1}	1.16	20.8 K	11.6 K

For Pt(755), with a step density of 0.072 \AA^{-1} , the ratio between step stabilized water and terrace stabilized water is 0.86, and for Pt(977), with a step density of 0.054 \AA^{-1} , this ratio is 0.21. The relative amounts of step- vs. terrace-bound water exhibit non-intuitive and non-linear changes with step density and terrace width. The ratio between the step stabilized water vs. the terrace stabilized water decreases faster with increasing terrace width than expected from the geometry of the surfaces. This indicates that the binding of water near steps seems to influence water at terraces more when the terraces are shorter. It appears that this is mirrored by the width of the intermediate temperature peak corresponding to water desorbing from (111) terraces. On Pt(111), this peak is rather sharp with a full width at half maximum (FWHM) of 5.6 K. The peak becomes broader as the terrace width decreases from 8 atom wide terraces (FWHM of 11.2 K for Pt(977)) to 6 atom wide terraces (FWHM of 12.6 K for Pt(755)) to 4 atom wide terraces (FWHM of 20.8 K for Pt(533)). At the same time, the (100) step peak width increases from 11.6 K on Pt(533) to 14.9 K on Pt(755). The peak of water desorption from the (100) steps on the Pt(977) surface is relatively small, which causes the slightly more narrow peak width (14.6 K) compared to the step peak width of the Pt(755) surface. Nevertheless, the variation in the peak width corresponding to water desorption from steps appears less than in the peak width variation for water desorbing from the terraces. The sharpness of the TPD peak is a measure of the lateral interactions between the species desorbing in the peak, a narrower peak signifying more strongly attractive interactions¹⁵⁰. On a Pt(111) surface, water forms a highly ordered 2-D network characterized by strong hydrogen bonding interactions. Introducing steps into the surface, breaks this 2-D order, weakening the overall influence of lateral hydrogen bonding. On a relatively narrow terrace such as on Pt(533), this much reduced 2-D hydrogen bonding network leads to a broad peak. The more moderate variation in peak width from step desorption suggests a more 1-D type nature of the lateral

interactions on the steps. This interpretation is consistent with STM imaging of low water coverages on Pt(111), where H_2O binds initially along step edges only¹²⁹.

Summarizing, steps influence the binding of water to well-defined platinum surfaces in a way that is long-ranged and that cannot be considered as an additive perturbation to the terrace adsorption of water. Steps break the ability of terrace-bound water to hydrogen bond, and the number of water molecules whose binding energy is influenced by the presence of steps is a non-linear function of step density.

6.3.2 H_2O desorption from D precovered Pt(111), Pt(533), Pt(755), and Pt(977)

Figure 6.3 shows a comparison between water TPD spectra from (a) completely D-precovered and from (b) bare Pt(111), Pt(533), Pt(755), and Pt(977). Pt(111) shows two water desorption peaks for both the bare surface and the D-precovered surface. The low temperature peak depends on the amount of water in the second layer that is dosed on the (D-precovered) surface and will therefore not be discussed in detail. The high temperature peak is located at a slightly higher temperature for the completely D-precovered Pt(111) surface (171 K) compared to the bare Pt(111) surface (168 K). This stabilization of water on D-precovered Pt(111) has been noted before by Petrik and Kimmel¹⁴⁶, who observed a high temperature peak for D_2O desorption located at 170 K. For small amounts of predosed deuterium, their peak was stabilized up to a temperature of 175 K. When more deuterium precovers the surface, this stabilization decreased to a peak temperature of 171 K for the completely D-precovered Pt(111) surface. Note that this desorption temperature indicates that water is still more stable on the completely D-precovered surface than on the bare Pt(111) surface. Our water desorption peak temperatures are somewhat different compared to those of Petrik and Kimmel, but the trends are the same. Our bare Pt(111) surface shows a water desorption temperature of 168 K. When half of this surface is precovered with D (figure 6.4a), the desorption temperature increases to 172 K. When the surface is completely precovered with D, the temperature decreases to 171 K, but it is still more stable than on bare Pt(111). Apparently water can still form a stable 2-D hydrogen-bonded network on the D/Pt(111) surface and it is slightly more stable than on the bare Pt(111) surface.

Whereas water desorption from bare Pt surfaces with (100) steps show three

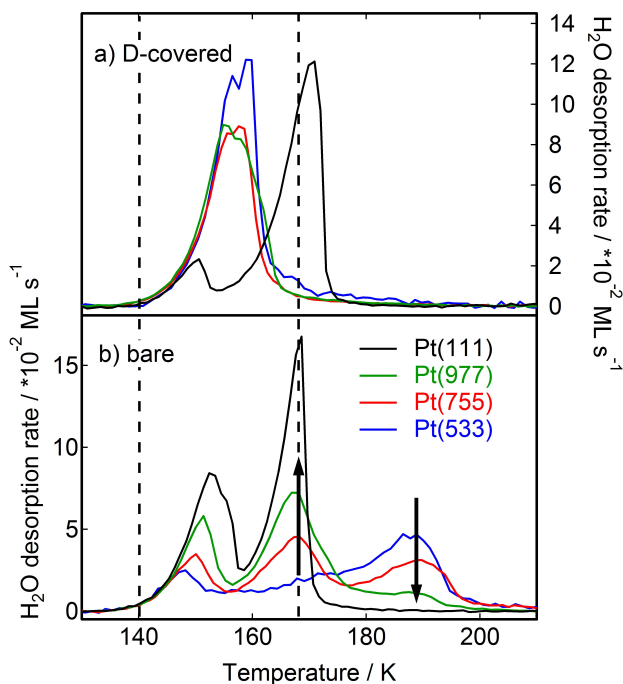


Figure 6.3: Comparison of H_2O TPD spectra from a) D-covered, and b) bare Pt(111) (black), Pt(533) (blue), Pt(755) (red), and Pt(977) (green). The black arrows indicate the decrease in water desorption from steps and increase in water desorption from terraces as the terrace width increases.

peaks for the water desorption, i.e at 188 K (steps), 167 K (terraces), and around 150 K (second and multilayer), the completely D-precovered surfaces only exhibit one peak corresponding to the multilayer water desorption regime for all three stepped surfaces. Even Pt(977), with eight atom wide (111) terraces, shows only a single desorption feature for water when the surface is completely precovered with D. The water destabilization on D/Pt(533) has been described in an earlier publication¹⁴⁹ and has also been compared to D/Pt(553)¹⁴⁷. Close to deuterium saturation of the Pt(533) surface, water forms 3-D ASW clusters near step sites. These ASW clusters are large enough to show a deflection in the TPD spectra at a temperature of around 157 K, which is characteristic of ASW transformation into CI^{149,151}. This implies that H_2O no longer spreads over the surface to form a hexagonal structure with hydrogen bonds, suggesting the hydrophobic character of D/Pt(533). The step-

bound D also disrupts the tendency of water to organize itself neatly in 1-D chains along the upper edge of the (100) step. Initial adsorption of H_2O forms D- H_2O clusters, which can be subsequently hydrated by additional H_2O . Broadening the 4 atom wide (111) terraces of Pt(533) to the 6 or 8 atom wide (111) terraces of Pt(755) and Pt(977), still results in a completely hydrophobic surface when fully precovered with D. These surfaces exhibit a single water desorption peak in the second water layer desorption regime, with the deflection of ASW crystallization into CI around 157 K. Since D/Pt(111) and D/Pt(977) show very different water adsorption properties, it seems that the (100) steps have a very strong and long-ranged influence on the surface hydrophobicity, particularly when the surface is precovered with D. On the bare surfaces, the influence of the (100) steps is less pronounced for broader terraces (figure 6.2 and 6.3b), with the broadness of the peak suggesting that water forms a more extensive hydrogen bonded network on the broader (111) terraces. However, on the D-precovered surfaces with (100) steps, the terrace width has essentially no impact on the water desorption, at least not for the terrace widths considered here. Apparently the step-bound D forces water to form 3-D ASW clusters near step sites largely independent of the width of the neighboring terraces. The stable water layer that adsorbs on the D-covered Pt(111) surface is completely absent on the stepped surfaces, even on Pt(977). This illustrates the highly long-ranged effect that steps may exert on water adsorption, even on well-ordered Pt surfaces.

To illustrate the role of the coverage by D, figure 6.4 compiles water desorption spectra from Pt(111) (a) and Pt(755) (b) for various amounts of D-precoverage. When D-precovers a Pt(111) surface, the H_2O monolayer is first stabilized, but for higher D-precoverage the temperature shifts back to a temperature that is just slightly higher than water desorption from the bare surface, as was discussed above. For the stepped Pt(533) (not shown), Pt(755), and Pt(977) (not shown) surfaces, the H_2O stabilization near (100) step sites rapidly disappears when small amounts of deuterium precover the step sites. The water desorption from (111) terraces is only observed for small amounts of D-precoverage on all stepped surfaces. As on Pt(111), this desorption temperature increases first when a small amount of D is present. In contrast to Pt(111), increasing the D coverage on the stepped surfaces destabilizes water adsorption on the (111) terraces very rapidly, until the surfaces become completely hydrophobic as manifested by water adsorbing as ASW near step sites.

Figure 6.5a plots the shift in maximum desorption temperature for water desorp-

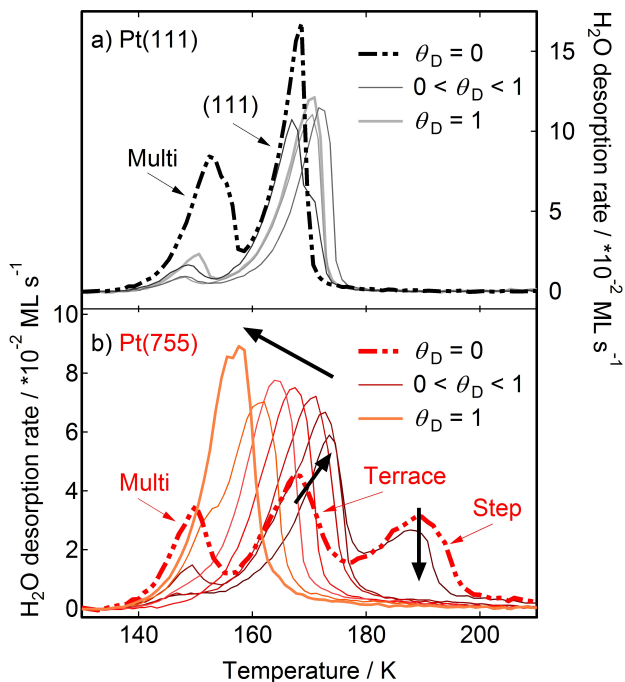


Figure 6.4: H_2O TPD spectra for various precoverages of D on a) Pt(111), and b) Pt(755). Consecutive D-coverages for Pt(111) are 0, 0.20, 0.47, 0.97, and 1.0 ML. Consecutive D-coverages for Pt(755) are 0, 0.06, 0.17, 0.33, 0.54, 0.71, 0.84, and 1.0 ML. The thick black arrows in section b indicate the destabilization of water at step sites, the initial stabilization of water at the terrace, followed by the fast destabilization.

tion from the (111) facets (the peak around 167 K) of Pt(111), Pt(533), Pt(755), and Pt(977) as a function of the deuterium coverage on the step sites ($\theta_{D,step}$) and on the terrace sites ($\theta_{D,terrace}$). There are three different influences of the D coverage. First, when D is precovering the (100) step sites, H_2O stabilization near step sites (the peak around 188 K) rapidly disappears. The second effect is that water on the (111) terraces (the peak around 167 K) is stabilized when D is precovering the step sites, which was also observed on Pt(111), where the desorption temperature increases first when a small amount of D is precovering the surface. On all stepped surfaces, the desorption temperature of the H_2O peak has a maximum when the steps are precovered with D. The third influence of D is that when D starts to precover the (111) terrace sites, on the stepped surfaces this leads to a desta-

bilization of water on the (111) terraces. The desorption temperature drops to the value where the second water layer desorption takes place. This means that all stepped surfaces become hydrophobic when the whole surface is precovered with D, whereas on D precovered Pt(111), the water is stabilized, as clearly illustrated in figure 6.5a.

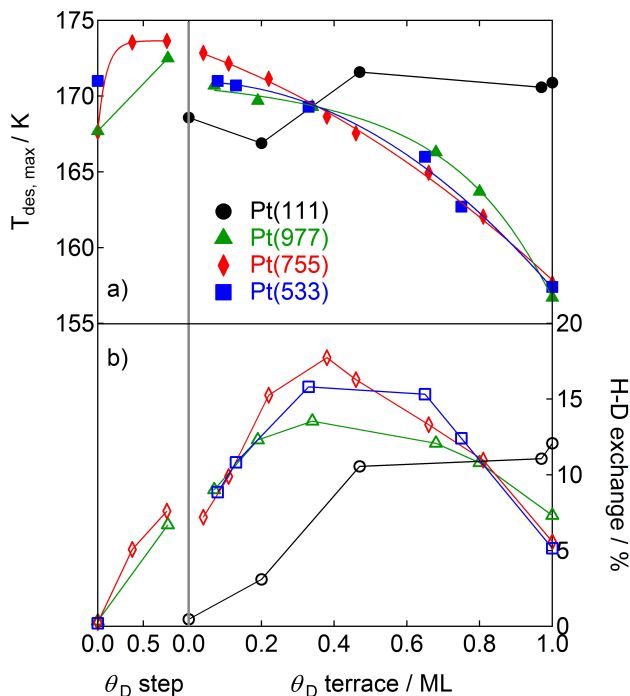


Figure 6.5: a) Maximum desorption temperature, and b) the percentage of H-D exchange, as a function of D coverage on the (100) steps and (111) terraces for Pt(111) (black circles), Pt(533) (blue squares), Pt(755) (red diamonds), and Pt(977) (green triangles). Lines are only a guide for the eye.

Figure 6.5b shows the percentage of H-D exchange between H_2O and deuterium as a function of $\theta_{D, step}$ and $\theta_{D, terrace}$. This percentage is determined by taking the integral of the HOD (one H-D exchange) and two times the D_2O (two H-D exchanges) signal divided by the integral of the total water desorption (combined H_2O , HOD, and D_2O signal). All three stepped surfaces show a maximum H-D exchange when approximately 0.4 ML of deuterium precovers the terraces. This does not appear to depend on the actual terrace width, but only on the percentage that is

covering the terraces. Again, Pt(111) shows completely different behavior. For this surface, the amount of exchange always increases with increasing D coverage. It seems that the (100) steps catalyze the exchange reaction between H and D atoms from H_2O and D_2 , since the amount of exchange on all stepped surfaces is higher than on the Pt(111) surface. However, for a D-precoverage higher than around 0.4 ML, the amount of exchange on the stepped surfaces starts to decrease. When more than around 0.8 ML of D is precovering the stepped surfaces, the total amount of H-D exchange is smaller than the H-D exchange on Pt(111). This is in agreement with the idea that when the (111) terraces of the stepped surfaces are precovered with D, the stepped surface becomes hydrophobic, forcing water into ASW snowballs on the steps. As a result, a smaller fraction of the adsorbed water is in direct contact with $D/Pt(S)$, resulting in a lower H-D exchange. We believe that the exchange between D and H_2O takes place through the formation of a hydronium intermediate, which have been observed on Pt(111)¹⁵² and Pt(100)¹⁵³ by infrared spectroscopy.

6.4 Conclusion

In this paper, we have shown that truncating an infinite (111)-type terrace by the introduction of steps, may affect the surface chemistry and surface physics of water in a way that does not scale linearly with terrace width or step density. Strong lateral interactions and step-induced preferences in adsorption or orientation affect binding of water at terrace sites even if they seem significantly remote from the step edge. Introduction of steps significantly perturbs the energetics of water ordering on (111) terraces, as evidenced by broadening of the water desorption peak from (111) terraces. Interestingly, the width of the peak corresponding to water desorption from steps is much less influenced by terrace width, testifying to the 1-D character of water interactions at steps. In the presence of D on the stepped Pt surfaces with (100) steps, a high D coverage makes all water accumulate at the step sites, largely independent of terrace width. These remarkable observations illustrate the highly subtle interactions between H_2O , D and Pt, showing that a stepped or defected surface in contact with water is far from a linear combination of terrace and step/defect effects. Steps exert a long-ranged effect on the adsorption of water on well-defined platinum surfaces; in the presence of hydrogen or deuterium, this even leads to an

adsorption behavior that is completely dominated by steps, even for relatively wide terraces. We believe that these results may have important implications for catalytic reactions taking place at the platinum-water interface, as we expect that the fundamental interactions responsible for this behavior will still be present at higher pressures and temperature.

Chapter 7

Future prospects

So far, our group has gained valuable knowledge on relevant systems by studying the interaction of molecules with metal surfaces under ultra-high vacuum conditions. Background adsorption of a single type of molecules on flat single crystals is considered a relatively simple type of experiment. The use of supersonic molecular beam techniques and regularly stepped single crystals already increases the complexity of the studied system. We have also studied the interaction of multiple types of molecules (co-adsorption via background) with stepped single crystals. Our UHV apparatus is actually a unique machine than can be used for even more complex measurements, since it has two molecular beams connected to it. In the future, we hope to be able to study the interaction of at least two types of adsorbing molecules via the supersonic molecular beam (SSB) and the effusive beam (EB) on curved single crystals. This chapter provides a short proof-of-principle of the use of the double beam and of the use of curved single crystals.

7.1 Double beam

The UHV machine has been rebuilt in the last few years. More than five years ago, it was a normal and simple surface science machine, capable of adsorbing molecules on surfaces via the background and only equipped with a LEED and QMS for TPD experiments. In the mean time, it was completely remodeled. It now contains a supersonic molecular beam (SSB, as used for the experiments in chapter 3, 4, and 5) and an effusive molecular beam (EB). A schematic top view of the beam

lines is shown in figure 7.1. As described before, the double differentially pumped supersonic molecular beam passes through a set of skimmers and a chopper wheel with a 16% duty cycle. The beam can be modulated by two flags (SSB1 and SSB2) and the slide can separate the entire SSB from the main chamber. The single differentially pumped effusive beam also passes through a set of skimmers. There is one gate (EB1) separating the EB from the main chamber and one flag (EB2) to prevent the beam from impinging onto the crystal directly.

The ratio of molecules in the SSB and EB can easily be adapted by changing the settings of the flow controllers to find an optimal rate for the formation of certain molecules. However, changing the settings will result in different beam conditions, which might also influence the reaction. A different way of changing the flux of the SSB is to keep the chopper wheel in the open position or to modulate the beam so that the incoming flux is reduced to 16%. A detailed analysis of the flux dependencies will provide information on the formation of molecules on stepped Pt. Here, only the proof-of-principle of HD formation from H_2 and D_2 and HOD formation from O_2 and a mixture of H_2 and D_2 is shown.

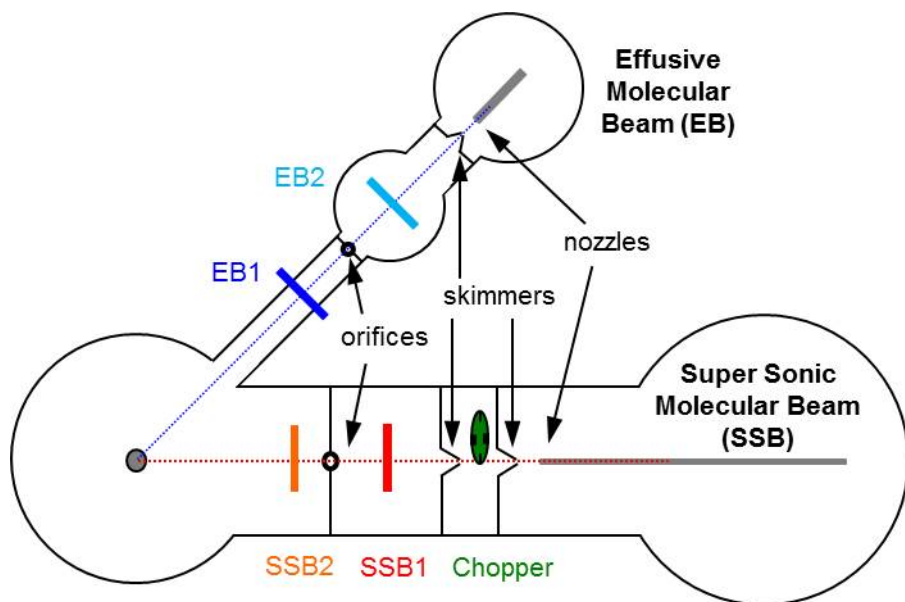


Figure 7.1: Schematic top view of the UHV machine Lion Fish with the SSB and EB lines.

We have studied HD formation on Pt(553) at a surface temperature of 500 K, while the crystal points in the direction between the two beams. Figure 7.2 shows the QMS intensities of H_2 (top, 4 ml/min in SSB, no chopping) and D_2 (middle, 0.5 ml/min in EB) and HD (bottom) as a function of time. A sequence of opening and closing the flags of both beams (see figure 7.1) results in changes of the HD, H_2 , and D_2 intensities. During the first 30 seconds all flags are closed so that we measure the background pressure of the different molecules. After 30 seconds, SSB1 is opened and the H_2 signal increases as the H_2 molecules enter the main chamber. They do not directly impinge onto the crystal yet. When SSB 2 is opened, the H_2 molecules can impinge onto the crystal. However, as the surface temperature is high, there are no stable chemisorbed hydrogen species on the surface. Therefore, the QMS intensity does not change. After closing SSB2 again, EB2 is opened and D_2 molecules from the EB enter the main chamber but do not directly impinge onto the crystal. EB2 is a gate valve and turning it results in noise in all signals. The D_2 and HD signals increase as expected since HD is partly present in the D_2 bottle and partly forms on other metal surfaces, such as the chamber walls and the filaments. When SSB2 is opened again, the H_2 molecules impinge onto the crystal directly. The H_2 signal slightly decreases, while the HD signal increases, indicating that part of the H_2 reacts on the surface with the background D_2 to form HD. When the EB2 is also opened, both beams impinge onto the crystal directly. The HD and D_2 signals increase significantly, while H_2 decreases. When SSB2 is closed, the HD signal decreases while the other signals increase. The H_2 does not directly impinge onto the crystal anymore. Less H_2 and D_2 react to form HD. Closing SSB1 results in a drop in H_2 and HD. The remainder of these signals results from the D_2 in the EB. The last steps are closing EB2 and EB1 and waiting until the signals stabilize again. Even though HD is already formed without both beams hitting the crystal directly, the Pt(553) crystal does increase the HD formation by a factor of about 2 under these conditions.

A similar type of experiment was performed to study the HOD formation from O_2 and a mixture of H_2 and D_2 on Pt(533) at a surface temperature of 500 K, while the crystal faces the SSB. Figure 7.3 shows O_2 (top, 4 ml/min in SSB, with chopper on), HD (middle, mixture of 4.8 ml/min H_2 and 4.8 ml/min D_2 in EB), and HOD (bottom) as a function of time. The reactants and products show similar behavior to the HD formation (figure 7.2). The O_2 signal shows a small drop when SSB2 is opened, due to dissociative adsorption of oxygen to the surface.

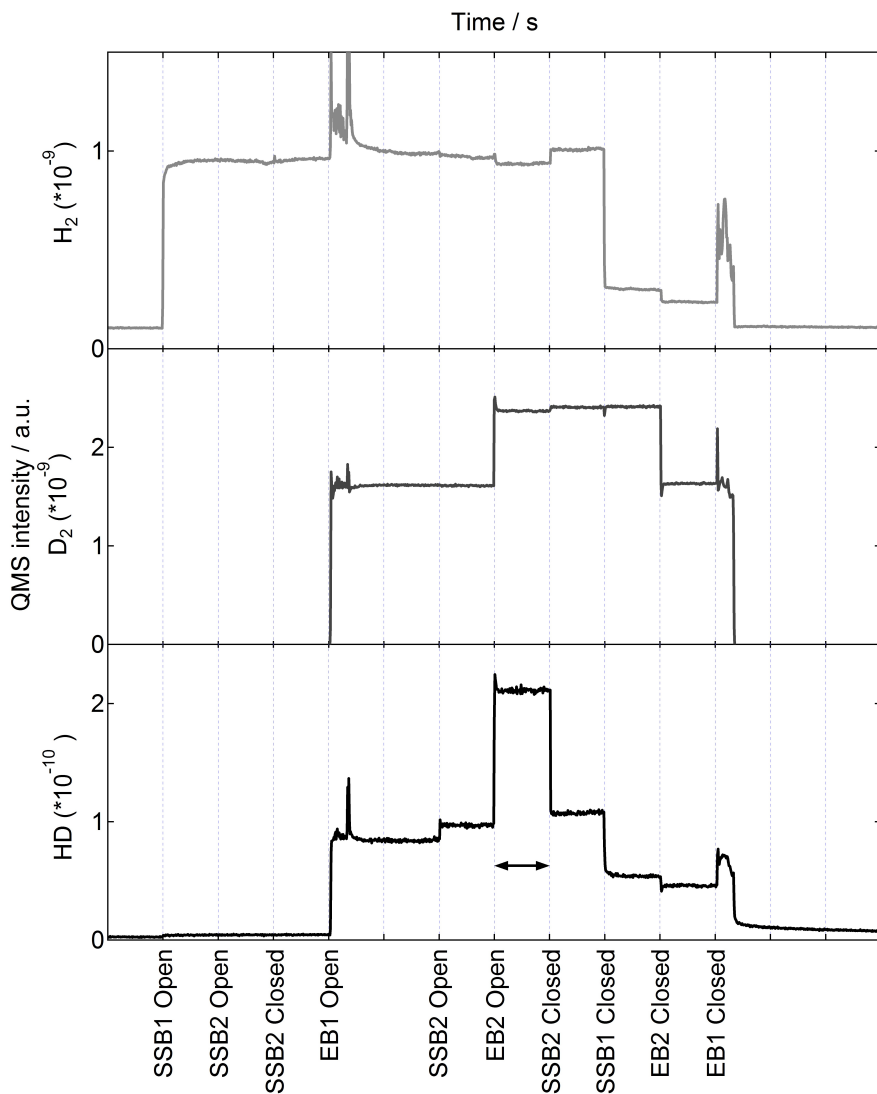


Figure 7.2: QMS intensity of H_2 (top), D_2 (middle), and HD (bottom) during a double beam experiment (4 ml/min H_2 in SSB, no chopper and 0.5 ml/min D_2 in EB) on Pt(553) at a surface temperature of 500 K. The arrow indicates the HD formation on the crystal when all flags are opened.

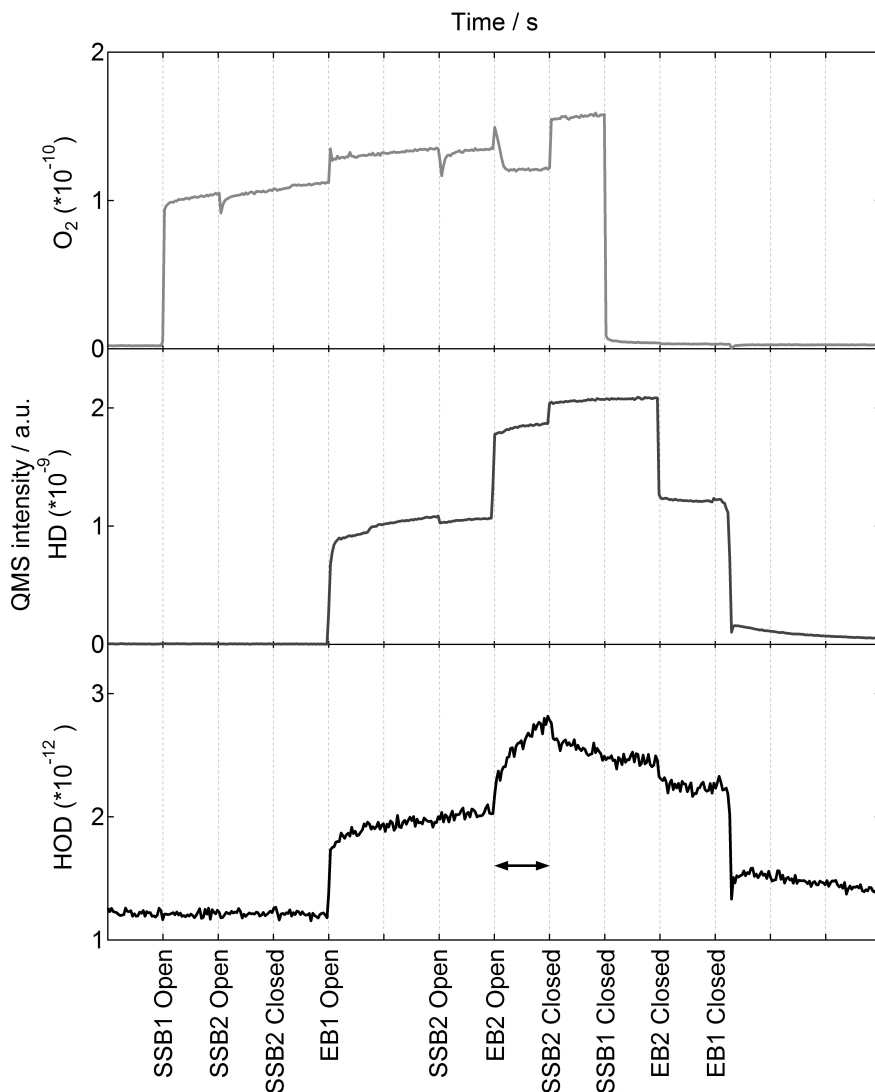


Figure 7.3: QMS intensity of O_2 (top), HD (middle), and HOD (bottom) during a double beam experiment (4 ml/min O_2 in SSB, chopper on, mixture of 4.8 ml/min H_2 and 4.8 ml/min D_2 in EB) on Pt(533) at a surface temperature of 500 K. The arrow indicates HOD formation on the crystal when all flags are opened.

When the surface is saturated, the intensity returns to the normal value (like the normal King and Wells experiments). When EB2 is opened, O₂ shows a small rise before it decreases. The HOD signal slowly increases when all flags are opened.

7.2 Curved single crystals

A single crystal can be cut in any direction to expose a certain surface structure. When it is cut in a cylindrical shape, a large variation of surface structures is exposed. A few years ago, measurements on a cylindrical Ni crystal have been performed with the use of a supersonic molecular beam. With only one crystal, the influence of step type and terrace length can be studied extensively^{154,155}. However, this type of crystal had a few drawbacks. As the crystal was large, it took a long time to heat and cool the sample and it can only be used in one machine. Recently, we started using curved single crystals. They have the size of our regular samples, heat and cool like the other samples, can be used in all of our systems, and still allow us to study a range of surface structures.

A schematic view of a curved crystal is shown in figure 7.4. The curved single crystal in this example contains (111) terraces with the (100) step type on the right side and the (110) step type on the left side. The real crystal exposes surface structures ranging from (111) in the middle to (533) and (553) at the sides. With this crystal, we can study the influence of terrace length from 4 atom wide atoms to 'infinitely long' (111) terraces for both (100) and (110) step type under identical conditions in a short amount of time. The combination of the curved crystals with the double molecular beam will not be easy. When everything works, it will yield valuable and unique new insights in the processes that take place in heterogeneous catalysis.

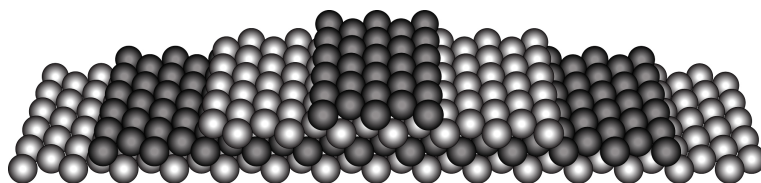


Figure 7.4: Schematic representation of a curved single crystal with (111) terraces and the (100) step type on the right and the (110) step type on the left.

Bibliography

- [1] I. Chorkendorff and J. W. Niemantsverdriet, *Concepts of Modern Catalysis and Kinetics*, Wiley-VCH, 2003.
- [2] Y. Shao, G. Yin, Z. Wang and Y. Gao, *J. Power Sources*, 2007, **167**, 235.
- [3] <http://energy.gov/eere/fuelcells/types-fuel-cells>.
- [4] H. A. Gasteiger, S. S. Kocha, B. Sompalli and F. T. Wagner, *Appl. Catal., B*, 2005, **56**, 9.
- [5] J. Greeley, I. E. L. Stephens, A. S. Bondarenko, T. P. Johansson, H. A. Hansen, T. F. Jaramillo, J. Rossmeisl, I. Chorkendorff and J. K. Nørskov, *Nat. Chem.*, 2009, **1**, 552.
- [6] J. K. Nørskov, T. Bligaard, J. Rossmeisl and C. H. Christensen, *Nat. Chem.*, 2009, **1**, 37.
- [7] G. J. Kroes, *Phys. Chem. Chem. Phys.*, 2012, **14**, 14966.
- [8] D. A. King and M. G. Wells, *Proc. R. Soc. London Ser. A*, 1974, **339**, 245.
- [9] M. T. M. Koper, *Nanoscale*, 2011, **3**, 2054.
- [10] W. P. Ellis and R. L. Schwoebel, *Surf. Sci.*, 1968, **11**, 82.
- [11] M. Henzler, *Surf. Sci.*, 1970, **19**, 159.
- [12] D. A. King, *Surf. Sci.*, 1975, **47**, 384.
- [13] J. W. Niemantsverdriet, *Spectroscopy in Catalysis*, Wiley-VCH, 2007.
- [14] G. Attard and C. Barnes, *Surfaces*, Oxford Science Publications, 1998.
- [15] C. Carbagno, A. Groß, J. Meyer and K. Reuter, *O₂ Adsorption Dynamics at Metal Surfaces: Non-Adiabatic Effects, Dissociation and Dissipation. From Dynamics of Gas-Surface Interactions.*, Springer, Berlin, 2013, vol. 50.
- [16] C. Stampfl, A. Soon, S. Piccinin, H. Shi and H. Zhang, *J. Phys.: Condens. Matter*, 2008, **20**, 184021.
- [17] E. Lundgren, A. Mikkelsen, J. N. Andersen, G. Kresse, M. Schmid and P. Varga, *J. Phys.: Condens. Matter*, 2006, **18**, R481.
- [18] P. D. Nolan, B. R. Lutz, P. L. Tanaka, J. E. Davis and C. B. Mullins, *Phys. Rev. Lett.*, 1998, **81**, 3179.
- [19] P. D. Nolan, B. R. Lutz, P. L. Tanaka, J. E. Davis and C. B. Mullins, *J. Chem. Phys.*, 1999, **111**, 3696.

- [20] A. C. Luntz, M. D. Williams and D. S. Bethune, *J. Chem. Phys.*, 1988, **89**, 4381.
- [21] A. C. Luntz, J. Grimblot and D. E. Fowler, *Phys. Rev. B*, 1989, **39**, 12903.
- [22] A. Groß, A. Eichler, J. Hafner, M. J. Mehl and D. A. Papaconstantopoulos, *J. Chem. Phys.*, 2006, **124**, 174713.
- [23] A. Groß, A. Eichler, J. Hafner, M. J. Mehl and D. A. Papaconstantopoulos, *Surf. Sci.*, 2003, **539**, L542.
- [24] C. T. Rettner and C. B. Mullins, *J. Chem. Phys.*, 1991, **94**, 1626.
- [25] C. T. Campbell, *Surf. Sci.*, 1985, **157**, 43.
- [26] P. D. Nolan, M. C. Wheeler, J. E. Davis and C. B. Mullins, *Acc. Chem. Res.*, 1998, **31**, 798.
- [27] G. R. Darling and S. Holloway, *Rep. Progr. Phys.*, 1995, **58**, 1595.
- [28] A. W. Kleyn, *Chem. Soc. Rev.*, 2003, **32**, 87.
- [29] A. Eichler, F. Mittendorfer and J. Hafner, *Phys. Rev. B*, 2000, **62**, 4744.
- [30] P. Sjövall and P. Uvdal, *Chem. Phys. Lett.*, 1998, **282**, 355.
- [31] C. Nyberg and C. G. Tengstal, *Surf. Sci.*, 1983, **126**, 163.
- [32] T. W. Orent and S. D. Bader, *Surf. Sci.*, 1982, **115**, 323.
- [33] C. Nyberg and C. G. Tengstal, *Solid State Commun.*, 1982, **44**, 251.
- [34] E. M. Stuve, R. J. Madix and C. R. Brundle, *Surf. Sci.*, 1984, **146**, 155.
- [35] S.-L. Chang and P. A. Thiel, *Phys. Rev. Lett.*, 1987, **59**, 296.
- [36] S.-L. Chang and P. A. Thiel, *J. Chem. Phys.*, 1988, **88**, 2071.
- [37] S.-L. Chang and P. A. Thiel, *Surf. Sci.*, 1988, **205**, 117.
- [38] G. Zheng and E. I. Altman, *Surf. Sci.*, 2002, **504**, 253.
- [39] D.-J. Liu and J. W. Evans, *Phys. Rev. B*, 2014, **89**, 205406.
- [40] J. Meyer and K. Reuter, *New J. Phys.*, 2011, **13**, 085010.
- [41] J. Meyer, *Ph.D. thesis*, Freie Universität Berlin, Berlin, 2011.
- [42] J. Meyer and K. Reuter, *Angew. Chem. Int. Ed.*, 2014, **53**, 4721.
- [43] B. L. M. Hendriksen, S. C. Bobaru and J. W. M. Frenken, *Surf. Sci.*, 2004, **552**, 229.
- [44] R. van Rijn, O. Balmes, A. Resta, D. Wermeille, R. Westerström, J. Gustafson, R. Felici, E. Lundgren and J. W. M. Frenken, *Phys. Chem. Chem. Phys.*, 2011, **13**, 13167.
- [45] B. Berenbak, D. A. Butler, B. Riedmüller, D. C. Papageorgopoulos, S. Stolte and A. W. Kleyn, *Surf. Sci.*, 1998, **414**, 271.
- [46] P. Junell, K. Honkala, M. Hirsimäki, M. Valden and K. Laasonen, *Surf. Sci.*, 2003, **546**, L797.
- [47] M. Beutl, M. Riedler and K. D. Rendulic, *Chem. Phys. Lett.*, 1995, **247**, 249.
- [48] M. Kay, G. R. Darling, S. Holloway, J. A. White and D. M. Bird, *Chem. Phys. Lett.*, 1995, **245**, 311.
- [49] A. Groß, S. Wilke and M. Scheffler, *Phys. Rev. Lett.*, 1995, **75**, 2718.
- [50] I. M. N. Groot, A. W. Kleyn and L. B. F. Juurlink, *Angew. Chem. Int. Ed.*, 2011, **50**, 5174.
- [51] R. A. Olsen, D. A. McCormack, M. Luppi and E. J. Baerends, *J. Chem. Phys.*, 2008, **128**, 194715.

- [52] I. M. N. Groot, A. W. Kleyn and L. B. F. Juurlink, *J. Phys. Chem. C*, 2013, **117**, 9266.
- [53] G. R. Darling, M. Kay and S. Holloway, *Surf. Sci.*, 1998, **400**, 314.
- [54] A. Cassuto and D. A. King, *Surf. Sci.*, 1981, **102**, 388.
- [55] H. J. Kreuzer, *J. Chem. Phys.*, 1996, **104**, 9593.
- [56] A. F. Carlsson and R. J. Madix, *J. Chem. Phys.*, 2001, **114**, 5304.
- [57] C. R. Brundle, J. Behm and J. A. Barker, *J. Vac. Sci. Technol., A*, 1984, **2**, 1038.
- [58] J. W. Evans and D.-J. Liu, *J. Chem. Phys.*, 2014, **140**, 194704.
- [59] J. E. Davis and C. B. Mullins, *Surf. Sci. Lett.*, 1997, **380**, L513.
- [60] X. Guo, A. Hoffman and J. T. Yates, *J. Chem. Phys.*, 1989, **90**, 5787.
- [61] R. Imbihl and J. E. Demuth, *Surf. Sci.*, 1986, **173**, 395.
- [62] D. T. Vu, K. A. R. Mitchell, O. L. Warren and P. A. Thiel, *Surf. Sci.*, 1994, **318**, 129.
- [63] J. W. Evans, *J. Chem. Phys.*, 1987, **87**, 3038.
- [64] M. Saidy, O. L. Warren, P. A. Thiel and K. A. R. Mitchell, *Surf. Sci.*, 2001, **494**, L799.
- [65] M. Todorova, E. Lundgren, V. Blum, A. Mikkelsen, S. Gray, J. Gustafson, M. Borg, J. Rogal, K. Reuter, J. N. Andersen and M. Scheffler, *Surf. Sci.*, 2003, **541**, 101.
- [66] D.-J. Liu and J. W. Evans, *Surf. Sci.*, 2004, **563**, 13.
- [67] Y. Zhang, V. Blum and K. Reuter, *Phys. Rev. B*, 2007, **75**, 235406.
- [68] K. Klier, Y. N. Wang and G. W. Simmons, *J. Phys. Chem.*, 1993, **97**, 633.
- [69] A. V. Walker, B. Klötzer and D. A. King, *J. Chem. Phys.*, 1998, **109**, 6879.
- [70] L. Jacobse, A. den Dunnen and L. B. F. Juurlink, *J. Chem. Phys.*, 2015, **143**, 014703.
- [71] A. den Dunnen, S. Wiegman, L. Jacobse and L. B. F. Juurlink, *J. Chem. Phys.*, 2015, **142**, 214708.
- [72] D. A. McCormack, R. A. Olsen and E. J. Baerends, *J. Chem. Phys.*, 2005, **122**, 194708.
- [73] I. M. N. Groot, K. J. P. Schouten, A. W. Kleyn and L. B. F. Juurlink, *J. Chem. Phys.*, 2008, **129**, 224707.
- [74] H. Ueta, L. Chen, R. D. Beck, I. Colón-Díaz and B. Jackson, *Phys. Chem. Chem. Phys.*, 2013, **15**, 20526.
- [75] D. J. Miller, H. Öberg, L. Å. Näslund, T. Anniyev, H. Ogasawara, L. G. M. Pettersson and A. Nilsson, *J. Chem. Phys.*, 2010, **133**, 224701.
- [76] T. Zambelli, J. V. Barth, J. Winterlin and G. Ertl, *Nature*, 1997, **390**, 495.
- [77] J. S. McEwen, J. M. Bray, C. Wu and W. F. Schneider, *Phys. Chem. Chem. Phys.*, 2012, **14**, 16677.
- [78] K. Gustafsson and S. Andersson, *J. Chem. Phys.*, 2004, **120**, 7750.
- [79] B. C. Stipe, M. A. Rezaei, W. Ho, S. Gao, M. Persson and B. I. Lundqvist, *Phys. Rev. Lett.*, 1997, **78**, 4410.
- [80] Z. Yang, J. Wang and X. Yu, *Phys. Lett. A*, 2010, **374**, 4713.
- [81] P. Valentini, T. E. Schwartzentruber and I. Cozmuta, *J. Chem. Phys.*, 2010, **133**, 084703.

- [82] J. M. Bradley, X.-C. Guo, A. Hopkinson and D. A. King, *J. Chem. Phys.*, 1996, **104**, 4283.
- [83] S. Ferrer and H. P. Bonzel, *Surf. Sci.*, 1982, **119**, 234.
- [84] A. T. Gee and B. E. Hayden, *J. Chem. Phys.*, 2000, **113**, 10333.
- [85] H. Wang, R. G. Tobin, D. K. Lambert, C. L. DiMaggio and G. B. Fisher, *Surf. Sci.*, 1997, **372**, 267.
- [86] A. Rar and T. Matsushima, *Surf. Sci.*, 1994, **318**, 89.
- [87] Ž. Šljivančanin and B. Hammer, *Surf. Sci.*, 2002, **515**, 235.
- [88] P. Gambardella, Ž. Šljivančanin, B. Hammer, M. Blanc, K. Kuhnke and K. Kern, *Phys. Rev. Lett.*, 2001, **87**, 056103.
- [89] P. J. Feibelman, S. Esch and T. Michely, *Phys. Rev. Lett.*, 1996, **77**, 2257.
- [90] M. Sano, Y. Seimiya, Y. Ohno, T. Matsushima, S. Tanaka and M. Kamada, *Surf. Sci.*, 1999, **421**, 386.
- [91] T. Yamanaka, T. Matsushima, S. Tanaka and M. Kamada, *Surf. Sci.*, 1996, **349**, 119.
- [92] A. Winkler, X. Guo, H. R. Siddiqui, P. L. Hagans and J. T. Yates, *Surf. Sci.*, 1988, **201**, 419.
- [93] X.-C. Guo, J. M. Bradley, A. Hopkinson and D. A. King, *Surf. Sci.*, 1994, **310**, 163.
- [94] L. Vattuone, L. Savio and M. Rocca, *Surf.Sci.Rep.*, 2008, **63**, 101.
- [95] M. J. T. C. van der Niet, A. den Dunnen, L. B. F. Juurlink and M. T. M. Koper, *J. Chem. Phys.*, 2010, **132**, 174705.
- [96] M. A. van Hove and G. A. Somorjai, *Surf. Sci.*, 1980, **92**, 489.
- [97] J. L. Gland, B. A. Sexton and G. B. Fisher, *Surf. Sci.*, 1980, **95**, 587.
- [98] D. L. Bashlakov, L. B. F. Juurlink, M. T. M. Koper and A. I. Yanson, *Catal. Lett.*, 2011, **142**, 1.
- [99] N. R. Avery, *Chem. Phys. Lett.*, 1983, **96**, 371.
- [100] A. E. Wiskerke, F. H. Geuzebroek, A. W. Kleyn and B. E. Hayden, *Surf. Sci.*, 1992, **272**, 256.
- [101] R. P. Bell, *Proc. R. Soc. London Ser. A*, 1936, **154**, 414.
- [102] J. N. Brønsted and K. J. Pedersen, *Z. Phys. Chem.-Stoch. Ve.*, 1924, **108**, 185.
- [103] M. G. Evans and M. Polanyi, *Trans. Faraday Soc.*, 1936, **32**, 1333.
- [104] M. Luppi, D. A. McCormack, R. A. Olsen and E. J. Baerends, *J. Chem. Phys.*, 2005, **123**, 164702.
- [105] K. Besocke, B. Krah-Urban and H. Wagner, *Surf. Sci.*, 1977, **68**, 39.
- [106] O. A. Petrii, *Russ. J. Electrochem.*, 2013, **49**, 401.
- [107] M. J. T. C. van der Niet, A. den Dunnen, L. B. F. Juurlink and M. T. M. Koper, *Angew. Chem. Int. Ed.*, 2010, **37**, 6722.
- [108] M. J. T. C. van der Niet, A. den Dunnen, L. B. F. Juurlink and M. T. M. Koper, *Phys. Chem. Chem. Phys.*, 2011, **13**, 1629.
- [109] D. Chandler, *Nature*, 2005, **437**, 640.
- [110] R. L. Baldwin, *Science*, 2002, **295**, 1657.
- [111] K. A. Dill and J. L. MacCallum, *Science*, 2012, **338**, 1042.
- [112] N. E. Levinger, *Science*, 2002, **298**, 1722.

- [113] M. Wong, J. K. Thomas and T. Nowak, *J. Am. Chem. Soc.*, 1977, **99**, 4730.
- [114] M. R. Hogerheijde, E. A. Bergin, C. Brinch, L. I. Cleeves, J. K. J. Fogel, G. A. Blake, C. Dominik, D. C. Lis, G. Melnick, D. Neufeld, O. Panic, J. C. Pearson, L. Kristensen, U. A. Yildiz and E. F. van Dishoeck, *Science*, 2011, **334**, 338.
- [115] B. Nisini, *Science*, 2000, **290**, 1513.
- [116] S. Ioppolo, H. M. Cuppen, C. Romanzin, E. F. van Dishoeck and H. Linnartz, *Astrophys. J.*, 2008, **686**, 1474.
- [117] F. Schreiber, *J. Phys.: Condens. Matter*, 2004, **16**, R881.
- [118] D. Schwendel, T. Hayashi, R. Dahint, A. Pertsin, M. Grunze, R. Steitz and F. Schreiber, *Langmuir*, 2003, **19**, 2284.
- [119] G. Hummer, J. C. Rasaiah and J. P. Noworyta, *Nature*, 2001, **414**, 188.
- [120] S. Granick and S. C. Bae, *Science*, 2008, **322**, 1477.
- [121] H.-J. Wang, X.-K. Xi, A. Kleinhammes and Y. Wu, *Science*, 2008, **322**, 80.
- [122] P. A. Thiel and T. E. Madey, *Surf. Sci. Rep.*, 1987, **7**, 211.
- [123] M. A. Henderson, *Surf. Sci. Rep.*, 2002, **46**, 1.
- [124] A. Hodgson and S. Haq, *Surf. Sci. Rep.*, 2009, **64**, 381.
- [125] S. Haq, J. Harnett and A. Hodgson, *Surf. Sci.*, 2002, **505**, 171.
- [126] J. Carrasco, A. Michaelides, M. Forster, S. Haq, R. Raval and A. Hodgson, *Nat. Mater.*, 2009, **8**, 427.
- [127] J. L. Daschbach, B. M. Peden, R. S. Smith and B. D. Kay, *J. Chem. Phys.*, 2004, **120**, 1516.
- [128] K. Thürmer and S. Nie, *Proc. Natl. Acad. Sci. U.S.A.*, 2013, **110**, 11757.
- [129] M. Morgenstern, T. Michely and G. Comsa, *Phys. Rev. Lett.*, 1996, **77**, 703.
- [130] K. Morgenstern, *Surf. Sci.*, 2002, **504**, 293.
- [131] J. A. Blackman, *Metallic Nanoparticles, Handbook of Metal Physics*, Elsevier, 2009.
- [132] G. B. Fisher and J. L. Gland, *Surf. Sci.*, 1980, **94**, 446.
- [133] B. A. Sexton, *Surf. Sci.*, 1980, **94**, 435.
- [134] E. Langenbach, A. Spitzer and H. Lüth, *Surf. Sci.*, 1984, **147**, 179.
- [135] U. Starke, K. Heinz, N. Materer, A. Wander, M. Michl, R. Döll, M. A. van Hove and G. A. Somorjai, *J. Vac. Sci. Technol. A*, 1992, **10**, 2521.
- [136] X. Su, L. Lianos, Y. R. Shen and G. A. Somorjai, *Phys. Rev. Lett.*, 1998, **80**, 1533.
- [137] A. L. Glebov, A. P. Graham and A. Menzel, *Surf. Sci.*, 1999, **427**, 22.
- [138] M. Nakamura, Y. Shingaya and M. Ito, *Chem. Phys. Lett.*, 1999, **309**, 123.
- [139] H. Ogasawara, J. Yoshinobu and M. Kawai, *J. Chem. Phys.*, 1999, **111**, 7003.
- [140] K. Jacobi, K. Bedürftig, Y. Wang and G. Ertl, *Surf. Sci.*, 2001, **472**, 9.
- [141] G. Zimbitas and A. Hodgson, *Chem. Phys. Lett.*, 2006, **417**, 1.
- [142] G. Zimbitas, S. Haq and A. Hodgson, *J. Chem. Phys.*, 2005, **123**, 174701.

- [143] G. A. Kimmel, N. G. Petrik, Z. Dohnálek and B. D. Kay, *J. Chem. Phys.*, 2006, **125**, 044713.
- [144] D. C. Skelton, R. G. Tobin, G. B. Fisher, D. K. Lambert and C. L. DiMaggio, *J. Phys. Chem. B*, 2000, **104**, 548.
- [145] M. L. Grecea, E. H. G. Backus, B. Riedmüller, A. Eichler, A. W. Kleyn and M. Bonn, *J. Phys. Chem. B*, 2004, **108**, 12575.
- [146] N. G. Petrik and G. A. Kimmel, *J. Chem. Phys.*, 2004, **121**, 3727.
- [147] M. J. T. C. van der Niet, A. den Dunnen, M. T. M. Koper and L. B. F. Juurlink, *Phys. Rev. Lett.*, 2011, **107**, 146103.
- [148] A. den Dunnen, M. J. T. C. van der Niet, M. T. M. Koper and L. B. F. Juurlink, *J. Phys. Chem. C*, 2012, **116**, 18706.
- [149] M. J. T. C. van der Niet, I. Dominicus, M. T. M. Koper and L. B. F. Juurlink, *Phys. Chem. Chem. Phys.*, 2008, **10**, 7169.
- [150] A. Cordoba and J. J. Luque, *Phys. Rev. B*, 1982, **26**, 4028.
- [151] P. Löfgren, P. Ahlström, D. V. Chakarov, J. Lausmaa and B. Kasemo, *Surf. Sci.*, 1996, **367**, L19.
- [152] D. Lackey, J. Schott, J. K. Sass, S. I. Woo and F. T. Wagner, *Chem. Phys. Lett.*, 1991, **184**, 277.
- [153] N. Kizhakevariam and E. M. Stuve, *Surf. Sci.*, 1992, **275**, 223.
- [154] C. Hahn, J. Shan, Y. Liu, O. T. Berg, A. W. Kleyn and L. B. F. Juurlink, *J. Chem. Phys.*, 2012, **136**, 114201.
- [155] R. Mom, C. Hahn, L. Jacobse and L. B. F. Juurlink, *Surf. Sci.*, 2013, **613**, 15.

Summary

Heterogeneous catalysis is very important for industrial applications and the environment. It is known that precious metals, such as Pd and Pt, can be good catalyst materials for various reactions. However, these metals are expensive and their catalytic action is not yet completely understood. In the search for better and cheaper materials, more fundamental knowledge is necessary. We use ultra-high vacuum techniques and well-ordered Pd and Pt single crystals to further investigate the oxygen dissociation process and the interaction of water with deuterated surfaces.

The breaking of the oxygen-oxygen bond of O_2 is a crucial step in various oxidation reactions, for example in the CO oxidation reaction in the three-way catalytic converter. In chapter 3, we have studied the oxygen dissociation process in the zero-coverage regime on Pd(100) as function of incident energy, surface temperature and incident angle. We have compared our data to those previously obtained by other groups. The Pd(100) surface shows a very high oxygen reactivity. Two mechanisms play a role in sticking and dissociation of O_2 . At high incident energy, O_2 molecules dissociate directly on the Pd(100) surface. At low incident energy, O_2 dissociates via an indirect pathway. We suggest a dynamical precursor that accounts for the indirect process and steering causes the absolute reactivity. The barrier to dissociation on this surface is very low. The other low-Miller-index surfaces show different dynamics. On Pd(111), a sequential physisorption and molecular chemisorption precursor mechanism was suggested for low incident energy. At high energies, the molecules directly adsorb in the molecular chemisorption well, but no direct dissociation was observed. The molecular state is stable on Pd(111), where it is not on Pd(100) (in the zero-coverage limit). The very attractive molecular chemisorption precursor state leads to dissociation on Pd(110) at low energies. At

high incident energy, a direct dissociation pathway opens.

In chapter 4, we investigate the oxygen adsorption and desorption processes on Pd(100) further. The sticking probability over time and the obtained maximum coverage are dependent on incident energy and surface temperature. The King and Wells traces indicate that the dissociation process is temperature independent for the first few seconds of the experiment. After some time the trace of 100 K remains higher than the 400 K trace for all energies. Additional oxygen molecules can adsorb on the patches of oxygen atoms. This is also confirmed by the subsequent TPD spectra. Dosing at a temperature between 100 and 150 K results in an additional molecular desorption peak (the δ -peak). During the temperature ramp, part of the oxygen molecules desorb, the other part still dissociates and desorbs recombinatively at a higher temperature in a sharp and narrow peak (the γ -peak). This leads to a relatively high surface coverage with respect to the high temperature experiments. At temperatures between 200 and 600 K and at low incident energy, the γ -peak is absent. This peak increases with increasing energy and temperature. A combination of high energy and temperature or dosing at a very low surface temperature results in higher oxygen coverage on the Pd(100) surface.

In chapter 5, oxygen adsorption and dissociation on Pt(553) was studied in a similar way as described for Pd(100). The data is compared to literature data from Pt(533), Pt{110}(1x2), and Pt(111). At low incident energy, all stepped surfaces show a similar reactivity. This reactivity is higher than on the flat Pt(111) surface. The exact arrangement of the atoms that form the corrugation of the surface does not play a role here. At high incident energy, Pt(533) and Pt(553) are still more reactive than Pt(111), however, in this regime the dissociation dynamics do depend on step type. The sticking probability is higher on the surface with the (100) steps than the one with (110) steps. On Pt(111), it was suggested that oxygen dissociation proceeds via an indirect process via the physisorbed state to the molecularly chemisorbed state at low energy. At high energy, the molecules can access the molecular chemisorbed state directly. The processes on Pt(533) are described to be the same as on Pt(111), with an additional pathway to dissociation. At low energy, the steps provide an additional path to direct chemisorption and increase the conversion of the physisorbed state to the molecular chemisorbed state. At high energy, oxygen molecules can dissociate directly via an activated pathway. For Pt(553), we suggest that parallel sticking mechanisms indeed occur, but we expect that the molecular sticking at steps at low energy is a non-activated process.

At high energy, the indirect mechanisms are replaced by activated direct sticking at the (111) terraces. TPD experiments show the presence of a molecular state on the (111) terraces and the (110) steps. Oxygen desorption from the (100) step type surface occurs at a higher temperature than the surface with (110) steps. The difference in the processes of Pt(553) and Pt(533) is due to a variation in the effective lowering of the barrier to dissociation from the molecularly adsorbed states into the atomic states.

The co-adsorption of water and deuterium on Pt is a relevant process for e.g. fuel cells, where both types of molecules are present on the surface. In chapter 6, we study the interaction of water with D-precovered Pt surfaces with the (100) step type and varying width of the (111) terraces by temperature programmed desorption. Water TPD spectra from the bare surfaces show a desorption peak from the step sites, the terrace sites and the multilayer. The (100) steps bind water more strongly than the (111) terraces. The water stabilization is annihilated by pre-adsorbing deuterium to the steps. At the same time, the water on the (111) terraces is stabilized, as on Pt(111). The stabilization reverses when the (111) terraces are also precovered with deuterium. The completely precovered Pt surfaces with (100) steps and terraces (up to 8 atom wide) become completely hydrophobic. Water desorption occurs in a single desorption peak in the region where the water multilayer usually desorbs and the exchange between H (from water) and D (from deuterium) atoms decreases. On these stepped surfaces with (100) steps, water forms amorphous solid water clusters near the step sites and does no longer spread over the surface as the Pt(111) and Pt(553) surfaces. Defect sites play a role in the delicate balance between intermolecular forces. The adsorption energy governs hydrophilic or hydrophobic behavior. The influence of steps on the adsorption of water on nanostructured Pt has a very long-ranged character which is non-linear with step density. The steps break the ability of terrace-bound water to properly form hydrogen bonds.

The future plans are presented in chapter 7. The combination of double molecular beam experiments and the use of curved single crystals is the next challenge to obtain even more knowledge on complex processes occurring in real heterogeneously catalyzed reactions.

Samenvatting

Heterogene katalyse is erg belangrijk voor industriële toepassingen en het milieu. Het is bekend dat waardevolle metalen, zoals Pd en Pt, vaak goede katalysator materialen zijn voor verschillende reacties. Echter, deze metalen zijn duur en de katalytische activiteit is nog niet volledig bekend. In de zoektocht naar betere en goedkopere materialen is een betere fundamentele kennis noodzakelijk. Wij gebruiken ultrahoog vacuüm technieken en Pd en Pt éénkristallen om het zuurstof dissociatie proces en de interactie van water met een gedeutereerd oppervlak verder te bestuderen.

Het breken van de zuurstof-zuurstof binding van O_2 is een cruciale stap in verschillende oxidatie reacties, zoals de CO oxidatie reactie in de driewegkatalysator. We hebben het zuurstof dissociatie proces op een schoon Pd(100)oppervlak bestudeerd voor verschillende energieën, oppervlakte temperaturen en invalshoeken (hoofdstuk 3). We hebben onze data vergeleken met eerder gemeten data van andere groepen. Het Pd(100) oppervlak vertoont een erg hoge zuurstof reactiviteit. Er zijn twee mechanismen die een rol spelen bij het adsorberen en dissociëren. Bij hoge energie dissociëren de zuurstof moleculen direct op het Pd(100) oppervlak. Bij lage energie, dissocieert zuurstof via een indirect pad. Wij stellen een dynamische precursor voor die het indirecte proces kan verklaren. Sturing zorgt voor de absolute reactiviteit. De barrière voor dissociatie op dit oppervlak is erg laag. De andere lage-Miller-index oppervlakken laten andere dynamica zien. Op Pd(111) werd een opeenvolgend fysisorptie en moleculaire chemisorptie precursor mechanisme voorgesteld voor lage energie. Bij hoge energieën adsorberen de moleculen direct in de moleculaire chemisorptie put, er werd geen directe dissociatie waargenomen. De moleculaire staat is stabiel op Pd(111), maar niet op het kale Pd(100) oppervlak. De sterk gebonden moleculaire gechemisorbeerde pre-

cursor staat zorgt voor zuurstof dissociatie op Pd(110) bij lage energieën. Bij hoge energie opent een direct dissociatie pad.

In hoofdstuk 4 bestuderen we de zuurstof adsorptie en desorptie processen op Pd(100) verder. The kans voor adsorptie over de tijd en de maximaal te verkrijgen bedekking zijn afhankelijk van de energie en oppervlakte temperatuur. De adsorptie signalen(King en Wells) laten zien dat het dissociatie proces temperatuursonafhankelijk is voor de eerste seconden van het experiment. Na een bepaalde tijd blijft de lijn van 100 K hoger dan die van 400 K voor alle energieën. De extra zuurstof moleculen kunnen adsorberen op de eilanden van zuurstof atomen. Dit wordt bevestigd door de opeenvolgende desorptie (TPD) spectra. Het doseren van zuurstof bij een oppervlakte temperatuur tussen 100 en 150 K resulteert in een extra moleculaire desorptie piek(de δ -piek). Tijdens het verwarmen van het kristal desorbeert een deel van de zuurstof moleculen. Het andere deel dissocieert alsnog en desorbeert recombinatief bij een hogere temperatuur in een scherpe piek (de γ -piek). Dit zorgt voor een relatief hoge oppervlakte bedekking in vergelijking tot de hoge temperatuur experimenten. Bij temperaturen tussen 200 en 600 K en lage energie is de γ -piek afwezig. Deze piek groeit met toenemende energie en toenemende temperatuur. Een combinatie van hoge energie en hoge temperatuur of doseren bij een erg lage oppervlakte temperatuur resulteert in een hogere zuurstof bedekking op het Pd(100) oppervlak.

De zuurstof adsorptie en dissociatie op Pt(553) werd op een zelfde manier als op Pd(100) bestudeerd in hoofdstuk 5. De data werd vergeleken met data uit de literatuur voor Pt(533), Pt{110}(1x2), en Pt(111). Bij lage energie laten alle gestapte oppervlakken een vergelijkbare reactiviteit zien. Deze reactiviteit is hoger dan op het vlakke Pt(111) oppervlak. De exacte rangschikking van de atomen die de stappen vormen maakt hierbij niet uit. Bij hoge energie laten Pt(533) en Pt(553) nog steeds een hogere reactiviteit zien dan Pt(111), maar hierbij hangt de dissociatie dynamica wel af van het stap type. De kans voor adsorptie is hoger voor het oppervlak met de (100) stappen dan het oppervlak met de (110) stappen. Voor Pt(111) werd voorgesteld dat zuurstof dissociatie bij lage energie plaatsvindt via een indirect proces via de fysisorptie toestand naar de moleculaire chemisorptie toestand. Bij hoge energie kunnen de moleculen direct naar de gechemisorbeerde toestand. De processen op Pt(533) worden hetzelfde beschreven als op Pt(111), maar met een extra pad naar dissociatie. Bij lage energie verschaffen de stappen een extra pad voor directe chemisorptie en verhogen ze de conversie van de fysisorptie toe-

stand naar de moleculaire chemisorptie toestand. Bij hoge energie kunnen de zuurstof moleculen direct dissociëren via een geactiveerd pad. Voor Pt(553) stellen wij een parallel adsorptie mechanisme voor, waarbij we verwachten dat het adsorberen van de zuurstof moleculen aan de stapranden bij lage energie een niet-geactiveerd proces is. Bij hoge energie worden de indirecte mechanismen vervangen door geactiveerde adsorptie aan de (111) terrassen. TPD experimenten laten de aanwezigheid van een moleculaire toestand op de (111) terrassen en de (110) stappen zien. Zuurstof desorptie van het oppervlak met het (100) stap type vindt plaats bij een hogere temperatuur dan het oppervlak met het (110) stap type. Het verschil in de processen op Pt(553) en Pt(533) wordt veroorzaakt door een variatie in de effectieve verlaging van de barrière tot dissociatie van de molecuair geadsorbeerde toestanden naar de atomaire toestanden.

De co-adsorptie van water en deuterium op Pt is een relevant proces voor bijvoorbeeld brandstofcellen, waarbij beide soorten moleculen aan het oppervlak aanwezig zijn. In hoofdstuk 6 bestuderen wij door middel van TPD de interactie van water met deuterium bedekte Pt oppervlakken met het (100) stap type en een variatie in de (111) terras breedte. Water TPD spectra van het kale oppervlak laten een desorptie piek van de stappen, de terrassen en de multilaag zien. De (100) stappen binden water sterker dan de (111) terrassen. Deze stabilisatie van water wordt teniet gedaan wanneer deuterium vooraf op de stappen wordt geadsorbeerd. Tegelijk wordt het water op de (111) terrassen tijdelijk gestabiliseerd, zoals op Pt(111). De stabilisatie keert om wanneer het (111) terras ook vooraf bedekt is met deuterium. Pt oppervlakken met (100) stappen en terrassen (tot 8 atomen breed) die compleet bedekt zijn met deuterium worden in het geheel hydrofoob. Water desorptie vindt nu plaats in een enkele desorptiepiek in het gebied waar de water multilaag normaal gesproken desorbeert. De uitwisseling tussen H (van het water) en D (van het deuterium) atomen vermindert. Op deze gestapte oppervlakken met (100) stappen vormt water een ASW cluster rond de stap randen. Het water verspreidt zich niet meer over dit oppervlak, zoals op Pt(111) en Pt(553). Defecten spelen een rol in de delicate balans tussen intermoleculaire krachten en de adsorptie energie die zorgt voor het hydrofobe of hydrofiele gedrag. De invloed van stappen op de adsorptie van water op nano-gestructureerd Pt heeft een erg ver reikend karakter en is niet lineair met de stapdichtheid. De stappen breken de mogelijkheid van water dat gebonden is aan de terrassen om waterstofbruggen te vormen.

De toekomstige plannen worden gepresenteerd in hoofdstuk 7. De combinatie

van een dubbele moleculaire bundel en gebruik van gekromde éénkristallen is de volgende uitdaging om nog meer kennis over de complexe processen die plaatsvinden in de echte heterogene katalyse te vergaren.

List of Publications

This thesis is based on the following publications:

Chapter 3

Reaction dynamics of initial O_2 sticking on Pd(100)

J. Chem. Phys., 2015, **142**, 214708

Angela den Dunnen, Sandra Wiegman, Leon Jacobse, and Ludo B. F. Juurlink

Chapter 4

Thermal desorption and time dependent adsorption of oxygen on Pd(100)

In preparation

Angela den Dunnen, Leon Jacobse, Sandra Wiegman, and Ludo B. F. Juurlink

Chapter 5

The molecular dynamics of adsorption and dissociation of O_2 on Pt(553)

J. Chem. Phys., 2015, **143**, 014703

Leon Jacobse, Angela den Dunnen, and Ludo B. F. Juurlink

Chapter 6

Long-range influence of steps on water adsorption on clean and D-covered Pt surfaces

Phys. Chem. Chem. Phys., 2015, **17**, 8530

Angela den Dunnen, Maria J. T. C. van der Niet, Cansin Badan, Marc T. M. Koper, and Ludo B. F. Juurlink

Other publications:

Interaction between H_2O and preadsorbed D on the stepped Pt(553) surface

Journal of Physical Chemistry C, 2012, **116**, 18706

Angela den Dunnen, Maria J. T. C. van der Niet, Marc T. M. Koper, and Ludo B. F. Juurlink

Structural modification of platinum model systems under high pressure CO annealing

Journal of Physical Chemistry C, 2012, **116**, 15353

David N. McCarthy, Christian E. Strebel, Tobias P. Johansson, Angela den Dunnen, Anders Nierhoff, Jane H. Nielsen, and Ib Chorkendorff

Tuning hydrophobicity of platinum by small changes in surface morphology

Physical Review Letters, 2011, **107**, 146103

Maria J. T. C. van der Niet, Angela den Dunnen, Marc T. M. Koper, and Ludo B. F. Juurlink

A detailed TPD study of H_2O and pre-adsorbed O on the stepped Pt(553) surface

Physical Chemistry Chemical Physics, 2011, **13**, 1629

Maria J. T. C. van der Niet, Angela den Dunnen, Ludo B. F. Juurlink, and Marc T. M. Koper

The influence of step geometry on the desorption characteristics of O_2 , D_2 , and H_2O from stepped Pt surfaces

Journal of Chemical Physics, 2010, **132**, 174705

Maria J. T. C. van der Niet, Angela den Dunnen, Ludo B. F. Juurlink, and Marc T. M. Koper

Co-adsorption of O and H_2O on nanostructured platinum surfaces: Does OH form at steps?

Angewandte Chemie-international Edition, 2010, **49**, 37

Maria J. T. C. van der Niet, Angela den Dunnen, Ludo B. F. Juurlink, and Marc T. M. Koper

Palladium-diphosphine complexes as catalysts for allylations with allyl alcohol

Journal of Molecular Catalysis A-chemical, 2010, **329**, 96

Jimmy A. van Rijn, Angela den Dunnen, Elisabeth Bouwman, and Eite Drent

Curriculum Vitae

Angela den Dunnen werd geboren op 24 oktober 1986 in Hardinxveld-Giessendam en groeide op in Sliedrecht. Tussen 1999 en 2005 ging zij naar het Gymnasium Camphusianum te Gorinchem. In 2005 begon ze aan haar studie Scheikunde aan de Universiteit Leiden. Tijdens haar BSc opleiding heeft ze een stage project gedaan in de groep van prof. dr. Elisabeth Bouwman (Coordination and Bioinorganic Chemistry groep) over 'Ruthenium and Palladium Catalyzed Allylation of Alcohols'. In 2008 is Angela begonnen met haar MSc met de specialisatie 'Physical and Theoretical Chemistry'. Hiervoor heeft ze twee stage projecten gedaan. Het eerste project was in de groep van prof. dr. Marc Koper and dr. Ludo Juurlink (Catalysis and Surface Chemistry groep). Samen met Janneke van der Niet bestudeerde ze de interactie van zuurstof/water/deuterium op gestapte Pt(553) en Pt(533) oppervlakken. Met de poster die zij maakte over dit onderwerp, won ze de VIRAN poster prijs op de X^{th} Netherlands' Catalysis and Chemistry Conference (NCCC). Voor het tweede project verhuisde Angela voor 5 maanden naar Denemarken. Daar deed zij een stage in de groep van prof. dr. Ib Chorkendorff (Center for Individual Nanoparticle Functionality, Technical University of Denmark, Lyngby). Ze werkte samen met Tobias Johansson aan 'Surface Science Studies of the Reactivity of Pt(111) in Comparison to Nanoparticles'. In februari 2011 behaalde ze haar MSc titel.

Tijdens haar studie was Angela werkzaam als student assistent bij het Junior Science Lab. Ook was ze actief bij de studievereniging Chemisch Dispuut Leiden (CDL). Ze heeft in verschillende commissies plaatsgenomen, zoals de bakcie en de fotocie. Ook zat ze in commissies die studiereizen naar België, Kopenhagen en Duisburg organiseerden.

In 2011 is Angela begonnen aan haar promotieonderzoek in de groep van prof.

dr. Marc Koper and dr. Ludo Juurlink (Catalysis and Surface Chemistry groep, Leiden Institute of Chemistry). De focus lag in eerste instantie op het bestuderen van de dissociatie van ethanol aan gestapte platina oppervlakken. Later verschoof de focus naar de interactie van zuurstof/water/waterstof met verschillende oppervlakte structuren van platina en palladium. Angela heeft dit werk op verschillende nationale en internationale symposia, conferenties en workshops gepresenteerd. Tijdens het promotietraject heeft ze verschillende projecten begeleid ('Practicum Basisvaardigheden', 'Leren Onderzoeken', BSc en MSc stage projecten). Ook was ze lid van het PhD platform van de HRSMC (Holland Research School Molecular Chemistry) en organiseerde zij verschillende activiteiten voor de vakgroep.

In augustus 2015 is Angela begonnen als 'Eerst de Klas' trainee. Tijdens dit tweejarige programma volgt zij de Universitaire Lerarenopleiding, een leiderschapsprogramma en geeft ze les op het Visser 't Hooft Lyceum in Leiden.